ISSN 1342-3479

北海道工業技術研究所報告

REPORTS
OF
THE HOKKAIDO NATIONAL INDUSTRIAL RESEARCH INSTITUTE

第69号
1997年 3 月

工業技術院
北海道工業技術研究所

北海道工業技術研究所報告第69号

目　次

REPORTS OF THE HOKKAIDO NATIONAL INDUSTRIAL RESEARCH INSTITUTE, No.69

Contents

〈要　　旨〉

環境問題の過去、現在そして未来　－地球にやさしい社会と技術をめざして－

吉田　諒一

北海道工業技術研究所において進められてきた環境関連技術開発を中心にその周辺技術の現状並びに今後の課題について概説した。

キーワード： 環境問題、資源リサイクル、地球環境

炭酸ガスレーザーで合成した炭化ケイ素－窒化ケイ素複合超微粒子の^{29}Siマジックアングルスピニング NMRとESRによる構造解析

鈴木　正昭、長谷川　義久、相沢　正之、中田　善徳、奥谷　　猛、魚崎　浩平

CO_2レーザーで合成した炭化ケイ素－窒化ケイ素複合粒子(SiC-Si_3N_4)の構造をマジックアングルスピニング核磁気共鳴(MAS-NMR)と電子スピン共鳴(ESR)によって調べた。シリコン(Si)原子の周りの構造は窒素を導入することで変化した。シリコン原子のまわりの炭素原子は窒素によって置換され、窒素量が多くなるにしたがって順次窒素リッチな配位が増加した。窒素含量の低い複合粒子は主として固溶した窒素を含むベータSiC相からなっていた。窒素原子は一部ベータSiC微結晶中に存在し、一部は粒子内の粒界に存在する。ベータSiC微結晶中では窒素は4個のSiに囲まれた4配位として存在し、粒界相では3個のSiと結合した3配位で存在する。高窒素含量の粒子はSiC,Si_3N_4アモルファス相からなり、それぞれの量は窒素量によって変化した。

キーワード：炭化ケイ素、窒化ケイ素、超微粒子、炭酸ガスレーザー、核磁気共鳴、電子スピン共鳴

ホットプレス法によるAl-セラミックス系複合強化材の作製

植田　芳信，鈴木　良和，下川　勝義，村上　和幸

Al合金にセラミックスの粉末を分散または，ウィスカーで強化した複合材料をホットプレス装置を用いて，973Kで作製し，その後，高温で加熱処理を行った。これらの複合材料の機械的性質について，三点曲げ試験と硬さ試験で調べ，その微細組織を，走査電顕やＸ線回折とＸＭＡ分析で検討した。

これらの結果，ホットプレス法による強化は，セラミックスの粉末を分散させた複合材料よりもウィスカーで強化させる複合材に効果的であるが，ホットプレスの後，高温にさらされることによって，セラミックス粉末を分散させた方は複合材の中に，気孔や亀裂が生じにくいので機械的強度を保持するのに有利であることを明らかにした。

キーワード：Al-セラミックス系複合強化材、ホットプレス法、三点曲げ試験、硬さ試験

乳酸の分離精製に関する研究
－逆浸透法の基礎的検討－

M. K. H. Liew，田中　重信，森田　幹雄

ポリアミド系複合逆浸透膜を用いて、乳酸並びに乳酸塩水溶液の物理化学的性質と逆浸透法の効果との関係を回分法で検討した。この複合膜はpH2.2で膨潤するが、顕著な溶質・膜相互作用は観察されなかった。操作圧力、原料濃度、撹拌速度などの操作条件を調べた結果、最適操作条件は操作圧が7 MPa、撹拌速度は900 rpmとなった。透過量の減少とともに溶質分離係数は増加し、乳酸溶液、乳酸アンモニウム溶液、乳酸ナトリウム溶液の透過量と溶質分離係数はそれぞれ（$0.66 m^3 m^{-2} d^{-1}$：5.8）、（$0.30 m^3 m^{-2} d^{-1}$：18.3）、（$0.18 m^3 m^{-2} d^{-1}$：＞80）であった。この関係は、原料溶液のpHで支配される溶質の解離イオン濃度と関連づけられることが明らかになった。

キーワード：ポリアミド複合膜、乳酸塩、乳酸、ｐＨ、イオン解離、逆浸透法

二酸化炭素ハイドレートの成長過程におけるラマン分光測定

内田　　努、高木　哲史、河端　淳一、前晋　　爾、本堂　武夫

二酸化炭素溶液から結晶面を持つ二酸化炭素ハイドレート結晶の成長過程を観測した。二酸化炭素溶液とハイドレートの両相について、ラマン分光測定を行った結果、二酸化炭素分子及び水分子のラマンスペクトルが、それぞれの相で異なることが明らかになった。また各分子のスペクトル強度比から、二酸化炭素ハイドレートの密度を見積もる方法を提案した。その結果本研究で得られた二酸化炭素ハイドレートの密度は、結晶モデルから予想されていた値より小さいことがわかった。

キーワード：二酸化炭素ハイドレート、ラマン分光、深海、二酸化炭素貯留

木材の熱分解によるレボグルコサンの収率に及ぼす昇温速度の影響

三浦　正勝、田中　重信、安藤　公二

赤外線加熱炉によってカラマツを熱分解し、レボグルコサンの収率に及ぼす昇温速度の影響を明らかにした。熱分解雰囲気による圧力の減少はレボグルコサンの収率を増大させるが高度の減圧は不要である。昇温速度の増大は、圧力の減少と同様レボグルコサンの収率を増大させ、炭化物の収率を減少させる効果がある。しかし昇温速度が著しく大きくなるとレボグルコサンの収率は減少する。88 kPaで無処理カラマツを熱分解した結果、昇温速度が1.3 K/s近傍でレボグルコサンの収率が最大となった。

キーワード：加熱速度、急速熱分解、木材、無水糖、レボグルコサン、赤外線加熱炉

南極氷床中に天然に産出される空気ハイドレート結晶の屈折率測定

内田　努、島田　亙、本堂　武夫、前晋　爾、N.I.Barkov

南極氷床氷中に天然に存在する空気ハイドレートの屈折率を、マッハツェンダー干渉系を用いて測定した。ハイドレートを包蔵している氷の屈折率との微少な差を、干渉縞のずれから測定した結果、ハイドレートの屈折率は氷のものより5.3x10-3大きいことがわかった。屈折率はハイドレートのケージ占有率に依存するため、測定結果からOnsager空洞モデルを用いてケージ占有率を見積もる方法を提案した。

キーワード：空気ハイドレート、屈折率、マッハツェンダー干渉系、Onsager空洞モデル、ケージ占有率

白金を修飾剤として用いる黒鉛炉原子吸光法による電解液中ケイ素の定量

福嶋　正巳、緒方　敏夫、原口　謙策、中川　孝一、伊藤　三郎、
角　正夫、浅見　直人

白金を化学修飾剤として用いた黒鉛炉原子吸光法によるケイ素の分析法を確立した。本法は、修飾剤が存在しない場合に比較し15倍感度が増加し、ケイ素の検量線は0～0.8ng範囲で直線となり、検出限界はブランク信号3σから計算し8pgとなった。修飾剤として白金を用い、ゼーマン効果バックグラウンド補正を行う本法により、燃料電池型電解セルでの電解液中ケイ素を、0.1M 塩化リチウムのマトリックスマッチング剤共存下で定量、良好な結果が得られ、また一般試料に対しても十分適用できる。

キーワード：ケイ素、化学修飾剤、白金、電解液、黒鉛炉原子吸光法

〈Abstracts〉

The Past, Present and Future Trends in Environmental Problems —— Toward Ecologically Conscious Society and Technology ——

Ryoichi YOSHIDA

This paper summarizes R & D related to environmental problems in the Hokkaido National Industrial Research Institute (HNIRI), and also gives an overview of the present state and the future subject of their relating technologies.

Key Words : Environmental problems, Recycled resources, Global environment

Characterization of Silicon Carbide-Silicon Nitride Composite Ultrafine Particles Synthesized Using a CO_2 Laser by Silicon-29 Magic Angle Spinning NMR and ESR

Masaaki SUZUKI, Yoshihisa HASEGAWA, Masayuki AIZAWA
Yoshinori NAKATA and Takeshi OKUTANI

The structure of silicon carbide-silicon nitride (SiC-Si_3N_4) composite particles synthesized using a CO_2 laser was studied by magic angle spinning nuclear magnetic resonance (MAS-NMR) and electron spin resonance (ESR). The structure around Si atom changed by introducing nitrogen. Carbon atoms around Si were substituted by N atoms and N-rich configurations around Si atom increased stepwise as the N content increased. The low N content composite particles consisted of mainly SiC phase containing dissolved nitrogen. Nitrogen atoms were partly present in β-SiC microcrystal and partly in the grain boundary layer in the particle. Nitrogen atoms were tetrahedrally surrounded by four Si atoms in β-SiC microcrystal and were trivalent state bonded to three Si atoms in the grain boundary layer. The high N content particles consisted of SiC, Si_3N_4, and amorphous phases, whose amount depended on N content.

Key Words : Silicon carbide, Silicon nitride, Ultrafine particles, CO_2 laser, MAS-NMR, ESR

Fabrication of Al/Ceramic Composites by Hot Pressing

Yoshinobu UEDA, Yoshikazu SUZUKI,
Katsuyoshi SHIMOKAWA and Kazuyuki MURAKAMI

Ceramic powder dispersed or whisker-reinforced Al composite was produced by hot pressing at 973K and exposure to high temperature of 1523K. The mechanical properties and micro structures of each compositewere examined by a three-point bending test, hardness tester, scanningelectron microscopy, X-ray diffraction patterns and XMA analysis.

The present method was found more effective for obtaining the whiskerreinforced Al composite than a powder dispersed Al composite. The powderdispersed Al composite following heat-treatment at high temperature maintained its mechanical strength owing to fewer pores and cracks.

Key Words : Al/Ceramic composites, Hot pressing, Three-point bending test, Hardness test

Separation and Purification of Lactic Acid : Fundamental Studies on the Reverse Osmosis Down-stream Process

M.K.H. LIEW, Shigenobu.TANAKA and Mikio. MORITA

The physico-chemical properties and effects of lactic acid and lactates in the reverse osmosis process were investigated using a polyamide composite membrane. The membrane was found to swell at pH 2.2, yet has no detectable solute-membrane affinity. The decrease in flux and increase in the solute reduction factor of lactic acid ($0.66\ m^3.m^{-2}.d^{-1}$; 5.8), ammonium lactate ($0.30\ m^3.m^{-2}.d^{-1}$; 18.3) and sodium lactate ($0.18\ m^3.m^{-2}.d^{-1}$; >80) were found to be related to the concentration of ions dissociated into solution as affected by the pH of the feed. The effects of operating parameters such as pressure, feed concentration and stirring speed were also discussed. Optimum operating conditions were found to be 7 MPa and 900 rpm.

Key words : Polyamide composite membrane; Lactate; Lactic acid; pH; Ion dissociation; Reverse osmosis

Raman Spectroscopic Analyses on the Growth Process of CO_2 Hydrates

Tsutomu UCHIDA, Akifumi TAKAGI, Junichi KAWABATA,
Shinji MAE and Takeo HONDOH

CO_2 hydrate crystals with polyhedral facet were observed to grow from CO_2 solution. For both CO_2 hydrates and CO_2 solution, raman spectroscopic analyses were carried out. Raman spectra of CO_2 and H_2O molecules in CO_2 hydrate were different from those in CO_2 solution. We presented an attempt to estimate the density of CO_2 hydrate by the raman intensity ratio, and found that the densities of CO_2 hydrates were considerably smaller than those used in some modeling studies.

Key Words : CO_2 hydrate, Raman spectroscopy, deep sea, CO_2 sequestration

Effect of Heating Rate on Yield of Levoglucosan in Wood Pyrolysis

Masakatsu Miura, Shigenobu Tanaka and Koji Ando

The Yield of levoglucosan (LG:one kind of anhydrosugar) from wood particles by pyrolysis was studied using infrared-ray furnace under various heating rates.

A slight reduction of pressure was found to increase the yield of levoglucosan. The increase of heating rate resulted in an increase of the yield of levoglucosan and a decrease of the yield of solid product, as was the case for the reduction of pressure. However, at an extremely high heating rate, the yield of levoglucosan decreased. As the result of pyrolysis of *Karamatsu* under 88 kPa, maximum yield of levoglucosan was obtained at heating rate of nearly 1.3 K/s.

Key Words : Rapid pyrolysis, Cellulosic materials, Wood , Anhydro sugar, Levoglucosan, Heating rate, Infrared furnace

Refractive Index Measurements of Natural Air - hydrate Crystals in Antarctic Ice Sheet

Tsutomu UCHIDA, Wataru SHIMADA, Takeo HONDOH, Shinji MAE and N.I. Barkov

The refractive index of air-hydrate crystals found in the deep Antarctic ice sheet was measured for the first time using a Mach-Zehnder interferometer. A very small difference between the refractive indices of the air-hydrate crystals and the matrix ice crystal was measured by a fringe-shift method. It was found that the refractive indices of all air-hydrate crystals were larger than those of ice, and the average difference was 5.3×10^{-3}, even considering the refractive index anisotropy of ice crystal. Because the refractive indices depended on the occupancy ratio of the cage-like cavities by air molecules, the experimental results are compared with the calculated values using the Onsager cavity model. It is suggested that the present method is useful for estimation of the cavity occupancy ratio of air-hydrate crystals, and also of the amount of air molecules in polar ice cores.

Key Words : Air hydrate, Refractive index, Mach-Zehnder interferometer, Onsager Cavity model, cage occu pancy

Determination of Silicon in Electrolyte Solutions by Electrothermal Atomic Absorption Spectrometry Using Platinum as a Matrix Modifier

Masami FUKUSHIMA, Toshio OGATA*, Kensaku HARAGUCHI, Kohichi NANAGAWA, Saburo ITO, Masao SUMI and Naoto ASAMI

A method has been developed for the determination of silicon by electrothermal atomic absorption spectrometry using platinum as a chemical modifier. The sensitivity for the determination was improved by a factor of 15 in the presence of platinum as compared with that in the absence of a chemical modifier. The calibration curve for silicon was linear over the range 0~0.8 ng, and the detection limit was calculated (as 3σ of the blank absorbance) to be 8 pg. The concentration of silicon in the electrolyte solutions of fuel cells was determined using the platinum modifier and Zeeman-effect background correction, with 0.1 mol^{-2} of litium chloride present as a matrix matching reagent.

Key Words : Silicon, Chemical modifier, Platinum, Electrolyte solutions, Electrothermal atomic absorption spectrometry

環境問題の過去、現在そして未来
―地球にやさしい社会と技術をめざして―

（キーワード：環境問題、資源リサイクル、地球環境）

吉田　諒一*1

1．はじめに

環境問題は、従来型産業公害問題などの国内環境問題と地球温暖化問題などの地球環境問題とに大別され、これらが地球の自然浄化力の範囲を越え、地球の環境耐量の限界に近づきつつあると認識されてきている。例えば、㈶旭硝子財団が環境「終末時計」（12時が終末）について世界の環境専門家を対象に行っている調査結果では、全回答者の平均が1992年７時49分、1995年８時49分そして1996年の調査では９時13分となり、同調査では「９～12時」を「極めて不安な時間」と定義している。なかでも北米の専門家は９時30分さらに西ヨーロッパの専門家は９時46分と分析している。このような人類社会をとりまく現状を解決するために、現在、地球に優しい社会システムと技術の構築が求められている。ここでは、北海道工業技術研究所（北工研）において進められてきた環境関連技術開発を中心に、その周辺技術の現状並びに今後の課題について概説する。

2．北工研における環境関連技術研究開発の概要

北工研では、昭和36年に当所が研究業務を開始して以来、図１に示したように、排水、排ガス・悪臭、廃プラスチック・廃タイヤ、バイオマス、石炭灰、IC基板、廃油および環境リスク等の環境関連技術に関する研究を実施してきている[1)]。最近、当所において実施したあるいは実施中の環境関連技術に関するプロジェクトは以下の通りである。

① 先端産業廃棄物の処理に関する研究（平成２年度～平成４年度）
② 循環流動層を用いた排ガス中の二酸化炭素吸着に関する研究（平成２年度～平成５年度）
③ 石炭燃焼装置からのN_2OおよびNO_xの同時抑制技術に関する研究（平成３年度～平成６年度）
④ 化学還元法を用いた有機性有害化合物の処理に関する研究（平成３年度～平成７年度）
⑤ 深層海水による二酸化炭素の固定に関する研究（平成３年度～平成８年度）
⑥ プラスチック廃棄物中の塩素の除去技術に関する研究（平成４年度～平成７年度）
⑦ 寒冷地バイオ資源の高度利用技術（平成４年度～平成８年度）
⑧ 高性能吸着剤による公害防止技術に関する研究（平成５年度～平成８年度）
⑨ 石炭灰からの高性能脱硫剤の製造に関する研究（平成６年度～平成９年度）
⑩ 有機ハロゲン化合物の無公害化処理に関する研究（平成６年度～平成９年度）
⑪ 石炭燃焼装置における高度炉内脱硫・脱硝技術に関する研究（平成７年度～平成10年度）
⑫ 人工ヒト化細胞を用いた環境変異原物質検出技術の開発に関する研究（平成８年度～平成11年度）

3．国内環境問題と地球環境問題

図２に示すように、環境問題は国内環境問題と地球環境問題とに大別される。国内環境問題は①大気汚染、水質汚濁などの従来型産業公害問題、②森林破壊、野生生物種減少などの自然生態系環境問題および③廃棄物問題などの都市型・生活型環境問題に分類される。一方、地球環境問題は被害、影響が一国内に留まらず、国際的ひいては地球規模にまで広がる環境問題および国際的な取り組みが必要な開発途上国における環境問題であり、①地球温暖化問題、酸性雨問題などのエネルギー系環境問題、②オゾン層破壊問題などの非エネルギー系環境問題、③森林破壊、砂漠化などの自然生態系環境問題および、④発展途上国の公害問題に分類される。

3．1　国内環境問題

3．1．1　従来型産業公害問題

従来型産業公害問題には大気汚染、水質汚濁、土壌汚染、騒音、振動などが含まれる。北工研においては、図１に示したようにこの分野の大気汚染に関して排ガス（SO_2、NOx）・悪臭処理技術、水質汚濁に関して排水処理技術の開発を1960年代から実施してきている。

＊１資源エネルギー基礎工学部

北海道工業技術研究所における環境関連技術開発の概要

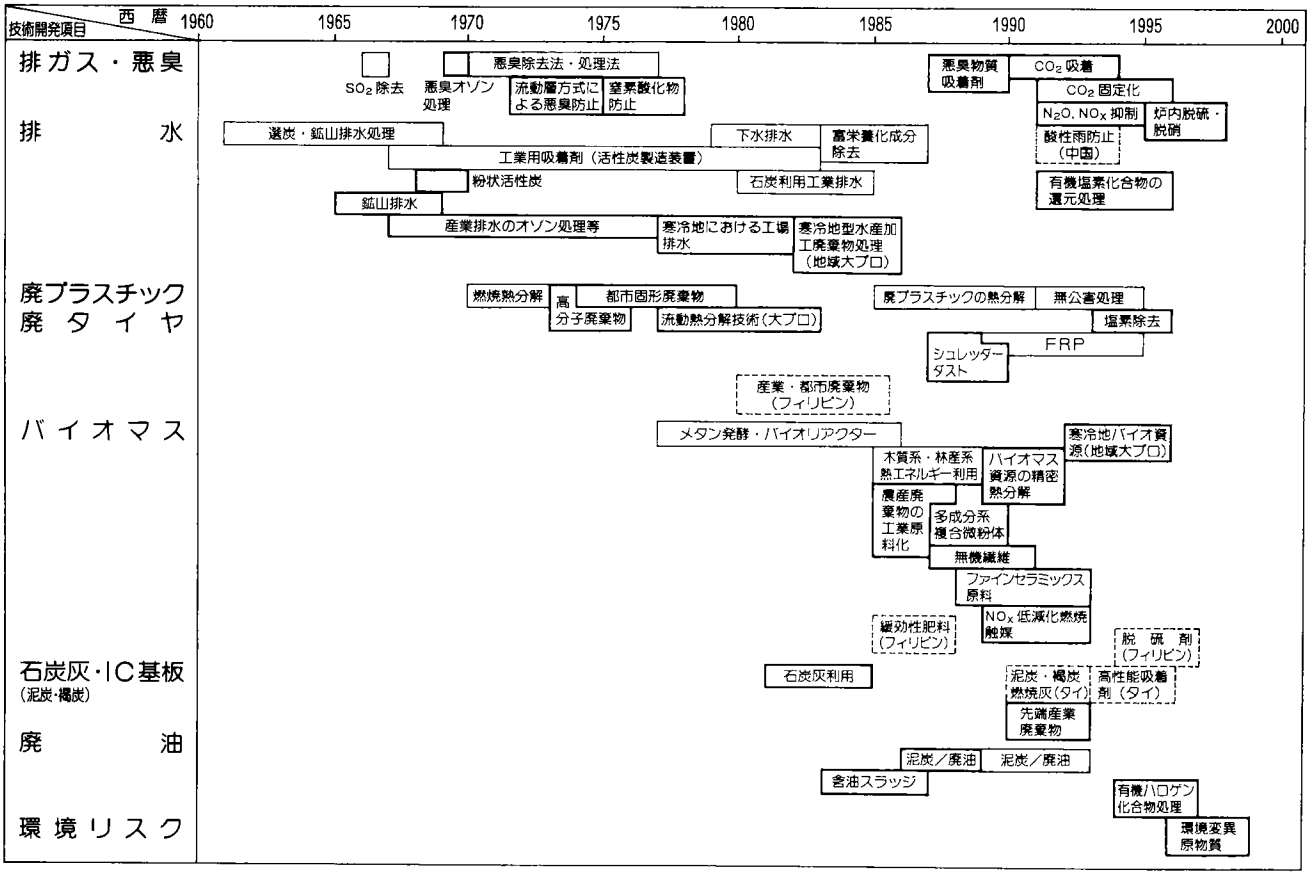

図－1

3．1．2　自然生態系環境問題

この分野での北工研における研究開発については、3．2地球環境問題の3．2．3自然生態系環境問題の項で一括して述べる。

3．1．3　都市型・生活型環境問題(廃棄物問題など)

北工研では、この分野については廃プラスチック、廃タイヤ、バイオマス、石炭灰、IC基板、廃油などの廃棄物処理技術の開発を実施してきている。

1）プラスチック廃棄物

プラスチック廃棄物の再利用法は、サーマルリサイクルとマテリアルリサイクルに大別される。サーマルリサイクルとしては焼却・エネルギー回収、固形燃料化、粉体・スラリー燃料化、油化などに関する技術開発がなされ、マテリアルリサイクルとしてはガス化・メタノール合成、油化・モノマー還元、再生利用などに関する技術開発がなされている。

固形燃料化については、札幌市が北区篠路町にごみ処理能力200t/日の燃料工場を平成2年に建設し、重量比で廃プラスチック10%、木くず40%および紙くず50%の固形燃料（RDF: Refuse Derived Fuel）を生産している[2)]。北工研においては、このようなRDF類の燃焼試験を実施している[3)]。

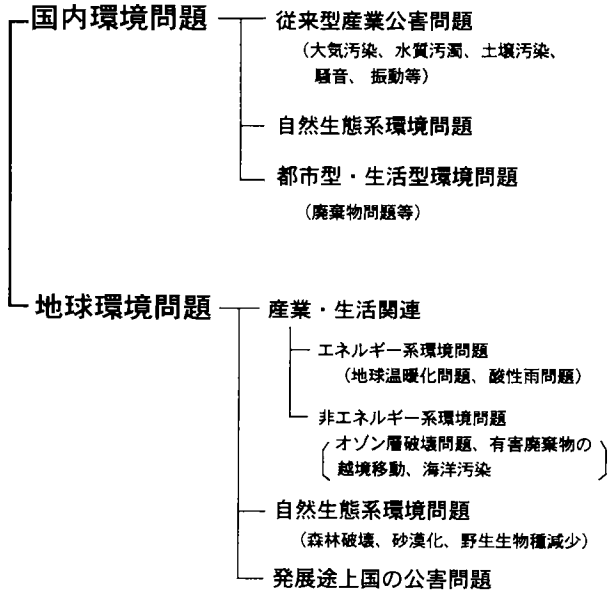

図2．環境問題の分出典：通商産業省環境立地局監修「環境総覧1994」(1993)より

さらに当所では、プラスチック廃棄物の油化技術および含塩素系プラスッチック廃棄物の脱塩素化・減容化技術の開発研究がなされている。当所で開発した二段接触熱分解油化法[4]は、中小企業事業団の平成２年度の「石油代替エネルギー技術開発事業」として採択された都市系混合プラスチック廃棄物を対象とした実験プラント（処理量500ｔ／年、埼玉県桶川市）、および（財）クリーンジャパンセンターの平成３年度国庫補助事業として採択された産業系プラスチック廃棄物を対象とした実験プラント（処理量5000ｔ／年、兵庫県相生市）に活用された。またプラスチック処理促進協会が通商産業省の援助の下で平成９年から操業を開始する「次世代廃プラスチック油化技術開発」プロジェクトの実用化プラント第１号（処理量6000t/年、新潟市）、並びに厚生省の委託の下で廃棄物研究財団が平成９年から実証試験に入る実証プラント（処理量10t/日、東京都立川市）にも二段接触熱分解油化法が活用されている。さらに、塩化ビニル系などの廃プラスチックの含有塩素分析法および脱塩素化・減容化処理法を開発し[5]、都市系を含む廃プラスチックの再資源化のための基盤技術を確立した（図３）。

我が国においても、「容器包装に係る分別収集及び再商品化の促進等に関する法律」（通称：「容器包装リサイクル法」）が平成７年６月16日に公布された。同法では一般廃棄物の容積比で約６割、重量比で約３割を占める容器包装について再生資源としての利用を図るために、容器包装を生産・使用する事業者に対して容器包装の再商品化を、自治体には回収をそれぞれ義務付けている。同法の施行は、ペットボトルとガラスびんについては平成９年４月から、ペットボトル以外のプラスチック製の容器包装と紙製の容器包装については平成12年（2000年）４月から実施される。平成12年４月から実施されるペットボトル以外のプラスチック製の容器包装については、その再商品化に際して燃料として利用する場合は、「炭化水素油」にすることが定められている。このような面からも、現在、廃プラスチックの物理的・化学的性状の把握および油化技術の確立が急がれている。

２）シュレッダーダスト

シュレッダーダストは、廃自動車、廃家電製品等の破砕選別の再資源化工程で発生するプラスチックを多く含む廃棄物であり、従来は安定型埋立処分場に埋め

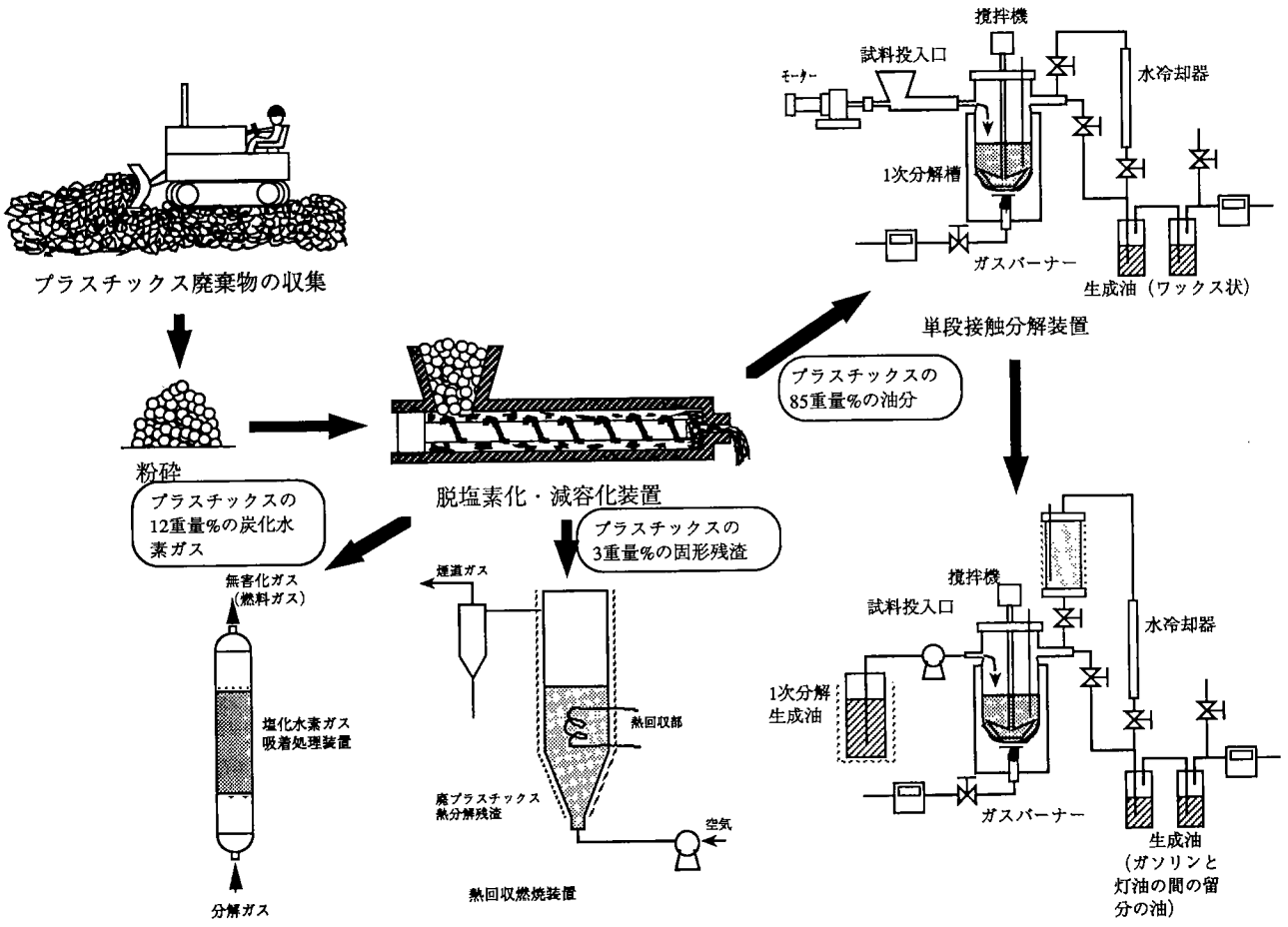

図３．プラスチック廃棄物の脱塩素化・減容化・油化技術

立てられてきたが、シュレッダーダストから重金属浸出の可能性があるため、平成８年４月より管理型埋立処分場に埋め立てることになった。このため、自動車業界などではシュレッダーダストに含まれる鉛などの重金属分の回収やプラスチックその他の燃料化、再資源化、サーマルリサイクル化のための技術開発を本格的に開始した。北工研においては、昭和62年から「シュレッダーダストの処理法および有効利用に関する研究」に着手し、シュレッダーダストの無公害簡易ガス化法およびこれから生成する低カロリーガス燃料によるガスエンジン発電技術を確立し、さらにこれらに基づきシュレッダーダストの無公害処理および有効利用のためのトータルシステムを提案している[6]。

3）石炭灰

石炭灰については、セメント・コンクリート分野（セメント原料など）、建築分野（人工軽量骨材など）、土木分野（アスファルトフィラーなど）、農業・水産分野（肥料、人工魚礁など）、その他分野（排煙脱硫材、融雪剤など）などで実用的資源化あるいは研究開発がなされている。北工研では、石炭灰からの珪酸カリ肥料およびガラス質建材の製造に関する開発研究がなされた[7]。さらに「石炭灰からの高性能脱硫剤の製造に関する研究」（平成６年度～平成９年度）をフィリピンとの共同研究で実施中である。

3.2　地球環境問題

3.2.1　エネルギー系環境問題

エネルギー系環境問題には地球温暖化問題、酸性雨問題が含まれる。北工研では、従来型産業公害研究として1960年代に開始した排ガス・悪臭関連研究が、現在では地球温暖化関連研究（炭酸ガス、亜酸化窒素）および酸性雨関連研究（SOx、NOx）として継承され推進されている（図１）。

1）地球温暖化問題

地球温暖化問題は大気中の温室効果ガス（炭酸ガス、フロン、メタン、亜酸化窒素など）の濃度が増加し、地球規模で気温が上昇することによる異常気象の発生、生態系、国土の保全などへの影響が懸念されているものである。

北工研では、炭酸ガス関連については「循環流動層を用いた排ガス中の二酸化炭素吸着に関する研究」（平成２年度～平成５年度）、「深層海水による二酸化炭素の固定に関する研究」（平成３年度～平成９年度）などを実施している。このうち「深層海水による二酸化炭素の固定に関する研究」においては、深層海水のような低温高圧下で炭酸ガスが水とどのような相互作用を示すのかというのが研究の主目的である。例えば、10℃においても30気圧位の圧力下で炭酸ガスは水と反応してクラスレート（$CO_2 \cdot nH_2O$）という氷状の物質を生成することが判っており、こういった物質の生成条件、物性などに関する研究を実施中である（図４）。さらに「石炭燃焼装置における高度炉内脱硫・脱硝技術に関する研究」（平成７年度～平成10年度）においては、排ガス再循環・酸素付加燃焼による排ガスからの炭酸ガスの分離・回収の抜本的合理化を図っている（図５）[8]。地球環境産業技術研究機構（RITE）などでは炭酸ガスのメタノール転換などの化学的利用に取り組んでいる。フロン関連については、群馬県工業試験場が特定フロンとトリクロロエタンを混合し、高周波プラズマにより分解し、この分解ガスを基板上に析出させることにより絶縁性の重合膜を生成できることを明らかにしている。

また北工研においては、亜酸化窒素（N_2O）関連についても、「石炭燃焼装置からのN_2OおよびNO_xの同時抑制技術に関する研究」（平成３年度～平成６年度）

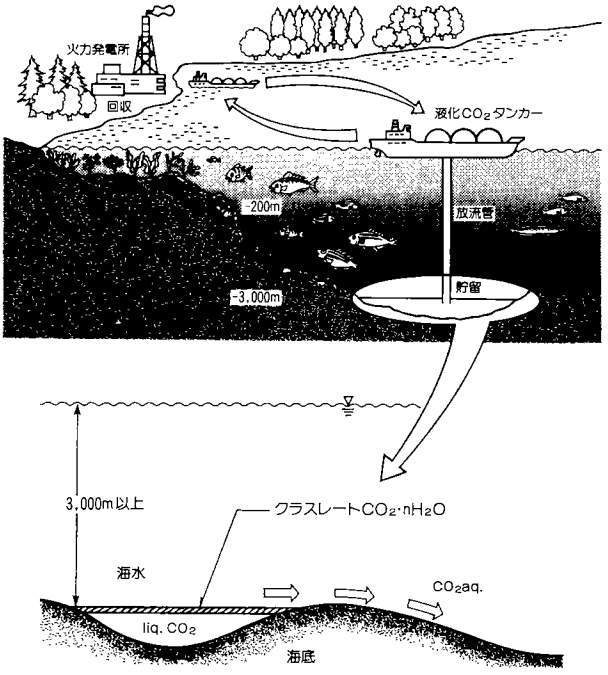

図４．深海に注入された液体CO２の挙動模式図

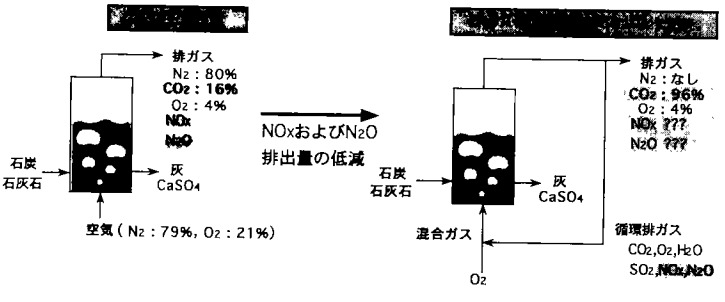

図５．排ガス再循環・酸素付加燃焼法による排ガスからの炭酸ガスの効率的分離・回収法

を実施した。この研究ではN_2Oの発生特性と機構を明らかにするとともに、新たに考案した改良型三段燃焼方式により、一次および二次燃焼域の酸素濃度を適切に制御することにより、N_2Oを85％以上およびNOxを60％以上低減できることを実証している（図６）。

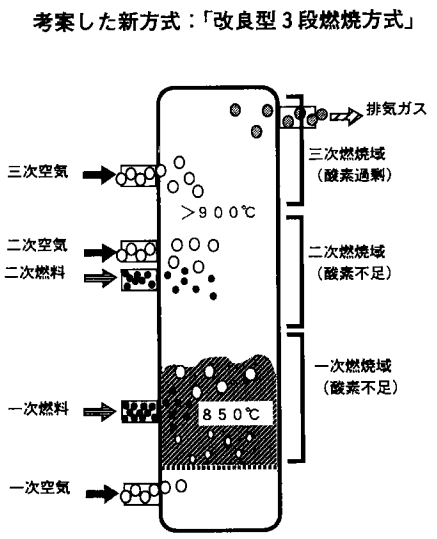

図６．N_2O及びNO_xの同時抑制が可能な改良型三段石炭燃焼技術

２）酸性雨問題

酸性雨問題は大気中に放出された硫黄酸化物（SOx）、窒素酸化物（NOx）などが雲や雨滴に溶解し、酸性化した雨が地表面に降下することにより森林および湖沼における生態系の破壊、文化財・建造物への被害をもたらす問題である。

北工研では、SOx関連については「石炭燃焼に起因する酸性雨の防止技術に関する研究」（平成３年度～平成５年度）を中国との共同研究で、「石炭灰からの高性能脱硫剤の製造に関する研究」（平成６年度～平成９年度）をフィリピンとの共同研究で、さらに「石炭燃焼装置における高度炉内脱硫・脱硝技術に関する研究」（平成７年度～平成10年度）（図５）についても実施中である。

NOx関連については、「群小発生源からNOx低減化のための触媒燃焼技術に関する研究」（平成元年～平成４年）、「石炭燃焼装置からのN_2OおよびNOxの同時抑制技術に関する研究」（平成３年度～平成６年度）（図６）を実施した。

３．２．２　非エネルギー系環境問題

非エネルギー系環境問題にはオゾン層破壊問題、有害廃棄物の越境移動、海洋汚染などが含まれる。

オゾン層破壊問題は冷媒、洗浄剤などに用いられてきた特定フロンなどが成層圏まで上昇し、オゾン層を破壊し、オゾンにより遮断されていた有害な紫外線が直接地表に達し、生態系へ悪影響を及ぼす問題である。

有害廃棄物の越境移動問題は処分費用の高い国から安い国へ、規制の厳しい国から緩い国へと有害廃棄物が不適正に移動されやすく、それに伴う環境問題である。

海洋汚染問題は船舶事故などに伴うオイルなどの流出、河川からの重金属などの有害物質の流入、廃棄物の海洋投棄などによる海洋の汚染が進行している問題である。

３．２．３　自然生態系環境問題

自然生態系環境問題には森林破壊、砂漠化、野生生物種減少などが含まれる。北工研では、この分野については「機能性土壌回復剤による緑化技術に関する研究」（平成２年度～平成５年度）をフィリピンとの共同研究で実施した。この研究は、熱帯雨林の伐採や家畜の放牧などにより荒廃した土壌に肥料成分や土壌活性化物質などを含んだマイクロカプセル（図７）を撒布することにより、森林あるいは緑地を回復することを目的に実施された。このような観点からの技術開発は、砂漠緑化、耕地面積の増大、森林回復などによる食糧問題、炭酸ガス問題の解決にも関連しており、21世紀に向けて重要視されるべきであろう。

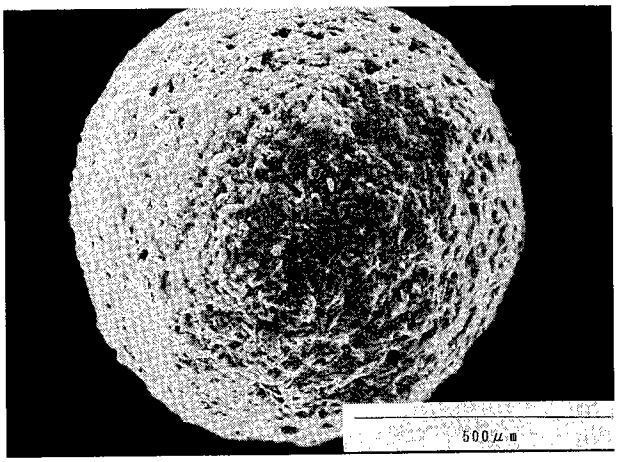

a）マイクロカプセルのSEM写真

b）マイクロカプセル表面細孔のSEM写真

図７．マイクロカプセルのSEM写真

3．2．4　発展途上国の公害問題

工業化や人口の都市集中に伴い公害問題が発展途上国にも発生し、国際協力による解決が望まれている。

北工研においては、これまで国内環境問題対策技術として開発してきた種々の技術が、現在は発展途上国の公害問題対策技術として対象国の実状に即した研究開発を目指して継承、推進されている。大気汚染、水質汚濁関連技術では、「高性能吸着剤による公害防止技術に関する研究」（平成５年～平成８年度）をタイとの共同研究で、廃棄物資源化技術については、「産業および都市廃棄物の熱分解による資源化に関する研究」（昭和55年度～昭和59年度）および「フィリピン産白雲石灰石と籾殻を主原料とする緩効性肥料の研究」（昭和60年度～昭和62年度）をフィリピンとの共同研究で、「低品位泥炭・褐炭の活性化処理技術に関する研究」（平成２年度～平成４年度）をタイとの共同研究で、SOx関連については、「石炭燃焼に起因する酸性雨の防止技術に関する研究」（平成３年度～平成５年度）を中国との共同研究で、「石炭灰からの高性能脱硫剤の製造に関する研究」（平成６年度～平成９年度）をフィリピンとの共同研究で、NOx関連については、「流動層による石炭の新燃焼技術に関する研究」（昭和63年度～平成２年度）を中国との共同研究で、森林破壊防止・緑化技術については、「機能性土壌回復剤による緑化技術に関する研究」（平成２年度～平成５年度）をフィリピンとの共同研究で実施してきている。

4．リサイクル社会の実現を目指した動き

家電製品およびワープロや複写機などのOA機器を中心に、最近の新しい方向として使用済みの製品・機器を回収・分解して再利用しようという動きが活発化し、それに伴いリサイクルを考慮した製品開発がなされている。このようなリサイクルを考慮した製品開発の分野では、リサイクルのみならず地球環境保全をも考慮したインバースファクトリー[9)10)]、エコファクトリー[11)]、エコマテリアル[12)]などの構想が提案されている。

4．1　インバースファクトリー（逆工場）[9)10)]

インバースファクトリーまたはインバースマニュファクチヤリングは、廃棄物のリサイクル・無公害化などを強く意識した製造技術で、「製造工場」に対して「逆工場」と呼ばれている。東京大学、MIT、スイス連邦工科大学（ETH）などの国際学術協力の成果として提案されたが、具体的にどのような要素技術が総合化されて循環型経済社会での新しい工学体系となるのかは、今後の検討を待たなければならない。

4．2　エコファクトリー（Ecology-Based Factory あるいはEcologically Conscious Factory）[11)]

エコファクトリーは、通商産業省工業技術院機械技術研究所などで、工業生産分野での経済的および技術的発展の活性を損なうことなく地球環境問題解決にも寄与しうる次世代技術として検討されている。その概念は、工業生産活動と地球生態系との調和であり、さらに工業生産系は「生産系工場」と「還元系工場」とで構成され、資源・エネルギーの消費・廃棄に伴う地球生態系への負荷を可能な限り軽減化することを目標としている。ここで「還元系工場」を主に構成するのは、廃棄された組立製品の「解体技術」と解体品をリサイクルするための「材料再生技術」である。

4．3　エコマテリアル[12)]

エコマテリアルは、材料開発に関する新しい考え方であり、これまでの材料の機能・性能に加えて、その材料の製造段階から輸送、販売、使用さらに廃棄に至る全ての段階にわたって、消費エネルギー、二酸化炭素排出量など環境への負担の大きさを算定し、それらを少なくするような材料・技術を開発することを目標としている。平成５年から科学技術庁の科学技術振興調整費による総合研究「材料のエコマテリアル化のための評価設計技術の確立に関する研究」が、通商産業省、農林水産省、科学技術庁および環境庁傘下の研究所、大学および民間企業が参加し、開始されている。このプロジェクトの主な研究内容は、１）物質循環を念頭に置いたリサイクルしやすい材料の設計、２）自然と融合可能な物質・材料の開発、および３）開発している材料の評価指標の確立、などである。このうち３）の評価指標の確立に関連して、その有力な評価手法として注目されているのがLCA（ライフサイクル・アセスメント）[13)]である。LCAは製品の生涯にわたる環境負荷を総合的・定量的に評価する手法であり、国際標準化機構（ISO）で国際規格化が検討され、その成果がISO14040として発効する見込みである（図８）。

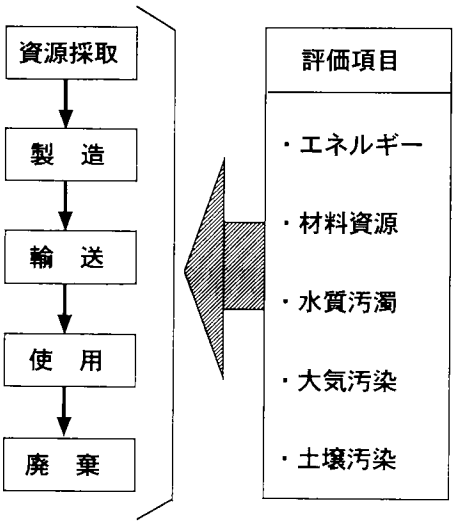

図８．ISOが検討しているライフサイクル・アセスメント規格の概要

4.4　ゼロ・エミッション計画（ZERI）

またリサイクル社会の実現を目指した具体的な動きとしては、国際連合大学のゼロ・エミッション計画（ZERI）の構想が挙げられる[14]。ゼロ・エミッション計画では、様々な産業を組み合わせてA社の廃棄物をB社の原材料として用いるといったように廃棄物を無くした無駄のない循環型産業構造の確立を目指し、

1）養殖漁業とビール醸造業との組み合わせ
2）砂糖を原料にしたプラスチック、洗剤、紙などの開発
3）林業の廃棄物である枝や葉から香水や防腐剤などを製造する技術
4）紙のリサイクル率向上とインクの完全分離リサイクルなど製紙・パルプ業界の技術革新
5）金属加工、プラスチック産業の廃棄物の建設資材などへの転換
6）蝶の鱗粉などを利用した新しい色素の開発など合成染料に代わる光の屈折による発色法の開発
7）テレビ受像器に使う水銀の回収
8）合成ワックスの代替品として鳥の羽の油の分子構造を応用する研究

などのプロジェクトを提案している。なかでも同大学がその実現を期待しているのが、1）の養殖漁業とビール醸造業との組み合わせであり、これはビールの醸造過程で排出されるビール酵母の滓や排水、およびビール瓶を洗浄した排水を魚を養殖するための用水や餌として利用し、魚の糞を藻類の栄養分とし、その藻類を魚が食べることで完全循環型の生産システムを完成させる。平成9年度を目途にコロンビアとネパールに実験工場を設置し、平成10年には中国の青島に商業プラントを建設する計画である。

我が国においては、鹿児島県屋久島において「ゼロエミッション構想」が動き出しており、2000年前後から段階的に化石燃料を太陽光、風力、波力などの自然エネルギーに転換し、自動車を電気自動車に転換し、廃棄物については生ごみのたい肥化や可燃ごみの固形燃料化を図り、林業から排出されるおがくずをきのこ栽培に利用し、木粉からは芳香剤や抗菌剤を作ることなどを計画している。

5．地球環境保全を目指して

現在、地球社会が直面している資源・エネルギー・食糧、環境、経済成長のトリレンマ問題は、人口の急増が予測される21世紀においては益々厳しいものとなると考えられる[15),16)]。21世紀において地球社会が持続的成長を遂げるためには、科学技術が果たす役割は極めて重要であり、

- エネルギー資源の探索、貯蔵、転換：自然エネルギー、水素エネルギーなど
- 省エネルギー・未利用エネルギーの有効利用・効率向上
- 食糧の確保：砂漠緑化、耕地面積の増大
- 地球環境の保全：　炭酸ガス削減対策、森林回復、環境リスク、バイオエンジニアリングなど

などの技術開発の継続、推進が望まれる。

5.1　省エネルギー・未利用エネルギーの有効利用・効率向上

この分野においては、現在、1）車の走行距離の向上（低燃費化）・低公害車、2）熱電変換技術、低温エネルギー輸送技術などの環境温度に近い熱エネルギーの利用および輸送（エネルギー利用効率向上、熱汚染防止）、および3）発電プラントの変換効率向上などの技術開発が進行している。

このうち、低燃費乗用車については米国、欧州および日本において直噴エンジンの開発を軸に3リッターで100ｋｍ走行可能な「3リッターカー」の開発が進行している。一方、低公害車については、米国カリフォルニア州が2003年以降州内で販売される車の1割を「排ガスゼロ車（ZEV）」にしなければならないという「排ガスゼロ車規制」の導入を決定したところから、電気自動車が脚光を浴び、日米でニッケル水素電池やリチウムイオン電池など電気自動車用電池を中心に活発な技術開発が進行している。

5.2　環境リスク

環境リスクとは、人の活動（例えば、化学物質など）によって環境に加えられる環境への負荷が、環境中の経路を通じてある条件のもとで、人の健康や生態系に影響を及ぼす可能性を示す概念と定義されている。このように環境リスクは、「人の健康リスク」と「生態系へのリスク」に大別されるが、一般的には化学物質などによる「人の健康リスク」を意味しており、リスクを与える化学物質を発ガン性物質と非発ガン性物質に分類し、前者はガンになる確率で、後者は人体に影響を及ぼさない最大量で評価する。

この分野について、北工研では平成8年から「人工ヒト化細胞を用いた環境変異原物質検出技術の開発に関する研究」を開始している。環境中に存在する変異原物質の多くは人の肝臓で酵素により活性型変異原物質に変換され、突然変異、細胞致死などを発現する。従来の変異原性試験においては、人の肝臓機能の代替としてラットの肝臓機能を用いてきている。本研究においては、人に対するリスクを正しく評価するために、人の肝臓が有する変異原物質活性化酵素の遺伝子をハムスターなどの細胞に組み込み、人の肝臓の変異原物質活性化機能をシミュレートする人工ヒト化細胞を作製し、これを用いて環境変異原物質を検出する技術を開発することを目的としている（図9）。

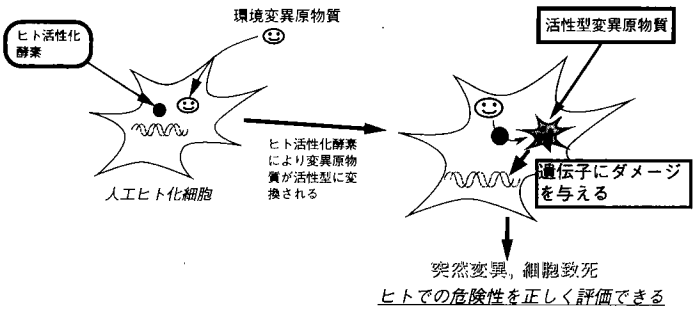

図９．人工ヒト化細胞による変異原物質検出法

５．３　グリーン調達とISO14000

環境負荷に対する配慮が、ビジネスの世界でもヨーロッパを中心に「グリーン調達」という形で始まっている。これは、製品の調達に際して、環境対策を徹底している企業の製品を優先的に購入しようという動きである。例えば、フィンランドのある企業が日本の電機メーカーに示した「グリーン調達」に関連する指針は、①環境管理システムはあるか？、②廃棄物管理とリサイクル計画はあるか？、③寿命を終えた製品のリサイクルシステムはあるか？、④環境に影響を与える事故などの非常事態に対する備えはあるか？、などであり、我が国の輸出企業にとって環境保全対策は備えるべき重要な条件となってきている。

このように企業が環境保全対策を進める際の管理・監査手法を、国際的に統一しようと国際標準化機構（ISO）が作成作業を進めているのがISO14000である。その内容は、

１）環境管理システム
２）環境監査
３）エコラベルの設定
４）対策の度合いをチェックする環境パーフォーマンス評価
５）製品の製造から廃棄までの環境への影響を調べるライフサイクル・アセスメント（LCA）

の５項目からなり、このうち１）環境管理システムおよび２）環境監査については平成８年９月から10月にかけて発効した。これらは目標設定、計画立案、実行、目標達成度のチェックという一連のシステムを作り、その成果を環境監査で評価することを規定しており、通商産業省工業技術院は平成８年10月20日に同じ内容を日本工業規格（JIS）に取り込んでおり、我が国においても企業の環境管理システム構築と環境監査が本格的に始まる。

６．おわりに

人類は、20世紀における未曾有の活発な経済活動により地球温暖化、酸性雨、オゾン層破壊、森林破壊、砂漠化などの地球環境に対する禍根を残すこととなった。21世紀において地球社会の持続的成長を可能とするためには、個々人、地域社会、企業（産業界）、国および国際社会が環境に配慮したライフスタイルを構築するとともに科学技術による地球環境の健全化が求められる。

参考文献

1）北海道工業開発試験所技術資料、第14号、平成４年７月（工業技術院北海道工業開発試験所）
2）三浦広仁、廃棄物学会誌、**7**，316（1996）
3）成川公史、陳　勇、山崎量平、森　滋勝、平間利昌、細田英雄、藤間幸久、化学工学論文集、**22**，1408（1996）
4）斉藤喜代志、北海道工業開発試験所報告、第51号、p.23（1991）
5）斎藤喜代志、ケミカル・エンジニアリング、**39**(1)，40（1994）
6）北海道工業開発試験所報告、第52号（「シュレッダーダストの処理法および有効利用に関する研究」特別研究報告書）、平成３年３月（工業技術院北海道工業開発試験所）
7）北海道工業開発試験所報告、第37号（「石炭灰の燃焼過程における残渣の活性化処理技術に関する研究」特別研究報告書）、昭和60年12月（工業技術院北海道工業開発試験所）
8）清水忠明、平間利昌、細田英雄、北野邦尋、ケミカル・エンジニアリング、**41**(8)，51（1996）
9）日刊工業新聞、平成７年２月24日付
10）日経産業新聞、平成７年４月25日付
11）井上英夫、工業技術、**33**(5)，1（1992）
12）古林英一、化学工業、**46**，185（1995）
13）森下研、廃棄物学会誌、**6**，85（1995）
14）日経産業新聞、平成６年７月19日付
15）依田直、斎藤眞人、工業技術、**34**(12)，1（1993）
16）S. Ono, Proceedings of The 5th China-Japan Symposium on Coal and C_1 Chemistry, Huangshan,China, May 13-16, 1996, p.1

Characterization of Silicon Carbide-Silicon Nitride Composite Ultrafine Particles Synthesized Using a CO_2 Laser by Silicon-29 Magic Angle Spinning NMR and ESR*1

(Key Words : Silicon carbide, Silicon nitride, Ultrafine particles, CO_2 laser, MAS-NMR, ESR)

Masaaki SUZUKI*2, Yoshihisa HASEGAWA*3, Masayuki AIZAWA*2, Yoshinori NAKATA*2, Takeshi OKUTANI*2, and Kohei UOSAKI*4

1. Introduction

High-resolution solid-state magic angle spinning nuclear magnetic resonance (MAS-NMR) spectroscopy has become a powerful and popular tool for investigating the local structures of solid materials. Most of the applications to date have been in organic systems such as polymers.

Recently, the MAS-NMR is finding new applications in solid inorganic systems such as silicate and zeolitel). In addition, this technique is also useful for the study of non-oxide materials[2,3].

In last few years, a number of NMR investigations about the structure of SiC and Si_3N_4 have been reported. Most of them were concerned with well-known structures such as α- and β-SiC and α- and β-Si_3N_4 and their polytypes[4-10]. Other studies were done to characterize the commercial products[5,11,12] and to investigate the behavior of boron used as a sintering aid for SiC[13]. These studies revealed that high resolution solid state NMR was a powerful and useful method for the study of ceramic materials, because of its high sensitivity to the local structure. Moreover, NMR is a bulk analysis technique. Information can be obtained with regard to the local structure over the entire sample under study, which is notably different from other surface analysis methods such as X-ray photoelectron spectroscopy (XPS).

In our previous paper[14], we have reported the synthesis of silicon carbide-silicon nitride (SiC-Si_3N_4) composite ultrafine particles. The results of XPS, lattice constant measurement and electron energy loss spectroscopy (EELS) have indicated that Si, C and N atoms were intimately mixed in the composite powder. In this paper, we have applied the ^{29}Si MAS-NMR technique to clarify the local structure of the SiC-Si_3N_4 particles.

2. Experimental Procedure

The powders were synthesized by irradiating SiH_4, C_2H_4, NH_3 gas mixtures with CO_2 laser at atmospheric pressure. In this study, NMR spectra were taken for the powders prepared at a laser power density of 0.92 kW/cm^2 and beam diameter of 4 mm. Preparation of SiC-Si_3N_4 ultrafine powders was described in Ref.14 and 15 in detail.

The crystalline phases of the powders were analyzed by X-ray diffraction (XRD) and the mean crystalline sizes were determined by the line width of diffraction line (Scherrer's method)[14].

Solid-state ^{29}Si MAS-NMR spectra were acquired at 53.7 MHz using a JNM-GX270 spectrometer (JEOL). The samples were packed into 17mm height x 5 mm diameter zirconia rotars with polyimide endcaps.

The spinning speed was between 5.7 and 6.2 kHz. The spectra were obtained following 90° pulse (4.5 ms, pulse width)

* 1 This paper was reproduced from Journal of the American Ceramic Society.Vol.78,No.1(1995)pp83-89 by the permission of the American Ceramic Society.

* 2 Materials Division
* 3 Ressources and Energy Division
* 4 Hokkaido University

All the chemical shifts were quoted relative to the signals for tetramethylsilane, although secondary external reference (poly-dimethylsilicone, -22 ppm) was used. The line width (FWHM) was determined from the spectra without broadening factor, while the spectra with broadening factor were shown in the figures to improve S/N ratio. The spin-lattice relaxation time (T_1) was defined by nonlinear inversion recovery (IR) method[16].

T_1 was measured for the several representative samples, and were in the range from 9.0 to 49.5s. It was considered that a relaxation delay of 5 times T_1 was long enough for the resulting spectra to be quantitatively representative of the sample[4]. Even though we did not measure T_1 for all samples, it was unlikely that T_1 value of other unmeasured samples showed extremely longer value than 49.5 s. Therefore, pulse delay (PD) of 300 s was considered to be long enough to get the quantitatively representative spectra. Most NMR spectra were taken at pulse delay of 400 s to make sure the quantitativity. In some cases, PD = 60 and 300 s were used to save measuring time. In any case, the condition at a relaxation delay of 5 times T_1 was satisfied.

ESR spectra were obtained using JES-FE3X spectrometer (JEOL) with a standard rectangular x-band cavity at 303 K. The samples of 3 to 15 mg were used for ESR measurement. The microwave power was 0.2 mW and it was confirmed that ESR signal was not saturated at 0.2 mW by changing the microwave power. The spin concentrations of the powders were measured using 0.25 mg solid DPPH as a standard.

Fourier transform photoacoustic emission spectra (FT-PAS) of the powders were obtained using FTS-65 (Bio-RAD) spectrometer.

3. Results

3-1. NMR

3-1-1. SiC and low N content composite powders

Figure 1 shows the ^{29}Si NMR spectra of ultrafine SiC powder synthesized by laser and the change of the spectra by introducing nitrogen into SiC powder. The NMR spectrum of ultrafine SiC powder exhibited one main peak (-15.9 ppm) and two shoulders (-20.3, -24.8 ppm). The main peak position agreed well with that

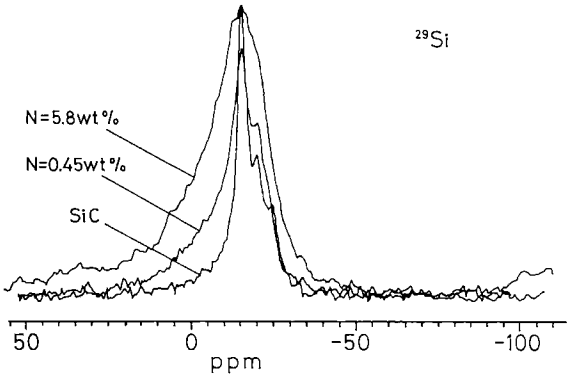

Fig. 1 ^{29}Si NMR spectrum of ultrafine SiC powdersynthesized by laser and the change of ^{29}Si NMRspectra by introducing nitrogen into SiC powder. The spectra were taken at the following condition;SiC; a pulse delay (PD) of 400 s, line broadening (LB) of 20 Hz and 148 scans.N = 0.45 wt%; PD = 60 s, LB = 10 Hz, 200 scan.N = 5.8 wt%; PD = 400 s, LB = 50 Hz, 168 scan

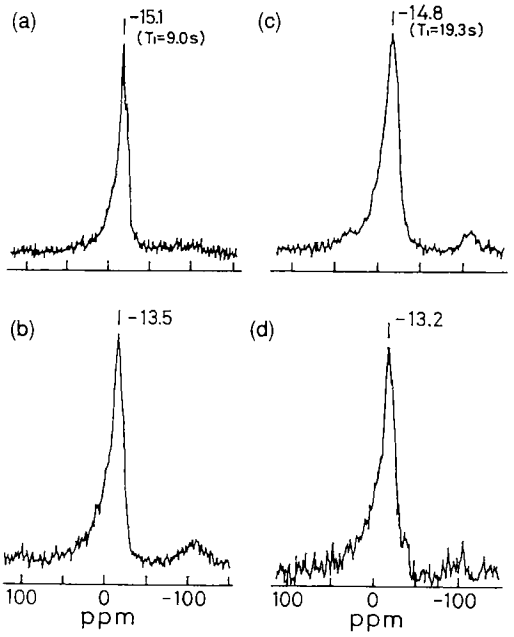

Fig. 2 ^{29}Si NMR spectra of low N content $SiC-Si_3N_4$ composite powders synthesized using a laser. (a) N = 0.45 wt%, C = 27.0 wt%, PD = 60 s, LB = 10 Hz, 200 scans (b) N = 2.6 wt%, C = 27.2 wt%, PD = 400 s, LB = 50 Hz, 269 scans (c) N = 5.8 wt%, C = 25.3 wt%, PD = 400 s, LB = 50 Hz, 168 scans (d) N = 10.3 wt%, C = 19.5 wt%, PD = 400 s, LB = 50 Hz, 168 scans

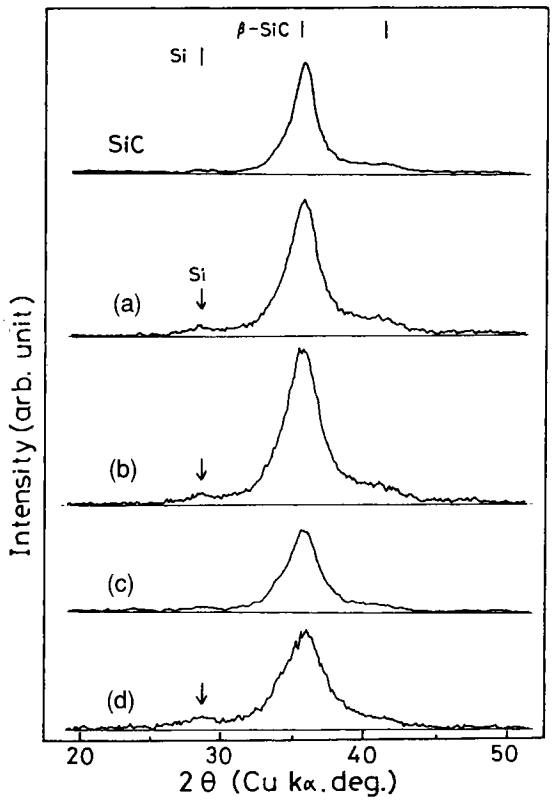

Fig. 3 X-ray diffraction patterns of SiC ultrafine powder and low nitrogen content SiC-Si_3N_4 composite powders synthesized using a laser. (a) N= 0.45wt%, C=27.0wt% (b) N=2.6wt%, C =27.2wt% (c) N =5.8wt%, C=25.3wt% (d) N =10.3wt%, C=19.5wt%

of β-SiC and the positions of two shoulders agreed well with those of a-SiC[9,10]. While X-ray diffraction (XRD) pattern showed only a broad β-SiC pattern (Fig. 3), the NMR spectra indicated that the ultrafine SiC powder synthesized by the laser consisted of mainly β-SiC and small quantity of α-SiC. The line width (FWHM) of the main peak at -15.9 ppm, which was determined without precise peak deconvolution, was approximately 3.0 ppm. The spin-lattice relaxation time, T_1 was estimated to be 18.8 s for the ultrafine SiC powder.

Figure 2 shows the ^{29}Si NMR spectra of low nitrogen content SiC-Si_3N_4 powders. Figure 3 shows the XRD patterns of these powders. The XRD patterns of these powders were similar and showed broad b-SiC patterns. A very small and broad peak of Si was observed in a few powders (Fig.3 (a), (b), (d)). The NMR spectrum of SiC-Si_3N_4 composite powder

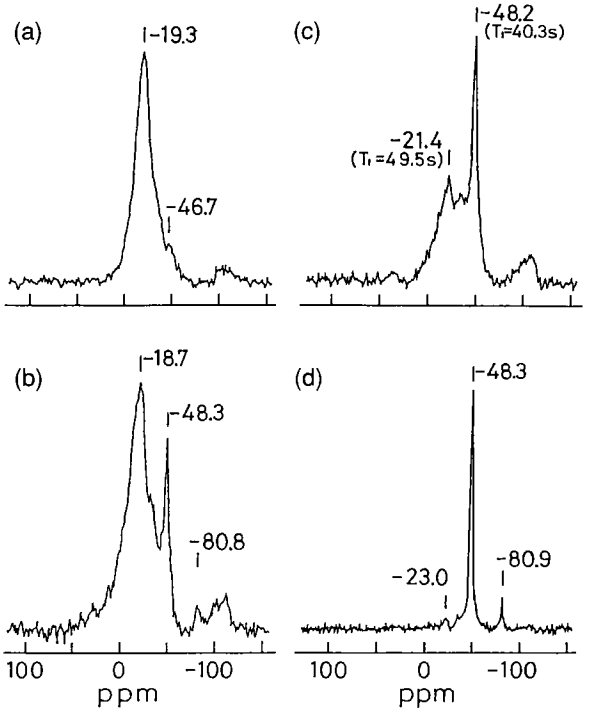

Fig. 4 ^{29}Si NMR spectra of high nitrogen content SiC-Si_3N_4 composite powders synthesized using a laser. (a) N = 13.1wt%, C = 17.9wt%, PD = 300s, LB = 50Hz, 160scans (b) N = 19.5wt%, C = 11.5wt%, PD = 400s, LB = 50Hz, 200scans (c) N = 28.0wt%, C= 6.7 wt%, PD = 400s, LB = 50Hz, 100scans (d) N = 30.9 wt%, C = 2.8wt%, PD = 300s, LB = 10Hz, 60scans

with nitrogen content of 0.45 wt% (Fig.2 (a)) was similar to that of ultrafine SiC powder (Fig.1). It exhibited a main peak at -15.1 ppm and a shoulder peak at -19.9 ppm, while the wltrafine SiC Showed two shoulder peaks. The component of low magnetic tield (between-5 and +30 ppm) inceneased compared to the case of ultvafine SiC powder. In the case of the powder with N content of 2.6,5.8and 10.3wt% (Fig.2(2),(c).and(d)),the NMR spectra weve guite similar to each other They exhibited a main peak between -14.8 and -13.2 ppm and had broad components at low magnetic field (between -5 and +30 ppm). These NMR spectra of the composite powders showed small broad peaks around -100 ppm, which came from sica of the surface oxide layer. The T_1 values of the NMR peaks were 9.0 s for 0.45 wt% N content and 19.3 s for 5.8 wt%.

3-1-2. High N content composite powders

Figure 4 shows ^{29}Si NMR spectra of high nitrogen content SiC-Si_3N_4 powders. Fi-

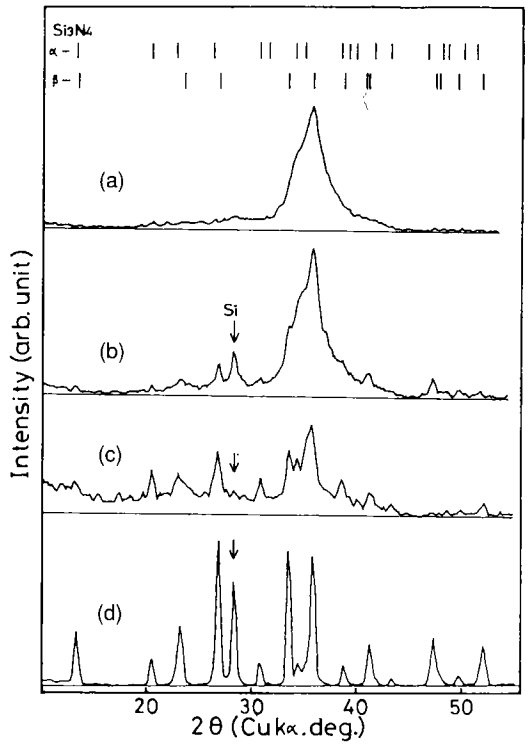

Fig. 5 X-ray diffraction patterns of high nitrogen content SiC-Si_3N_4 composite powders. (a) N=13.1 wt%, C=17.9wt% (b) N=19.5wt%, C=11.5wt%, (c) N=28.0wt%, C=6.7wt% (d) N=30.9wt%, C=2.8 wt%

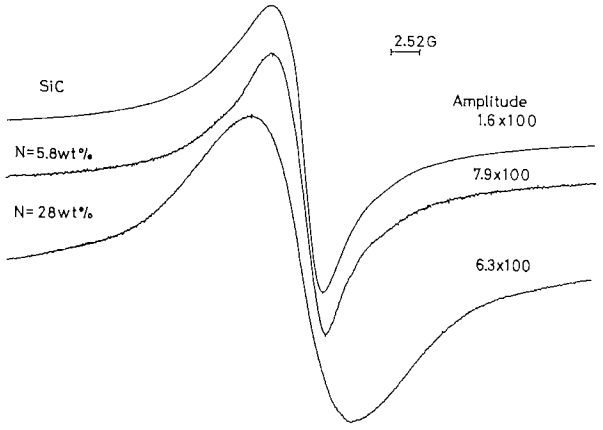

Fig. 6 Typical ESR spectra of SiC and SiC-Si_3N_4 ultrafine composite powders synthesized using a laser. microwave power: 0.2 mW, modulation: 100 kHz, 0.4 G temperature: 303 K

gure 5 shows their XRD patterns. Crystalline Si_3N_4 phase clearly appeared above 19.5 wt%. The XRD pattern of the powder of Fig. 5(a) showed a broad β-SiC pattern including very small amorphous component, which was observed as a base line increase at a very wide range from about 20 to 45 degrees. The NMR spectrum showed a main broad peak at -19.3 ppm and a small shoulder at -46.7 ppm, which corresponded to Si_3N_4[6]. The low magnetic field component (between -5 and 30 ppm) became very small. The XRD pattern of the powder of Fig. 5(b) was the mixture of broad β-SiC pattern, crystalline Si_3N_4, small Si peak and a small amount of amorphous component. The NMR spectrum showed a broad peak at -18.7 ppm and a relatively sharp peak at -48.3 ppm (FWHM, approximately 10 ppm). In addition, it contained a small peak at -80.8 ppm and around -110 ppm, which corresponded to elementary silicon and silica, respectively. As the nitrogen content increased and reached 28.0 wt% (Fig 5(c)), crystalline Si_3N_4 increased and SiC decreased in the XRD pattern. In addition, an amorphous phase was observed more clearly. The NMR spectrum showed that the peak at -21.4 decreased and the peak at -48.2 ppm increased and became a little sharper (FWHM, approximately 6.3 ppm). When the nitrogen content was 30.9 wt% (Fig.5 (d)), XRD pattern was the mixture of sharp a-Si_3N_4 and b-Si_3

The T_1 values of the two peaks in Fig.4 (c) were estimated to be 40.3 s for -48.2 ppm, and -49.5 s for -21.4 ppm, respectively.

3-2. ESR

ESR spectra were taken for these ultrafine powders. Figure 6 shows the typical ESR spectra of SiC and SiC-Si_3N_4 composite ultrafine powders synthesized using the laser. These powders showed strong ESR signals, which indicated that these powders had a lot of paramagnetic defects. The ESR spectra of the powders exhibited a single line shape without any satellites and shoulders, even though the spectra of SiC and low nitrogen content SiC-Si_3N_4 were somewhat asymmetric.

Table 1 lists the g value, peak to peak line width (ΔHpp) and spin concentration (Ns). No correlation could be drawn between nitrogen content and paramagnetic spin concentration. The Ns of SiC-Si_3N_4 powders were smaller by at least one order of magnitude than nitrogen content of the powder. For example, the Ns of the powder with nitrogen content of 0.45

Table 1. g Value Spin Concentration and Peak-to-Peak Line Width of ESR Spectra of SiC and SiC-Si_3N_4 Composite Powders

Sample	g value	Spin conc. (spings/g)	Peak-to-peak line width ΔHpp(G)
SiC(commercial)	2.0026	1.0×10^{18}	4.6
SiC	2.0027	1.1×10^{19}	5.1
SiC-Si_3N_4			
N=0.45wt%	2.0030	1.1×10^{19}	5.4
N= 5.8wt%	2.0025	1.9×10^{18}	4.9
N=11.0wt%	2.0026	4.8×10^{18}	5.6
N=13.1wt%	2.0026	3.4×10^{18}	5.0
N=19.5wt%	2.0025	8.9×10^{17}	8.5
N=28.0wt%	2.0025	1.9×10^{19}	8.5
N=30.9wt%	2.0025	3.9×10^{19}	10.5

wt% (0.66 mot%) was 0.037 mot% and the Ns of the powder with nitrogen content of 30.9 wt% (45.8 mot%) was 0.13 mol%. This fact revealed that most of nitrogen in the composite powders were present in a non paramagnetic form.

4. Discussions

4-1. NMR

4-1-1. SiC and low N content composite powders

Carduner et al.[11] have studied seven commercial β-SiC powders. From the results of Carduner, it seemed that there were typically two kinds of powders. A kind of powders showed broader NMR spectra (FWHM 5 to 6 ppm) with peak maxima at about -18 to -19 ppm. The other kind of powders showed relatively narrower peak (FWHM 0.8 ppm) with peak maxima at -16 ppm. They showed that the existence of much stacking faults broadened the spectra and shifted the peak position towards high magnetic field. But our laser synthesized SiC powder seemed to be different type from those reported by Carduner, because it showed a relatively broad (FWHM, approximately 3.0 ppm) peak at -15.9 ppm. This laser synthesized SiC powder consisted of very fine particles and the mean crystalline size was 4.4 nm[14]. This powder might have many defects besides stacking faults, or contain amorphous phase. Crystal imperfections as well as amorphous phase seemed to broaden the NMR spectrum[5]. The very similar spectra were observed in polymer derived SiC[17] and SiC based materials[18].

The spin-lattice relaxation time, T_1 was estimated to be 18.8 s for the ultrafine SiC powder. In general, the NMR relaxation time is dependent on molecular motion, but in the case of solid systems molecular motion is not vigorous enough to be efficient. Therefore, silicon carbide generally has long T_1 values. The longest T_1 value of 35 ±4 min was reported for highly pure 6H-SiC_4). Our laser-synthesized ultrafine SiC showed a very short T_1 value. In addition, SiC-Si_3N_4 composite ultrafine powders showed very short T_1 values. The ultrafine powders had a lot of paramagnetic defects, which are shown in the ESR results. Because the relaxation probably occurred via paramagnetic centers[4,12], these ultrafine powders showed short T_1 values.

It was interesting to take MAS-NMR spectra at different relaxation delays, because it was expected that the species in the vicinity of paramagnetics showed faster relaxation time. The information on distribution or local structure in the vicinity of paramagnetics might be obtained by taking MAS-NMR spectra at shorter pulse delays. The powder of 5.8 wt% nitrogen content (T_1 = 19.3 s) was measured at PD = 400, 20, 5 seconds. These NMR spectra were the same and any difference was not observed. Further investigation would be needed to get the information about the local structure in the vicinity of paramagnetics by NMR measurements at shorter pulse delays.

It was expected that a relationship between Ns and T_1 might be observed, because it was considered that spin-lattice relaxation would occur via paramagnetic centers. However, any distinct relationship between them was not observed. The spin concentration of our laser synthesized powder were in the range from 8.9 x 1017 to 3.9 x 1019 spins/g. All the Ns of powders, even a 8.9 x 1017 spins/g, might be too high to exhibit the different effects on T_1.

As illustrated in Fig.1, the low magnetic field component was increased by introducing nitrogen. The mean crystalline sizes of SiC in these composite powders were in the range from 2.4 to 4.3 nm and they were almost the same size as that of ultrafine SiC powder. Therefore, the degree of broadening by small crystalline size was expected to be the same as that of SiC ultrafine powder. The low magnetic field component in NMR spectra suggested that there existed Si atoms with different structure from SiC.

The chemical shift value of low magnetic field component was different from those of SiC, Si_3N_4, SiO_2 and Si. In addition, it was difficult to determine the structure around Si atoms, with a low magnetic field shift, by comparing the chemical shift with those of the standard inorganic materials. This is because there are few standard inorganic materials, which consist of silicon, carbon and nitrogen atoms and have structurally and chemically well known phases.

In the field of organosilicon compound, a lot of ^{29}Si NMR data is available. The chemical shift of SiC-Si_3N_4 powder was compared with those of organosilicon compounds to determine the local structure around Si atoms in the composite powders. In general, ^{29}Si chemical shift is affected by not only the nearest neighbor atoms but also the next nearest neighbor atoms. It was necessary to take into account both the nearest and the next nearest neighbor atoms for precise interpretation of ^{29}Si chemical shift. However, the nearest neighbor atoms have greater effect on chemical shift than the next nearest neighbors. As the first approximation, only the nearest neighbors were taken into consideration. In β-SiC crystal, Si atom is surrounded by four C atoms. Therefore, organosilicon compounds, which have a Si atom surrounded by four C atoms, such as $(CH_3)_4Si$, and their substituted could be used as reference materials.

The chemical shift of $(CH_3)_4Si$ was 0 ppm, and the chemical shifts of its substitute by $-N(CH_3)_2$ group were in the range from 5.90 to 6.90 ppm for $(CH_3)_3SiN(CH_3)_2$, from -1.30 to -1.85 ppm for $(CH_3)_2Si(N(CH_3)_2)_2$, from -16.30 to -17.50 ppm for $CH_3Si(N(CH_3)_2)_3$ and from -28.10 to -28.60 for $Si(N(CH_3)_2)_4$[19]. The chemical shift of ^{29}Si shifts towards a lower magnetic field, when one of the four carbon atoms around silicon atom was substituted by a nitrogen atom. When two of the four carbon atoms were substituted by two nitrogen atoms, it shifted again towards a higher magnetic field. Then, it further shifted higher as three and four carbon atoms were substituted by nitrogen. This behavior of ^{29}Si chemical shift, which is observed in the case of stepwise substitution of SiR_4 type compound by another more electronegative group, is known as the "sagging behavior"[19]. In addition, this "sagging be-

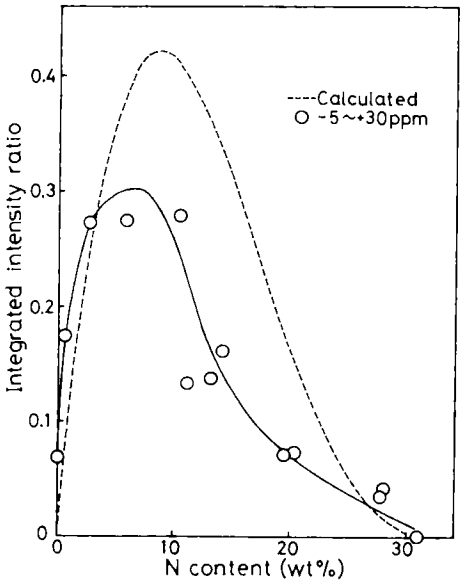

Fig. 7 The change of the integrated intensity ratio of the component between -5 and 30 ppm with nitrogen content of the powder. The dotted line shows the calculated atomic ratio of Si atom with SiC_3N configuration.

havior" was predicted by semi-empirical and empirical treatments considering the electronegativity of the substituent. Because nitrogen has higher electronegativity than carbon, if one of the four carbon atoms was substituted by nitrogen atom in β-SiC lattice, ^{29}Si chemical shift was considered to move towards a lower magnetic field compared to that of a pure β-SiC. Therefore, the low magnetic field component in Fig. 1 was considered to come from the silicon atoms surrounded by three carbons and one nitrogen (SiC_3

It was known that Si-C (H) units showed the chemical shift in this low magnetic region[20]. It was possible that amorphous Si-C(H) species contributed the tail of spectra in the low magnetic field. But this contribution of Si-C(H) species was probably small, because C-H and Si-H vibration could not be observed in the FT-PAS spectra of the powders, even though the direct chemical analysis of residual hydrogen was not carried out.

In order to see some compositional trend about the SiC_3N configuration, integrated intensity was calculated. It was difficult to estimate precisely the degree of the broadening by poor crystallinity and the effect of the different next nearest neighbor atoms on NMR chemical shift. For instance, nitrogen atoms were considered to bond three or four silicon atoms, as discussed later. The coordination number of nitrogen could affect on ^{29}Si chemical shift, even though that effect was probably low compared to the effect of nearest neighbor atoms. At the present stage, MAS-NMR can not distinguish between $SiC_{3/4}N_{1/3}$ and $SiC_{3/4}N_{1/4}$. Babonneau et al[18] quantitatively analyzed the MAS-NMR data of $SiC_{(4-x)}O_x$ (x = 0 to 4) by peak deconvolution. In this study, peak deconvolution was not performed. It was simply assumed that the low magnetic component with the chemical shift from -5 to 30 ppm came from Si atom with SiC_3N configuration, and measured the integrated intensity of that range. Peak deconvolution with some assumed different components may be suitable for discussions on subtle change of spectra, however compositional trend of spectra would be seen by this simple calculation.

Figure 7 shows the change of the integrated intensity ratio of the low magnetic field component with nitrogen content of the powders. The ratio of SiC_3N increased rapidly with nitrogen content of the powder and became maximum at around 8 wt% nitrogen content. Then, it decreased with the nitrogen content. The dotted line shows the change of the atomic ratio of Si atom having SiC_3N configuration with nitrogen content, calculated by assuming that C atom was randomly substituted by N atom in the β-SiC crystal and each N atom shared four Si atoms i.e. $SiC_{3/4}N_{1/4}$. If N atom shared three Si atoms i.e. $SiC_{3/4}N_{1/3}$, this dotted line showed the same tendency, but peak position shifted from 8.6 to 11.2 wt%. The integrated intensity ratio of low magnetic field component showed a similar behavior to the calculated
atomic ratio of Si with SiC_3N configuration. This fact probably suggested that a SiC_4 unit was changed to $SiC_{3/4}N_{1/4}$ or $SiC_{3/4}N_{1/3}$ by random substitution of C atom for N atom.

4-1-2. High N contennt composite powders

Carduner et al.[6] reported that the NMR spectra of a-Si_3N_4 showed two peaks (-46.8 and -48.9 ppm) and b-Si_3N_4 showed one peak (-48.7 ppm). Even though XRD pattern of the powder of Fig. 5(d) included both a- and β-Si_3N_4, the NMR spectrum exhibited only one peak at -48.3 ppm. The mean crystalline sizes of Fig. 5 (d) estimated by Scherrer's method were 35nm for α-Si_3N_4 and 44 nm for β-Si_3N_4.

In addition, the three peaks of α- and β-Si_3N_4 exist within 2.1 ppm. Therefore, in this experiment, the three NMR peaks could not be resolved because of the broadening by their poor crystallinity.

The chemical shift values of each Si configuration were considered to be in the following order, judging from the sagging behavior, $SiC_3N < SiC_4$, $SiC_2N_2 < SiCN_3 < SiN_4$. In the case of high nitrogen content of the powder, low magnetic field com-

ponent decreased and high magnetic field component increased with increasing nitrogen content. This fact suggested that C-rich configuration such as SiC_3N and SiC_2N_2 decreased and N-rich configuration such as $SiCN_3$ and SiN_4 increased with increasing nitrogen content.

In order to see some compositional trend about the Si configurations, integrated intensity was calculated as in the case of low N content particles. A calculation was done by simply assuming the chemical shift range for each silicon carbonitride unit as follows;

SiN_4 unit -42.5 to -57.5 ppm
SiC_3N unit -27.5 to -42.5 ppm
SiC_2N_2 unit -5 to -27.5 ppm
SiC unit -5 to -27.5 ppm (overlapped with SiC_2N_2)

Figure 8 shows the change of the integrated intensity ratio of these chemical shift ranges. Figure 9 shows the change of atomic ratio of Si atoms having various configurations, calculated by assuming that C atoms, tetrahedrally coordinated around Si atom, were randomly substituted by the introduced N atoms and each nitrogen shared four silicon atoms. If nitrogen atoms shared three silicon atoms, the calculated curves changed its value. For instance, SiN4 ratio became 1.0 at 33.3 wt% N content in the case of sharing four silicon, and at 39.9 wt% in the case of sharing three silicon. But the compositional trends were the same. The trends of each integrated intensity ratio in Fig. 8 were very similar to the corresponding curves in Fig. 9. These results suggested that nitrogen rich tetrahedral configuration of Si atom increased in a stepwise manner as the nitrogen content of the powder increased. At the present stage, ^{29}Si MAS-NMR can not distinguish between N atoms sharing three or four Si atoms. Further investigation would be needed for more precise interpretation of NMR spectra.

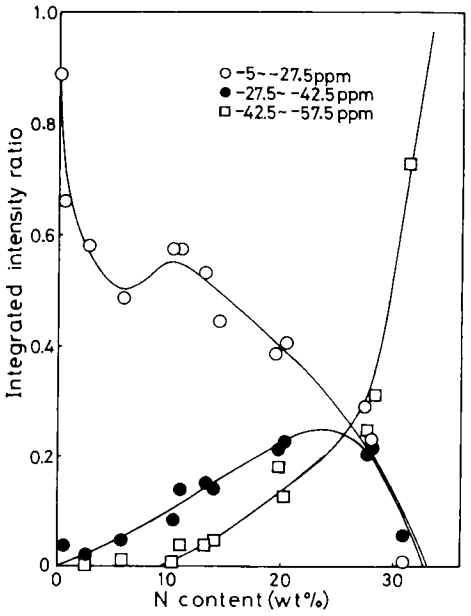

Fig. 8 The change of integrated intensity ratio of various components with nitrogen content of the powder.

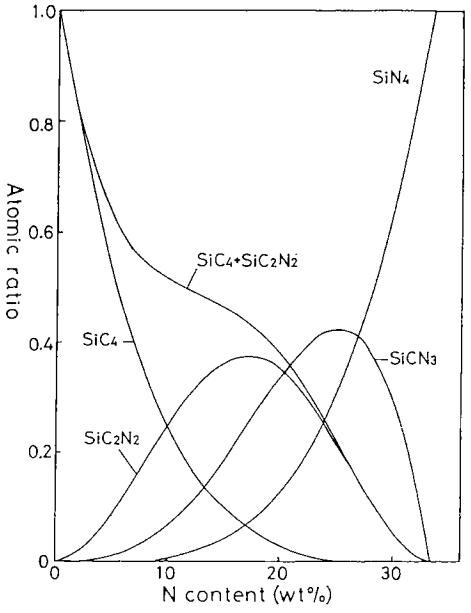

Fig. 9 The change of the calculated atomic ratio of Si atoms having various configurations with nitrogen content, assuming that C atoms, tetrahedrally coordinated around Si atom, were randomly substituted by N atoms.

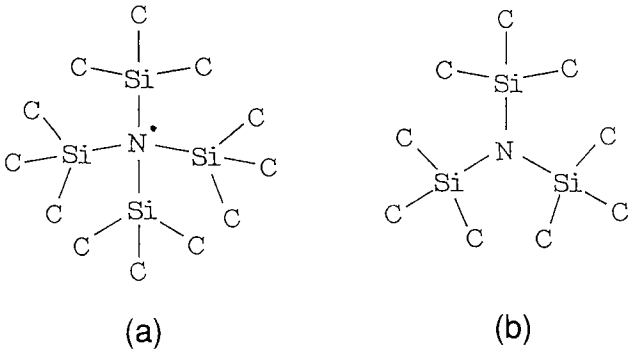

Fig. 10 The configuration of nitrogen atoms in the low nitrogen content SiC-Si_3N_4 composite particles.

4-2. ESR

The g value of ultrafine SiC was 2.0027, and changes in its values by introducing nitrogen were very small. The following were reported g values for several paramagnetic centers : g = 2.0055 for a Si dangling bond with only Si nearest neighbors,[21-23], g = 2.003 and ΔH_{pp} = 14 G for Si dangling bond with N nearest neighbors[22-24], g = 2.0027 and ΔH_{pp} = 6.1 G for C dangling bond[25,26], g = 2.0024 for nitrogen in diamond[27], g = 2.004 ±0.002 for nitrogen in 6H-SiC[28].
These g values were very close to each other except g = 2.0055 for Si dangling bond with only Si nearest neighbors. It was difficult to identify the paramagnetic defect centers only by g values.

When the nitrogen content exceeded 19.5 wt%, the ΔH_{pp} of ESR spectra became larger and the Ns increased with increasing nitrogen content and Si_3N_4 phase. Those paramagnetic defects seemed to be characteristic of Si_3N_4 phase. Warren et al.[29] reported that the ΔH_{pp} of Si dangling bond with N nearest neighbors was broadened by hyperfine interaction between ^{14}N and Si dangling bond. Therefore, the increase of the ΔH_{pp} suggested that the paramagnetic center with nitrogen neighbors, such as $Si(N)_3$, became dominant when nitrogen content exceeded 19.5 wt%.

4-3. Structure of composite particles

4-3-1. Low N content composite powder

In the previous study, transmission electron microscopic (TEM) observation showed that the low nitrogen content $SiC-Si_3N_4$ composite particles contained very small SiC crystals in a particle, and the lattice constant of crystalline SiC phase drastically decreased with nitrogen content. It was suggested that a composite particle consisted of small SiC crystals and grain boundary layer between crystals and that SiC microcrystals contained dissolved nitrogen by substituting C atoms[14]. The MAS-NMR results showed that the SiC_3N configuration was appeared by introducing nitrogen. However, at the present stage, ^{29}Si NMR can not distinguish between $SiC_{3/4}N_{1/4}$ and $SiC_{3/4}N_{1/3}$ units in these composite particles.

In β-SiC microcrystals containing dissolved nitrogen, nitrogen atoms were considered to be tetrahedrally surrounded by four Si atoms in the lattice ($SiC_{3/4}N_{1/4}$, Fig. 10(a)). In this case, nitrogen atoms in β-SiC lattice should be paramagnetic centers by unpaired electrons because of the valence difference of nitrogen and carbon. However, the results of spin concentration measured by ESR showed that most of the nitrogen atoms in the powder were present as a non paramagnetic form.

There could be two possible non paramagnetic nitrogen forms. One was a trivalent nitrogen bonded to three Si atoms ($SiC_{3/4}N_{1/3}$, Fig. 10(b)). The ultrafine SiC particles had a lot of paramagnetic defects. Even though those defects had not been identified, dangling bonds such as $C(Si)_3$ were considered to be present in ultrafine particles. If nitrogen atoms substituted the carbon dangling bond, nitrogen could exist as a non paramagnetic trivalent form ($N(Si)_3$). This might be the reason that spin density tended to decrease with increasing nitrogen content in the case of low nitrogen content of $SiC-Si_3N_4$.

The composite particles showed only a broad SiC pattern, until nitrogen content became up to about 10 wt%. However, trivalent nitrogens were unlikely to be present in the β-SiC crystalline lattice at large amounts up to about 10 wt%, because they distort the tetrahedral SiC lattice much. Trivalent nitrogen atoms might exist in grain boundary layer.

Another possible non paramagnetic form was positively charged nitrogen atom bonded four Si atoms ($\oplus N(Si)_4$) making pairs of negatively charged defects such as $\ominus Si(C)_3$ or $\ominus C(Si)_3$. In this case, nitrogen atoms could exist in β-SiC lattice, because nitrogens bonded to four silicons were expected to distort the β-SiC lattice less than trivalent nitrogens. Nitrogen might reduce the paramagnetic defect in the SiC phase, because Ns tended to decrease with increasing nitrogen content until nitrogen content reached to 19.5 wt%. However, further investigations will be

needed to clarify the defect structures.

At the present stage, it seemed most likely that nitrogen atoms in the powder partly dissolved into β-SiC crystal as tetrahedral form bonded to four Si atoms, and were partly present in the grain boundary layer as trivalent forms bonded to three Si atoms.

4-3-2. High N content composite powder

In the case of high nitrogen content SiC-Si_3N_4 composite particles, XRD results showed that SiC, Si_3N_4, Si and amorphous phases were present in the powder and their relative amount changed according to the nitrogen content of the powder. The previous study[14] showed that the lattice constants of Si_3N_4 phase in composite particles were different from those of pure Si_3N_4.

The NMR results showed that these particles consisted of SiC, Si_3N_4, amorphous phases, and contained the configuration of $SiC_{(4-x)}/4N_{x/4}$ or $SiC_{(4-x)}/4N_{x/3}$ with x = 0 to 4. The proportion of N-rich Si configurations such as SiN_4 and $SiCN_3$ increased stepwise with increasing nitrogen content of the powder. As the N-rich configuration increased, the crystalline phase changed from SiC to Si_3N_4 or an amorphous phase. Finally, the powder with nitrogen content of 30.9 wt% was composed of crystalline Si_3N_4 and Si. SiC phase was not completely pure phase, and contained nitrogen. Si_3N_4 phase showed a different lattice constant, but direct evidence was not found of the presence of C in crystalline Si_3N_4 phase by MAS-NMR.

The local structure of SiC-Si_3N_4 composite particles was studied by MAS-NMR and ESR. The low N content particles consisted of very small crystalline SiC containing nitrogen. The SiC_3N configuration was appeared by introducing nitrogen. It was suggested that nitrogen atoms in the low nitrogen content composite particles were partly present in β-SiC microcrystal tetrahedrally surrounded by four Si atoms and partly present in the grain boundary layer between SiC microcrystals in the particles as trivalent state bonded to three Si atoms.

In the case of high nitrogen content powder, N-rich Si configurations increased with increasing nitrogen content of the powder, and the crystalline phase changed from SiC to Si_3N_4 or amorphous phases.

5. Conclusions

Acknowledgement

We would like to thank the coal liquefaction research group in our laboratory for faciliting the use of NMR and ESR equipments.

References

1) E. Oldfield and R. J. Kirkpatrick, "High-Resolution Nuclear Magnetic Resonance of Inorganic Solids.", Science (Washington. D.C.), 227, 1537-44 (1985)
2) G. R. Hatfield and K. R. Carduner, "Review, Solid State NMR: Applications in High Performance Ceramics.", J. Mater. Sci., 24, 4209-19 (1989)
3) G. L. Turner, R. J. Kirkpatrick, S. H. Risbud, and E. Oldfield, "Multinuclear Magic-Angle Sample-Spinning Nuclear Magnetic Resonance Spectroscopic Studies of Crystalline and Amorphous Ceramic Materials.", Am. Ceram. Soc. Bull., 66[4], 656-63 (1987)
4) D. C. Apperley, R. K. Harris, G. L. Marshall, and D. P. Thompson, "Nuclear Magnetic Resonance Studies of Silicon Carbide Polytypes." J. Am. Ceram. Soc., 74[4], 777-82 (1991)
5) K. R. Carduner, R. O. CarterⅢ, M. E. Milberg, and G. M. Crosbie, "Deter mination of Phase Composition of Silicon Nitride Powders by Silicon-29 Magic Angle Spinning Nuclear Magnetic Resonance Spectroscopy.", Anal. Chem., 59, 2794-97 (1987)
6) K. R. Carduner, C. S. Blackwell, W. B. Hammond, F. Reidinger, and G. R. Hatfield," ^{29}Si NMR Characterization of α-and β-Silicon Nitride.", J. Am. Chem. Soc., 112, 4676-79 (1990)
7) N. R. Dando and M. A. Tadayyoni, "Characterization of Polyphasic Silicon Carbide Using Surface-Enhanced Raman and Nuclear Magnetic Resonance

Spectroscopy.", J. Am. Ceram. Soc., 73[8], 2242-46 (1990)
8) G. R. Finlay, J.S.Hartman, M. F. Richardson, and B. L. Williams, "^{29}Si and ^{13}C Magic Angle Spinning N.M.R. Spectra of Silicon Carbide Polymorphs.", J. Chem. Soc., Chem. Commun., 1985, 159-61 (1985)
9) J. R. Guth and W.T.Petuskey, "Silicon-29 Magic Angle Sample Spinning Nuclear Magnetic Resonance Characterization of SiC Polytypes.", J. Phys. Chem., 91, 5361-64 (1987)
10) J. S. Hartman, M. F. Richardson, B. L. Sherriff and B. G. Winsborrow, "Magic Angle Spinning NMR Studies of Silicon Carbide: Polytypes, Impurities, and Highly Inefficient Spin-Lattice Relaxation.", J. Am. Chem. Soc., 109, 6059-67 (1987)
11) K. R. Carduner, S. S. Shinozaki, M. J. Rokosz, C. R. Peters, and T. J. Whalen, "Characterization of β-Silicon Carbide by Silicon-29 Solid-State NMR, Transmission Electron Microscopy, and Powder X-ray Diffraction." J. Am. Ceram. Soc., 73[8] 2281-86 (1990)
12) G. W. Wagner, B. K. Na, and M. A. Vannice, "High-Resolution Solid-State NMR of ^{29}Si and ^{13}C in β-Silicon Carbides.", J. Phys. Chem., 93, 5061-64 (1989)
13) D. J. O'Donnell, T. T. P. Cheung, G. F. Schuette and M. Sardashti, "Solid-Sample ^{11}B Nuclear Magnetic Resonance and X-ray Photoelectron Spectroscopy Study of Boron-Doped β-Silicon Carbide.", J. Am. Ceram. Soc., 74[8], 2025-28 (1991)
14) M. Suzuki, Y. Maniette, Y. Nakata and T. Okutani, "Synthesis of Silicon Carbide-Silicon Nitride Composite Ultrafine Particles Using a CO_2 Laser"., J. Am. Ceram. Soc., 76 [5], 1195-200 (1993)
15) M. Suzuki, Y. Nakata, T. Okutani and A. Kato,"Preparation of SiC Ultrafine Particles by Using a CO_2 Laser"., Seramikkusu Ronbunshi, 97, 972-75 (1989)
16) G. C. Levy and I. R. Peat, "The Exp erimental Approach to Accurate Carbon-13 Spin-Lattice Relaxation Measurements", J. Magn. Resonance 18, 500-21 (1975)
17) K. E. Inkrott, S.M. Wharry, and D. J. O' Donnell, "Silicon -29 Solids NMR-MAS Characterization of Non-Oxide powders and Fibers.", Mater. Res. Soc. Symp. Proc., 73, 165-71 (1986)
18) F. Babonneau, G. D. Soraru and J. D. Mackenzie, "^{29}Si MAS-NMR Investigation of the Conversion Process of a Polytitanocarbosilane into SiC-TiC Ceramics", J. Mater. Sci., 25, 3664-70 (1990)
19) H. Marsmann, "^{29}Si-NMR Spectroscopic Results"; pp65-235 in NMR Basic Principles and Progress Vol.17, Oxygen-17 and Silicon-29, Edited by P. Diehl, E. Fluck and R. Kosfeld.Springer-Verlag, Berlin, 1981
20) G. D. Soraru, F. Babonneau and J. D. Mackenzie,"Structural Concepts on New Amorphous Covalent Solids" J. Non-Cryst. Solids, 106, 256-61 (1988)
21) S. Hasegawa, N. Furuta, T. Takeshita, T. Inokuma, and Y. Kurata, "Phosphorous and Nitrogen Doping into Polycrystalline SiC Films Prepared by Plasma-Enhanced Chemical Vapor Deposition at 700℃.", J. Appl. Phys., 72 [4], 1374-77 (1992)
22) A. Morimoto, Y. Tsujimura, M. Kumeda and T. Shimizu, "Properties of Hydrogenated Amorphous Si-N Prepared by Various Methods.", Jpn. J. Appl. Phys, 24[11], 1394-98 (1985)
23) W. L. Warren, F. C. Rong, E. H. Poindexter, J. Kanicki, and G. J. Gerardi, "Low-Temperature Electron Spin Resonance Investigation of Silicon Paramagnetic Defects in Silicon Nitride.", Appl. Phys. Lett., 58[21], 2417-19 (1991)
24) D. T. Krick, P. M. Lenahan, and J. Kanicki, "Electrically Active Point Defects in Amorphous Silicon Nitride: An Illumination and Charge Injection Study.", J. Appl. Phys., 64[7], 3558-63 (1988)
25) A. Morimoto, T. Miura, M. Kumeda, and T. Shimizu, "Glow Discharge a-$Si_{1-x}C_x$:H Films Studied by ESR and IR Measurements.", Jpn. J. Appl. Phys.,

21〔2〕, L119-L121 (1982)
26) I. Watanabe and K. Sugata, "ESR in Diamond Thin Films Synthesized by Microwave Plasma Chemical Vapor Deposition.", Jpn. J. Appl. Phys., 27〔10〕, 1808-11 (1988)
27) W. V. Smith, P. P. Sorokin, I. L. Gelles and G. J. Lasher, "Electron-Spin Resonance of Nitrogen Donors in Diamond.", Phys. Rev., 115〔6〕, 1546-52 (1959)
28) L. S. Dang, K. M. Lee, G. D. Watkins and W. J. Choyke, "Optical Detection of Magnetic Resonance for an Effective-Mass-like Accepter in 6H-SiC.", Phys. Rev. Lett., 45〔5〕, 390-94 (1980)
29) W. L. Warren, F. C. Rong, E. H. Poindexter, G. J. Gerardi, and J. Kanicki, "Structural Identification of the Silicon and Nitrogen Dangling-Bond Centers in Amorphous Silicon Nitride.", J. Appl. Phys., 70〔1〕, 346-54 (1991)

ホットプレス法によるAlセラミックス系複合強化材の作成*1

（キーワード：Al-セラミックス系複合強化材、ホットプレス法、三点曲げ試験、硬さ試験）

植田　芳信*2　鈴木　良和*3　下川　勝義*2　村上　和幸*4

1　緒　言

耐熱性、耐摩耗性材料としてAlセラミックス系複合材料の開発[1,2]が数多く行われているが、実用に向けては信頼性を求めて、さらに詳細な検討が必要である。

今回はAl粉末をマトリックスとしてSiC,Si_3N_4各粉末、並びに各ウィスカーを分散させた複合強化材をホットプレス（H．P）法で比較的低温（973K）で作製した。さらに高温（～1523K）での熱処理を行い、X線回折やXMAによる分析と三点曲げ強度、ビッカース硬度測定等から熱的変化とその影響について検討したのでその結果を報告する。

2　実験方法

マトリックスにはAl合金粉末（2024）平均粒径20μm）を、分散材にはSiC,Si_3N_4の粉末（P:いずれも平均粒径1.4μm）およびウィスカー（W:SiCは粒径0.3～0.7μm、長さ10μm以上、Si_3N_4は粒径0.3～1.2μm、長さ10μm以上）を用いた。

分散材の体積率が10，15，20vol%になるように秤量後、スウィングロールミルを用いて乾式で混合した。ウィスカーを分散させた混合試料のSEM像をFig.1に示す。SiCはSi_3N_4に比べて長く、一部凝集を起こしているのが認められた。

得られた混合原料をホットプレス装置を用いて3.5×3.5 mmの成形体を作製した。10^{-3}Paで真空脱ガス後、Arガス0.2MPaの雰囲気中、973Kで300s保持した。97.3Kでプレス操作（31.2MPa）を行い室温まで保持した。

成形体試料を3×4 mmの三点曲げ用試験片に切断した後、表面を研磨し三点曲げ試験、ビッカース硬度測定を行った。残りの試験片について赤外線イメージ炉を用い、N_2ガス雰囲気で予備加熱（1323K）を行った。亀裂などの発生を防ぐために昇温速度を4.8K/sで行った。この予備加熱した試料を赤外線放射炉で1423Kで熱処理を行った。一部の試料については熱処理を微小重力（μg）下でも行った。赤外線放射炉は、微小重力を得るための落下実験用に試作した装置[3]であり、1523Kまで90～120sで急速昇温ができる。微小重力下での実験は北海道上砂川町の地下無重力実験センターの落下施設を用いて行った。この試料についても三点曲げ試験、ビッカース硬度の測定を行った。さらに、これらの試料についてX線回析で化合物の同定を、SEMおよびEPMAで破面および組織の観察と分析を行った。

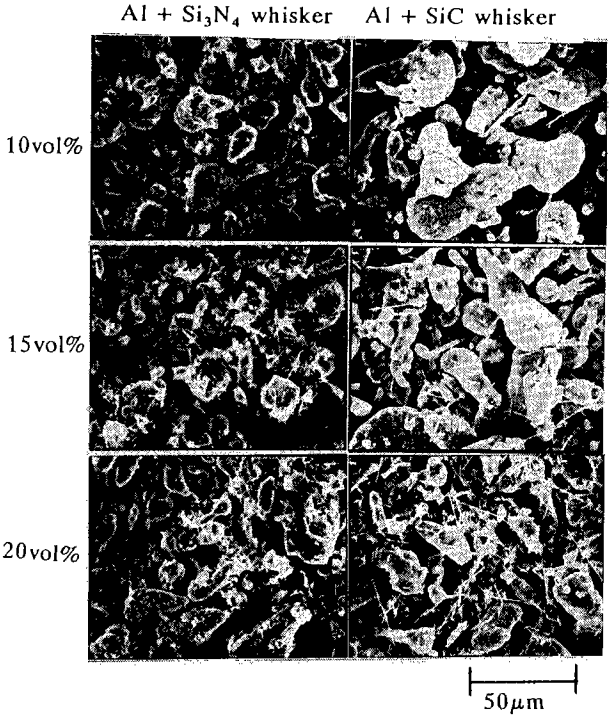

Fig. 1　SEM image of Al composite samples mixed with Si_3N_4 and SiC whisker.

＊1　粉体及び粉末冶金、Vol.42、No. 3（1995）pp.318～322より転載（粉体粉末冶金協会より転載許可）
＊2　極限環境材料部
＊3　首席研究官
＊4　北海道工業大学

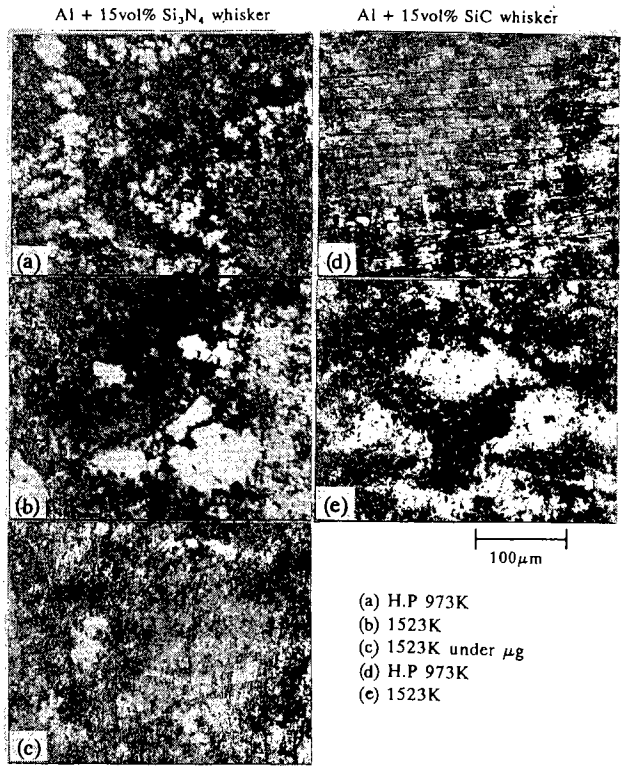

Fig. 2 Optical micrographs of surface of composites (Al/Si_3N_4 and Al/SiC).

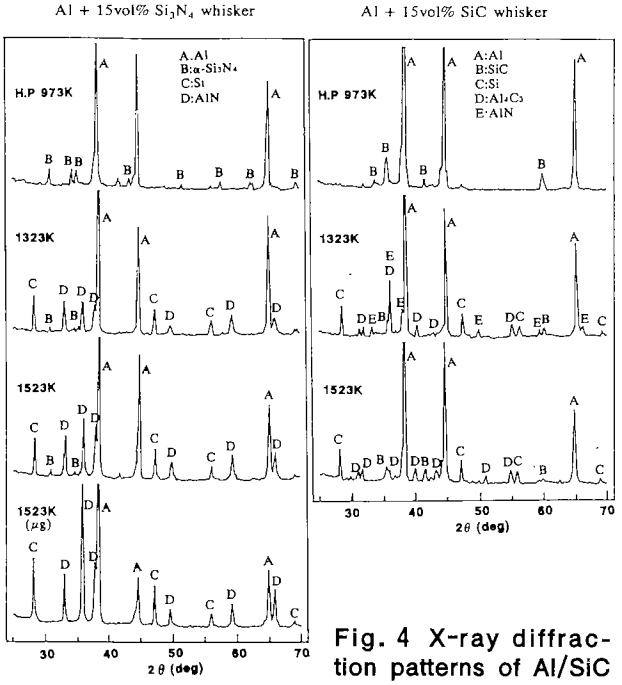

Fig. 3 X-ray diffraction patterns of Al/Si_3N_4 composites.

Fig. 4 X-ray diffraction patterns of Al/SiC composites.

3 結果および考察

Al粉末にSi_3N_4およびSiCのウィスカーを15vol%分散させたホットプレス試料および1523Kでの熱処理試料の表面を光学顕微鏡で観察した結果をFig. 2に示した。ホットプレス試料（a）（b）は白っぽいところにAlが、黒っぽいところにセラミックスが多く分散しており、比較的気孔の少ない細かく平坦な組織を示している。熱処理試料（b）（c）ではSi_3N_4やSiC,がAlと反応あるいは分解して生成したAlN およびAl_4C_3と思われる大きな組織が、また、このときに発生したと思われる亀裂や気孔が多く観察された。微小重力下の場合（c）は、（b）に比べて生成物も細かく比較的均一な組織を示している。

Fig. 3とFig. 4にウィスカーを混合した試料のX線回析結果を示した。Si_3N_4の場合、ホットプレス試料ではAlとSi_3N_4のみで分解や反応が認められないが、1323Kの熱処理試料ではSiとAlNの生成が始まり、1523K試料ではSiとAlNが多く、Si_3N_4のピークが小さくなっている。1093Kと1213Kについても調べたが、Siの生成がわずかに認められ、ホットプレスのみの試料と大きな差はなかった。SiCの場合のホットプレス試料にAlとSiCが、1323Kの熱処理試料では、Si、

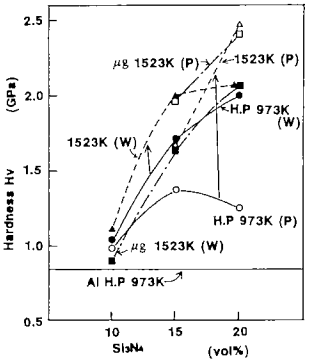

Fig. 5 Vickers hardness of Al/Si_3N_4 composites.

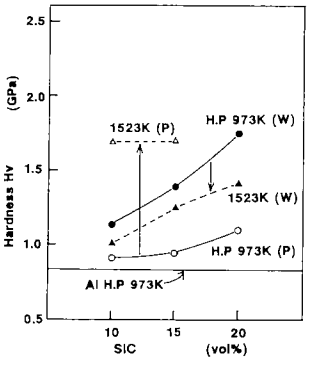

Fig. 6 Vickers hardness of Al/SiC composites.

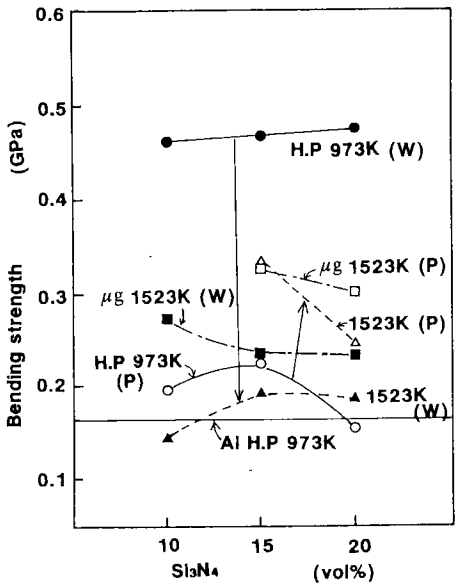

Fig. 7 Bending hardness of Al/Si_3N_4 composites.

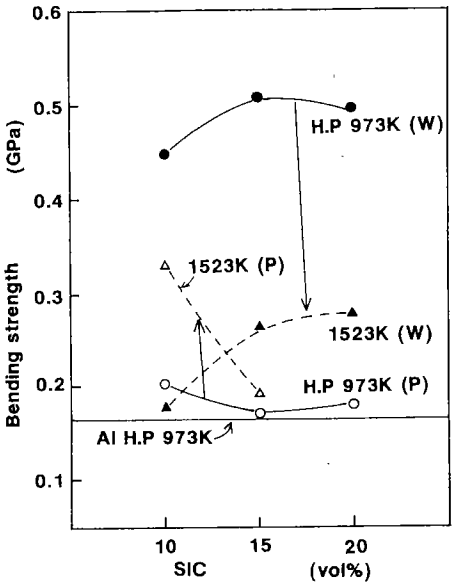

Fig. 8 Bending hardness of Al/SiC composites.

Al_4C_3が認められた。1093Kと1213Kについても調べたが、Si、Al_4C_3の生成が認められた。このことからSi_3N_4に比べてSiCのほうが分解または反応の始まる温度が低いことが分かった。SiCの1323KでAINが生成したが、これは予備加熱をN_2ガス雰囲気中で行ったためと思われる。粉末を分解した場合および分散材の体積率が変わっても、生成物の傾向は変わらなかった。

つぎに、ホットプレス試料および熱処理試料について機械的強度を調べるために、ビッカース硬度測定および三点曲げ強度試験を行った。

Fig. 5 とFig. 6 にビッカース硬度測定結果を示し

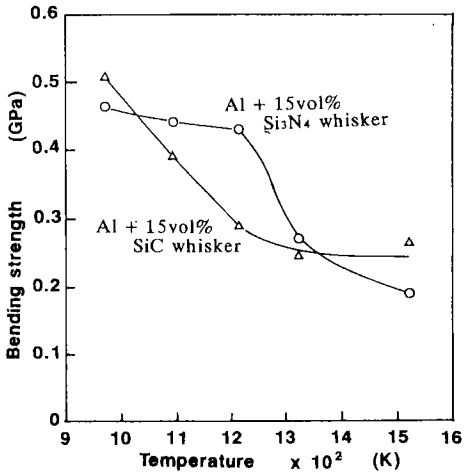

Fig. 9 Relation between heat treatment and bending strength.

た。ホットプレス試料ではSi_3N_4およびSiCのいずれの場合も、Al粉末のみをホットプレスした試料と比較して、分散材の体積率が多くなるにしたがって硬さを増す傾向を示しており、分散材の効果が現れていると思われる。さらに熱処理した試料では、Si_3N_4を加えた微小重力下のものとSiCのウィスカーを加えた場合を除いてはいずれも、ホットプレスのみの試料と比較して向上した。Fig. 2 に示したように熱処理試料では亀裂や気孔が多いにもかかわらず硬さが増すのは、X線回析の結果から分かるように微少部分に生成したAIN、Al_4C_3が硬さを増し、全体的にビッカース硬度を向上させるためと考えられる。

三点曲げ強度測定結果をFig. 7 とFig. 8 に示した。Si_3N_4およびSiCを分散したいずれの場合も、Al粉末のみをホットプレスした試料と比較すると、ウィスカーの場合は高い強度を示したが、粉末の場合はあまり強度が向上していない。1523Kで熱処理後の試料はウィスカーの場合は著しく低下したが、粉末の場合はウィスカーの場合と異なり、強度の低下はなく逆に向上した。Si_3N_4の場合微小重力下で熱処理を行った試料が、重力下のものに比較していずれも強度が向上した。しかし、ビッカース硬度のようにセラミックスの体積率と強度の関係は顕著でなかった。

つぎに、ウィスカーを分散した場合の熱処理による曲げ強度の低下が著しいので、熱処理温度による影響を調べた。

熱処理温度と曲げ強度の関係についてFig. 9 に示した。Si_3N_4の場合は、1213Kまでは強度の低下は少ないが、その後急激に低下した。SiCの場合は、1093Kから急激に低下しており、1213Kで一定値を示した。また、曲げ強度の低下はFig. 3 とFig. 4 に示したSi、AIN、Al_4C_3の生成量と比例していた。

Fig.10にウィスカーを分散した試料の三点曲げ試験後の破面のSEM組織を示した。ホットプレス試料の場

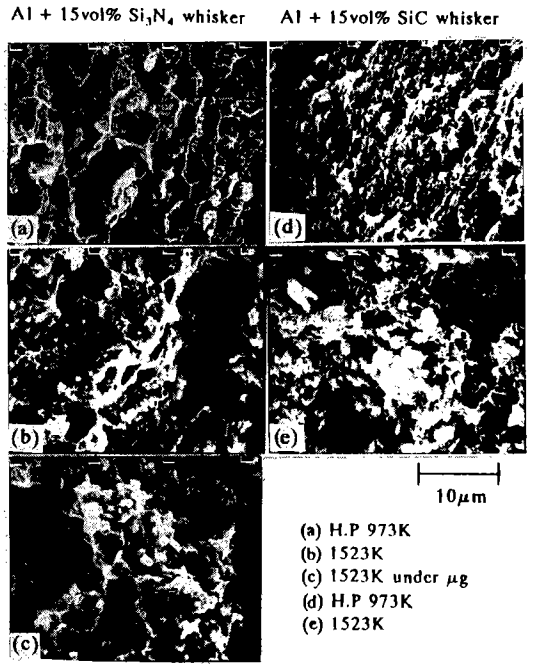

Fig.10 Fracture surface of Al/Si_3N_4 and Al/SiC composites after bending test.

合は脈状模様から見られ粒内破壊が考えられる。1523K熱処理試料では、Si_3N_4やSiCがAlと反応または分解してSi、AIN、Al_4C_3が生成するときに発生したと思われる亀裂や気孔が多く観察され、ここが破壊の発生場所になって曲げ強度を低下させたものと考えられる。

Fig.11とFig.12にSi_3N_4粉末を15vol%分散したホットプレスのみの試料、およびその熱処理後の試料の曲げ試験後の破面の観察とEPMAでの分析結果をそれぞれ示した。SEM像およびSikαの面分析から、ホットプレス試料では脈状模様の破面に沿ってSiが分布していることから粒内破壊がおこったと考えられる。熱処理試料では破面の形状が大きくなっているが、破面は脈状模様を示しており、ホットプレス試料と同様に粒内破壊がおこっていると考えられる。また、ウィスカー分散試料の場合と異なり、亀裂や気孔の発生が少ないことから、曲げ強度を向上させたものと考えられる。

4 まとめ

ウィスカーを分散してホットプレスで作製した試料は、Al粉末のみをホットプレスした試料と比較して高強度の試料が得られ、複合化による効果が顕著であった。ホットプレス試料を熱処理することによってSi_3N_4やSiCがAlと反応または分解してSi、AIN、Al_4C_3が生成するときに気孔または亀裂が発生するため、曲げ強度は著しく低下したが、微小部分では生成したAINやAl_4C_3が硬さを増し、全体的にビッカース硬度を向上する傾向が認められた。

粉末で分散した場合は、熱処理時に気孔や亀裂の発生が少ないため、硬くなった結果ウィスカーを分散した場合の様な曲げ強度の低下はなく、逆に強化された。

微小重力下では、Si_3N_4粉末を分散した場合には、体積率が増しても硬度の増加を伴い曲げ強さ向上が認められ、分散性への効果が見られるが、ウィスカーの場合は、熱処理における亀裂や気孔の発生による影響が大きいため、期待したほどの効果は見られなかった。なお、微小重力の効果についてはまだ実験回数が少ないので、今後さらに検討する必要がある。

文 献

1）大蔵明光：日本金属学会会報、29（1990）、91.
2）日本産業技術振興協会 新複合材研究推進協議会：新複合材料の先端的技術開発の現状と将来機械的機能材料（無機系・金属系）分野、(1988)、79.
3）下川勝義、鈴木良和、植田芳信他：北海道マイクログラビティー研究会第3回講演論文集（1944）

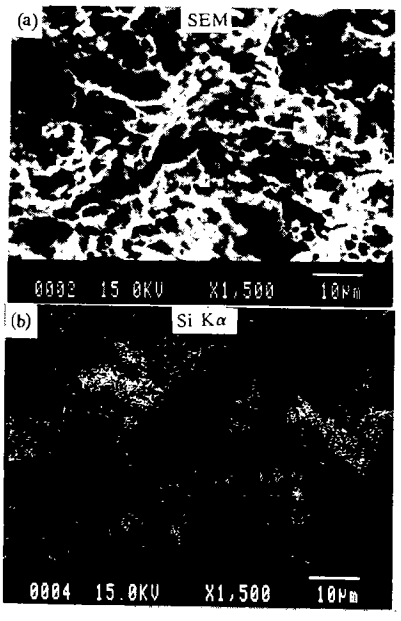

Fig.11 Fracture surface of hot pressed sample after bending test (Al+15vol% Si_3N_4 powder).

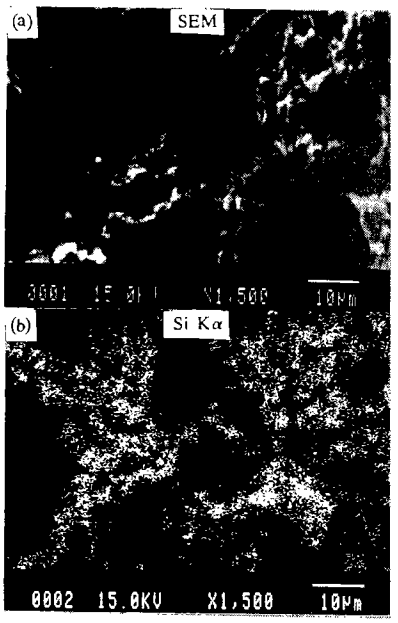

Fig.12 Fracture surface of additional heat treatment sample after bending test (Al +15vol% Si_3N_4 powder).

Separation and Purification of Lactic Acid : Fundamental Studies on the Reverse Osmosis Down-stream Process*1

(Keywords: Polyamide composite membrane, Lactate; Lactic acid, pH, Ion dissociation, Reverse osmosis)

M.K.H. Liew*2, Shigenobu TANAKA*3, Mikio MORITA*3

1. Introduction

Lacti acid can be obtained via a chemical or a fermentation process. Although the chemical process offers a product with a relatively low production cost, an optically inactive racemic mixture of 50% L-type and 50% D-type lactic acid is always produced. Conversely, by fermentation, the selectivity of lactic acid can be attained by using an appropriate bacteria species and/or by genetic engineering of the species. In this project L-lactic acid is preferred as it can produce biodegradable plastic material, material with high dielectric constants for liquid crystals, and optical isomeric reagents. This is produced via fermentation process using potato starch as raw material, which is a common agricultural product in Hokkaido, Japan.

In order to maximize the production of lactic acid in a fermentation process, special caution has to be taken in the choice of the pH-controlling agent adopted. This is because certain pH-controlling agents were found to have inhibitory effects on cell growth due to their salts produced [1] and/or fouling effects on microfiltration and ultrafiltration processes [2-4]. Hongo and co-workers [1] studied the effects of lactic acid and various lactates on the cell growth using *L. delbrueckii*, in which sodium lactate, ammonium lactate and calcium lactate (1.0% each) were found to offer only 50%, 67% and 72% of cell growth, respectively. Although calcium lactate had the least detrimental effect on cell growth, its low solubility could lead to solidification within the broth, resulting in severe fouling during membrane separation process. This option was therefore not considered in this study. Alternatively, sodium hydroxide or ammonium hydroxide could be used to control pH without causing a significant detrimental effect on cell growth, on condition that a microfilter is used to continually release the lactates produced [5,6].

The adverse effects of these lactates on the performance of the RO down-stream process have, however, yet to be evaluated. This forms the objective of the present study. In particular, the physico-chemical and operating effects of lactic acid and lactates will be studied, and any solute membrane interaction that exits, characterized. The results obtained from this study might facilitate the selection of the best pH controlling agents to be used in the lactic acid production process. To substantiate the physico-chemical effects being species-originated, the effective pH range of this polyamide composite membrane will also be considered.

2. Materials and Methods

Three broth-free feed solutions of sodium lactate, ammonium lactate and lactic acid (Wako Pure Chem. Ind. Ltd.) were concentrated using a flatsheet polyamide composite membrane (Nitto Denko Co., NTR7199) which was placed in a stirred-cell with working volume of 300 ml. The

---

* 1 This paper was reproduced from Desalination, Vol. 101,(1995) pp.269-277 by the permission of Elsevir Science-NL, The Netherlands.

* 2 STA Fellow

* 3 Booscience and Chemistry Division

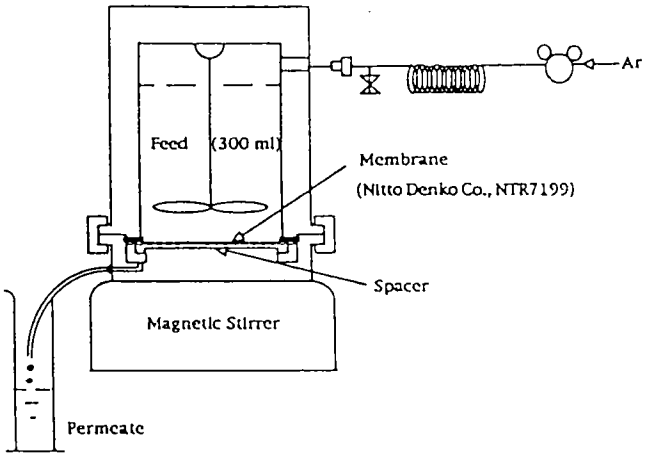

Fig.1 Schematic diagram of the apparatus used to concentrate broth-free solutions.

stirred-cell was placed on a magnetic stirrer (Iwaki Glass Co., BS-190), and inert gas was used to regulate the pressure applied; a schematic diagram of the experimental set-up is depicted in Fig. 1.

Flux was measured volumetrically; permeate concentration was detected using a standard HPLC method (Tosoh Co., Co-8020); pH value was recorded using a pH meter (Horiba Co., M.8L); and osmotic pressure was measured by the RO membrane permeating method [7]. In addition, the bulk concentration (C_b), total solute loss (Tsl), rate of solute loss (Rsl), solute rejection (R_{obs}) and concentration efficiency (η) were obtained from the equations listed below (it was assumed that densities were identical to that of water).

$$C_b = \frac{(C_f \rho_f V_i) - (C_p \rho_p V_p)}{[\rho_b (V_i - V_p)]} \times 100 \quad (1)$$

$$Tsl = \frac{(C_p \rho_p V_p)}{(C_f \rho_f V_i)} \times 100 \quad (2)$$

$$Rsl_t = \frac{\triangle Tsl}{\triangle t} = \text{gradient of graph } Tsl \text{ vs } t \quad (3)$$

$$Rsl_t = \frac{\triangle Tsl}{\triangle Vp} = \text{gradiennt of graph } Tsl \text{ vs } V_p \quad (4)$$

$$R_{obs} = \left[1 - \frac{C_p}{C_b}\right] \times 100 \quad (5)$$

$$\eta = \frac{\triangle C_b}{C_f} = \frac{C_b - C_f}{C_f} \quad (6)$$

where C, ρ, V and t denote concentration, density, volume and time, respectively; and the subscripts b, f, i and p refer correspondingly to bulk solution, feed, initial and permeate.

3. Results and Discussions

3. 1 Effective pH Range

Fig. 2 shows the pH effect on the polyamide membrane as investigated using hydrochloric acid or sodium hydroxide solutions. When the pH of the solution was increased from 4.2 to 10.1, the membrane flux decreased gradually from 0.69 to 0.50 $m^3.m^{-2}.d^{-1}$ (27.5%), while the pH of permeate increased from 6.1 to 7.8 (27.9%) in the vicinity of neutral pHs. These new neutral pHs of permeate obtained, as expected, were most likely due to the surface forces and the electrical potential jumps on the membrane boundaries, caused by the difference in distribution coefficients for H^+ and OH^-, as have been discussed in details by Starov and Churaev [8]. However at pH 2.2 a dramatic increase in flux to 1.85 $m^3.m^{-2}.d^{-1}$ (an increased of ≧170%) with extensive solute leakage was observed; equal values of pH were attained for both permeate and feed. This suggests that this particular type of membrane swelled in the low pH range, around pH 2.2, as a result of the variations in membrane charge brought about by pH changes. This result is in agreement with Hurndall's work [9].

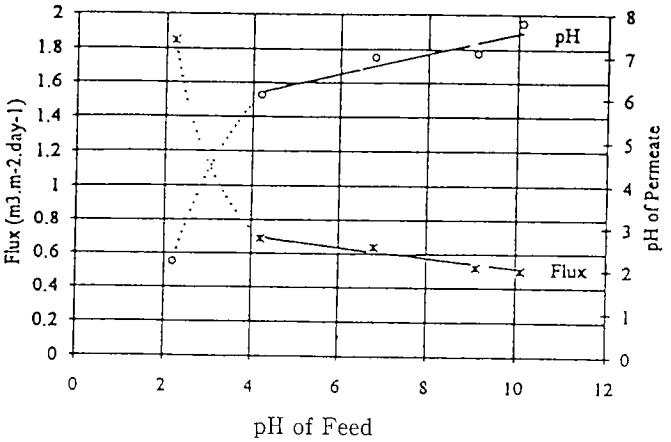

Fig. 2 Effects of pH on polyamide composite membrane

3. 2 Physico-chemical Effects

The membrane performances of three different feed solutions (3.0%), concentrated at 7 MPa and 900 rpm were compared. The results showed a decreasing order of flux for lactic acid, ammonium lactate and sodium lactate. For instance, at a permeate volume of 250 ml, lactic acid had a flux of 0.66 $m^3.m^{-2}.d^{-1}$; ammonium lactate, 0.30$m^3.m^{-2}.d^{-1}$; and sodium lactate, 0.18$m^3.m^{-2}.d^{-1}$. Conversely, an increasing order of solute reduction factor (C_b/C_p) for the above feeds was found, as illustrated in Fig. 3. The solute reduction factors for 3.0% feeds of lactic acid, ammonium lactate and sodium lactate at 250 ml were 5.8 (equivalent to a rejection of 83%), 18.3 (rejection of 91%) and > 80.0 (rejection of > 99%), respectively. The values attained were the result of different degrees of solute leakage as indicated in Fig. 4, where the permeate concentration for the above feeds were 1.8%, 0.82% and 0.14% at 250 ml. This illustrates the well-known trade-off between solute rejection and permeate flow rate in RO systems [10].

The differences in flux and solute reduction factor for these three different feeds were found to be a function of their pH values; the pH values for lactic acid, ammonium lactate and sodium lactate were found to be 2.2, 5.4 and 7.2, respectively. To further confirm the pH effects of feeds on the flux and solute retention, further experiments with 3.0% lactic acid

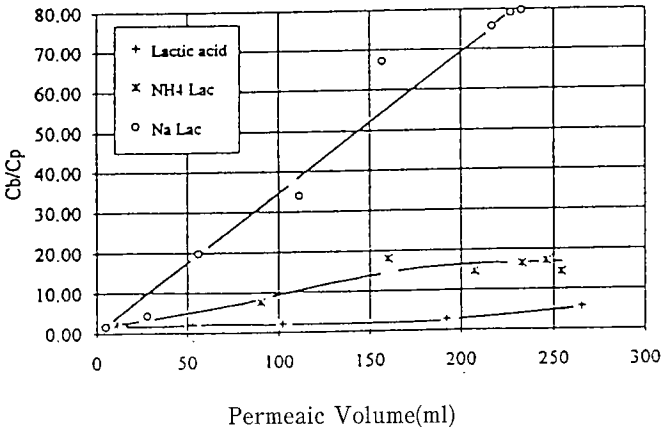

Fig. 3 Comparison of solute reduction factors for three different feed solutions at 3.0%

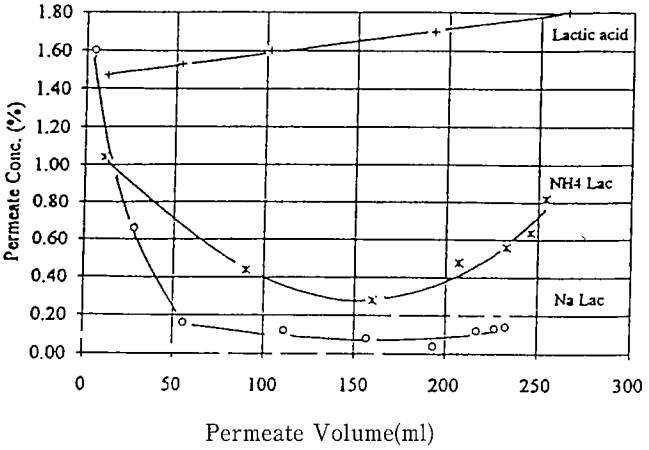

Fig. 4 Permeate concentration profile for different feeds

adjusted to pH 5.6 and sodium lactate adjusted to pH 11.5 using NaOH(s), were also conducted. All these results are summarized in Figs. 5 and 6, showing that with an increase in pH, flux and permeate concentration were decreased, while the solute reduction factor was increased.

The chemical compositions for these feeds at different pH values were calculated and confirmed with the assistance of equilibrium diagrams [11,12], as shown in Table 1. The data indicate that at pH 2.2 there were only 0.01 Mions, yet 0.33 M lactic acid molecules were present; whereas at pHs ranging from 5.4-11.5 concentration of ions remained relatively constant at 0.54 M, with an insignificant concentration of molecules. Fig. 6 further depicts that at pHs where a low concentration of ions was present, the permeate concentration or solute leakage was enhanced; this was the case for pH 2.2. At pHs where a high concentration of ions existed (i.e., pH 5.4-11.5), the permeate concentration or solute leakage was reduced accordingly. This suggests that solutes in ionic state are preferentially retained as compared with their counterpart (i.e. molecules). This was likely to be attributed to the larger sizes of ions attained as a result of the potential hydration they inherit by merit of their charge densities [13,14]. The larger sizes of hydrated ions, compared with the molecules, would reduce their rates of diffusion, re-

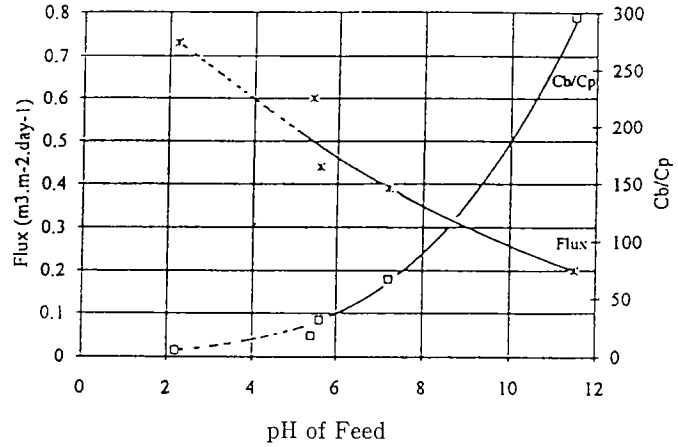

Fig. 5 Effects of pH values on flux and solute reduction factor

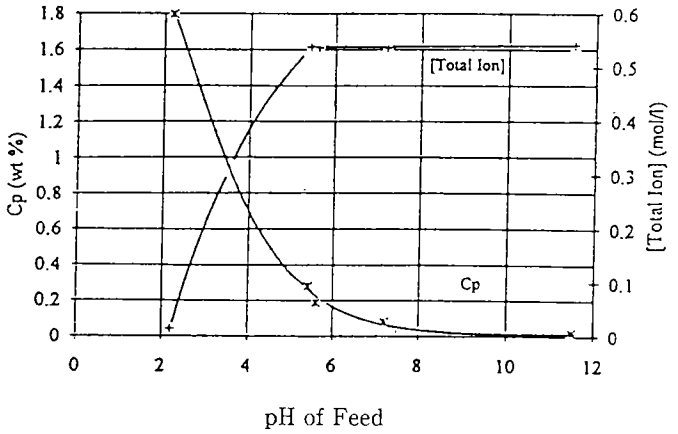

Fig. 6 Relationships between pH of feed, permeate concentration and total ion concentration

sulting in lower permeate concentrations. The increase in osmotic pressure due to the enhanced dissociation with pH, was believed to result in the reduced flux. Miyaki and Fujimoto [15] have also observed the ion dissociation effect on flux in the dialysis of acetic acid, citric acid and ascorbic acid with a charge-mosaic membrane.

According to Kielland [16], the diameters of hydrated ions H^+, Na^+ and NH_4^+ are 9Å, 4-4.5Å and 2.5Å, respectively. In terms of size, the bigger ions had lower rates of diffusion and were expected to have lower permeate concentration. However, the capability of the H^+ and NH_4^+ ions to form hydrogen-bonds with the carbonyl groups of the polyamide membrane could promote ionic passage. At similar ionic concentrations, the larger hydrated size and the non-hydrogen-bonding characteristics of Na^+ as compared with NH_4^+ are believed to have contributed to the lower permeate concentration and greater solute reduction factor of sodium lactate compared to that of ammonium lactate. These effects are even more obvious at a higher operating pressure (Table 2). Lactic acid (at pH 2.2) did not attain the greatest solute reduction factor (Fig. 3) and its lowest permeate concentration (Fig. 4), despite the largest hydrated size of H^+, was likely attributed to its lowest ion concentration (Table 1) and its hydrogen-bonding capability, in addition to

Table 1 Chemical compositions of various feeds at different pH values (mol/ℓ)

	Feed				
	LacH (pH 2.2)	NH_4Lac (pH 5.4)	LacH (pH 5.6)	NaLac (pH 7.2)	NaLac (pH 11.5)
$[H^+]$	7.08E-3	3.98E-6	2.51E-6	6.31E-8	3.16E-12
$[Na^+]$	—	—	0.266	0.268	0.271
$[NH4^+]$	—	0.269	—	—	—
$[Lac^-]$	7.08E-3	0.269	0.266	0.268	0.268
$[OH^-]$	1.41E-12	2.51E-9	3.98E-7	1.58E-7	3.16E-3
[LacH]	0.326	1.41E-3	4.37E-3	1.10E-4	5.50E-9
$[NH_3]$	—	1.78E-5	—	—	—
[Total ions]	0.014	0.538	0.537	0.536	0.542

Table 2 Fluxes and solute reduction factors at 3 and 7 MPa for different feeds (readings taken at 200 ml of permeate)

MPa	Feed					
	Sodium lactate		Ammonium lactate		Lactic acid	
	Flux ($m^3.m^{-2}.d^{-1}$)	C_b/C_p	Flux ($m^3.m^{-2}.d^{-1}$)	C_b/C_p	Flux ($m^3.m^{-2}.d^{-1}$)	C_b/C_p
3	0.18	73	0.25	32.1	0.63	2.48
7	0.40	85	0.70	36.9	1.01	9.33

the swelling of polyamide membrane (Fig. 2). The unexpected increase in permeate concentration for ammonium lactate in the latter half of the filtration process (Fig. 4) was believed to be due to concentration polarization; its small hydrated ion size and hydrogen-bonding capability also helped to enhance the solute leakage.

At this stage, ammonium hydroxide (at 3.0%) offering a rejection of 91%, despite the concentration polarization effect its lactate incurred in the latter half of the process, is considered to be the optimum pH-controlling agent to be used in lactic acid production. Moreover, its capability to augment cell growth and productivity by acting as a nitrogen source [17] has further supported its use. On the other hand, sodium lactate, despite its high solute retention capability, offered an extremely low flux, and permeate collection was time consuming; for instance it took 600 min to collect 250 ml of permeate as compared to 360 min to collect ammonium lactate. Sodium hydroxide is therefore not recommended in this process.

3.3 Operating effects

3.3.1. Pressure applied

Figs. 7 and 8 illustrate the relationship of applied pressure to flux (J), observed solute rejection (R_{obs}), permeate concentration (C_p), bulk concentration (C_b), rate of solute losses (Rsl_t and Rsl_v) and total solute loss (Tsl) using a 1.0% ammonium lactate solution concentrated at 900 rpm; data were taken at the 150th min of filtration process for comparison. As the pressure was increased from 3 to 7

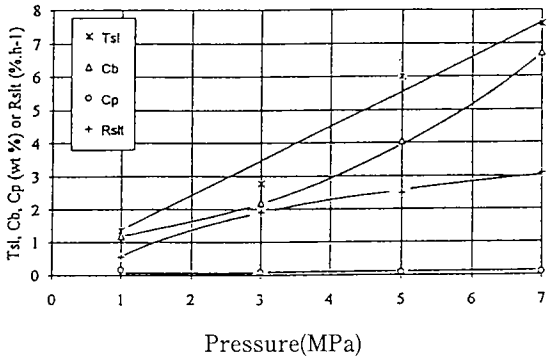

Fig. 7 Pressure effects on total solute loss, permeate and bulk concentrations, and rate of solute loss

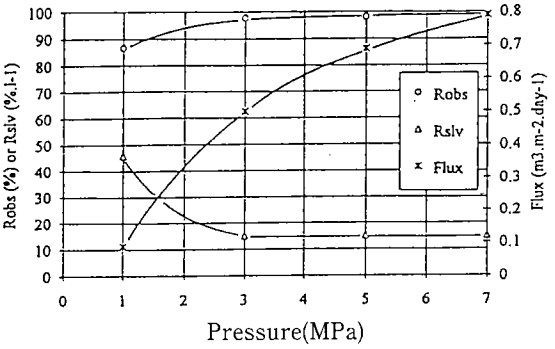

Fig. 8 Pressure effects on solute rejection, rate of solute loss and flux using 1.0% ammonium lactate solution

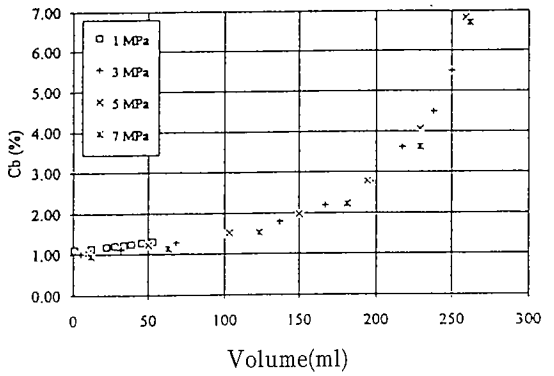

Fig. 9 Bulk concentration profile at various pressures

MPa, flux, bulk concentration, solute rejection, rate of solute loss (Rsl_t) and total solute loss were increased, with an insignificant change in permeate concentration and rate of solute loss (Rsl_v). Fig. 9 further shows that the increase in bulk concentration with increasing pressure was attributed to the larger quantity of permeate obtained as a result of higher flux. The lower flux and the greater permeate concentration at 1 MPa (i.e., Cp of 0.16% as compared to 0.08% recorded at the other pressures) have resulted in a higher Rsl_v and hence a lower Robs at this particularly low pressure at a given time. However, the increasing Rsl_t with pressure has incurred a greater loss in the total amount of solute (Tsl). In conclusion, an increment of pressure would offer a greater flux, which overweighs the effect of increasing total solute loss and consequently contributes to an increase in solute rejection. Glueckauf and Sammon [18] explained the increased rejection with increasing pressure on the basis of dielectric constant of water content. 7 MPa is considered to be an optimum operating condition in this process, with the cost of losing a certain amount of solute (i.e., Tsl of 7.59%).

Table 2 compares the flux and solute reduction factor for various feed solutions. These results indicate an increase in solute reduction factor with an increase in pressure, suggesting that lactic acid, sodium lactate and ammonium lactate did not show a strong solute-membrane affinity. A strong solute-membrane affinity

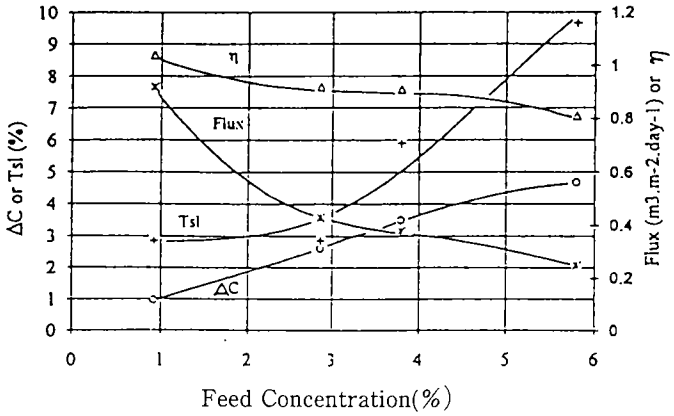

Fig. 10 Effects of feed concentration on flux, concentration efficiency, bulk concentration difference and total solute loss

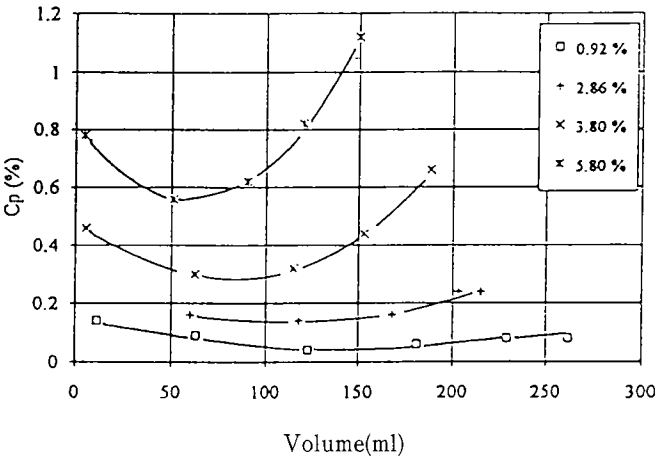

Fig. 11 Permeate concentration profiles at various feed concentrations

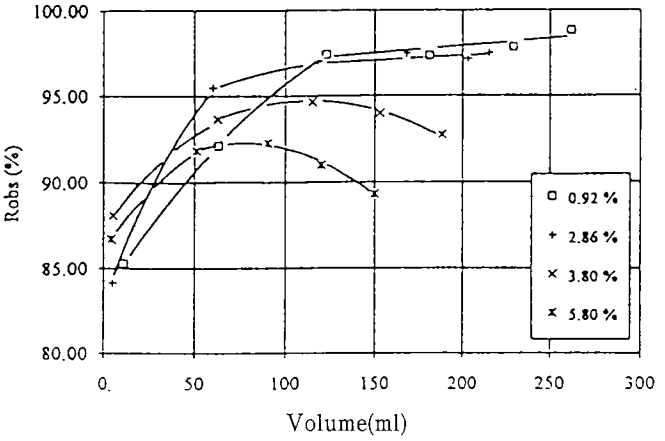

Fig. 12 Effects of feed concentrations on solute

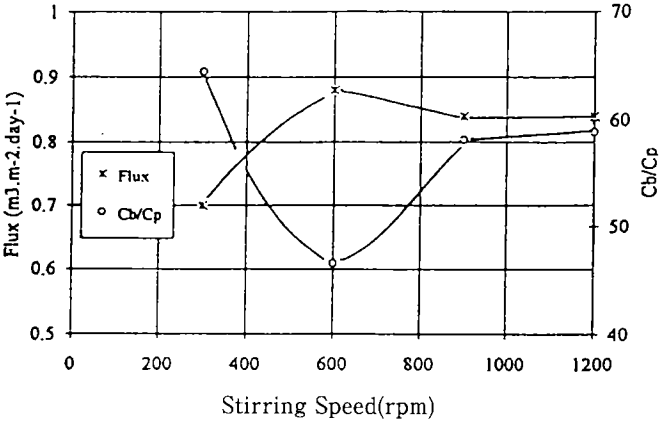

Fig. 13 Effects of stirring speeds on flux and solute reduction factor using a 1.0% ammonium lactate solution

system would show a decrease in solute reduction factor with an increase in applied pressure, as is the case for certain low molecular weight organics in water such as benzene, toluene and phenol derivatives, which have been thoroughly studied by several authors [19-23].

3.3.2. Feed concetration

Fig. 10 depicts the relationship between C_f and flux, Tsl, bulk concentration change (ΔC_b), or concentration efficiency (η) using ammonium lactate solution filtered at 7 MPa and 900 rpm; data were taken when 150 ml of permeate was obtained. As feed content was increased from 0.92% to 5.80%, flux was decreased from 0.92 $m^3 .m^{-2}.d^{-1}$ to 0.25 $m^3 .m^{-2}.d^{-1}$, while Tsl was increased from 2.86% to 9.66%. This has resulted in a reduced concentration efficiency from 1.04 to 0.81, despite the increment of C_b from 0.96% to 4.68%. The increase of osmotic pressure from 0.7 MPa to 1.4 MPa obtained experimentally and the increase of viscosity of solution as a result of increased molecular interaction [24], resulting in higher resistance to flow, could well explain the decrease of flux when feed was increased from 0.92% to 5.80%. Fig. 11 reports an increase of permeate concentration or solute leakage with feed concentration. Also, the permeate concentration at all feed concentrations studied shows a similar profile of an initial decrease followed by an increase, with volume of permeate obtained. The latter increase was attributed to the concentration polarization where the effect was further augmented with feed concentration as indicated by a greater positive gradient (Fig. 11). This leads to a reduced solute rejection as filtration proceeded, especially as feed concentration increased, $\geqq$3.80% in this case, as illustrated in Fig. 12.

3.3.3. Stirring speed

Fig. 13 illustrates the effects of variations in stirring speed on the flux and solute reduction factor using a 1.0% ammonium lactate solution concentrated at 7 MPa. The results indicate an increase of flux from 0.70 $m^3.m^{-2}.d^{-1}$ to 0.88 $m^3.m^{-2}.d^{-1}$ (i.e., +25.7%) from 300 rpm to 600 rpm, yet decreased to 0.84$m^3.m^{-2}.d^{-1}$ (i.e., 4.5 %) with a further increase up to 1200 rpm. However, the increase in flux at 600 rpm was also accompanied by a decrease in the solute reduction factor from 64.5 to 46.5. In spite of the similar fluxes and reduction factors attained at 900 rpm and 1200 rpm, mechanical instability was observed at 1200 rpm. This indicates an optimum stirring speed of 900 rpm.

4. Conclusions

The physico-chemical and operating effects of lactic acid, sodium lactate and ammonium lactate on the RO process have been investigated using a polyamide composite membrane. This particular type of membrane was found to swell at pH 2.2 but had no detectable solute-membrane affinity. The flux and permeate concentration were found to be an inverse function, whereas the solute reduction factor was a direct function of the pH value of feed. This was attributed to the greater concentration of ions dissociated into the solution as the pH was increased, and the fact that hydrated ions possess larger sizes than molecules by merit of their charge densities is believed to help enhance rejection by their lower rates of diffusion.

At this stage, ammonium hydroxide is considered to be the optimum pH-controlling agent for lactic acid production by virtue of its reasonably high flux and solute rejection as well as its capability to aug ment cell growth by acting as a nitrogen source. In terms of operating conditions, an increase in pressure from 1 MPa to 7 MPa has contributed to a higher flux, which overweighs the effect of the increasing total solute loss and consequently leads to an increase in solute rejection. On the contrary, an increase in feed concentration, especially to$\geqq$3.80%, has incurred pronounced effects on concentration polarization, leading to a reduced solute rejection and concentration efficiency. The optimum operating conditions were estimated to be 7 MPa and 900 rpm.

5. Symbols

C —Concentration, wt%
C —Concentration difference, wt%
J —Flux, $m^3.m^{-2}.d^{-1}$
Rob_S —Observed solute rejection, %
Rsl_t —Rate of solute loss based on time, $wt\%.h^{-1}$
Rslv —Rate of solute loss based on volume of permeate, $wt\%.L^{-1}$
t —Time, h
Δt — Time difference, h
Tsl —Total solute loss, wt%
V —Volume, m^3
η —Concentration efficiency
ρ —Density, $kg.m^{-3}$

Subscripts
b —bulk solution
f —feed solution
i —initial volume
p —permeate volume

Acknowledgements

The authors wish to express their gratitude to the Japan Research Development Cqrporation (JRDC) for its financial support for this work under the Science and Technology Agency Fellowship Program.

References

[1] M. Hongo, Y. Nomura and M. Iwahara, Appl. and Environ. Microb., 52 (1986) 314.
[2] K.H. Kroner et al., in: Membranes and Membrane Process, E. Drioli and M. Nakagaki, eds., Plenum Press, New York 1986.
[3] M. Fontyn, K. Van't Riet and B.H. Bijsterbosch, Membraantechnologie, 2 (1987) 31.
[4] M.K.H. Liew, A.G. Fane and P.L. Rogers, Biotech. Bioeng., submitted.
[5] P. Boyaval, C. Corre and S. Terre, Biotech. Lett., 9 (1987) 207.
[6] Y. Nomura, K. Yamamoto and A. Ishizaki, J. Ferm. and Bioeng., 71 (1991) 450.
[7] H. Nabeya et al., Proceedings of the 55th Chemical Engineering Conference in Japan, 1990 p. 581.
[8] V.M. Starov and N.V. Churaev, Kolloidn. Zh., 50(5) (1988) 932.
[9] M.J. Hurndall et al., Desalination, 90 (1993) 45.
[10] H.K. Lonsdale, in: Desalination by Reverse Osmosis, U. Merten ed., MIT Press, Cambridge, MA, 1966.
[11] L.G. Sillen, in: Treatise on Analytical Chemistry, I.M. Kolthoff and P.J. Elvings, eds., Interscience, New. York. 1959.
[12] W.Stumm and J.J.Morgan, in: Aquatic Chemistry: An Introduction Emphasizing Chemical Equilibria in Natural Water, Wiley, New York 1970, p. 69.
[13] P. Lenard, W. Weick and H. Ferd, Ann. Physik., 61 (1920) 665.
[14] J. W. Mellor, Mellor's Comprehensive Treatise on Inorganic and Theoret-
ical Chemistry, Vol. 1, Longmans, UK, 1963.
[15] Y. Miyaki and T. Fujimoto, in: Membrane Science and Technology, Y. Osada and T. Nakagawa eds., Marcel Dekker, New York, 1992 p. 61.
[16] J. Kielland, J. Am. Chem. Soc., 59 (1937) 1675.
[17] Workshop, Advance Utilization of Biomass in Cold Region, Hokkaido National Industrial Research Institute, Japan, 1994.
[18] E. Glueckauf and D. Sammon, Proc. Third Int. Symp. Fresh Water from the Sea, Dubrovnik, 2 (1970) 397.
[19] H.K.Lonsdale, U.Merten,M.Tagami, J. Appl. Polym. Sci., 11 (1967) 1807.
[20] T. Matsuura and S. Sourirajan, J. Appl. Polym. Sci., 15 (1971) 2905.
[21] H. G. Burghoff, K. L. Lee, and W. Pusch, J. Appl. Polym. Sci., 25 (1980) 323.
[22] D.R. Lloyd, M. Babai-Pirouz and J. M.Dickson, J. Sep. Tech., 3 (1982) 21.

[23] H. Mehdizadeh and J.M. Dickson, AIChE J, 39 (1993) 434.
[24] N.I.Prokhorenko et al., Dokl. Akad. Nauk. Ukr. SSR. Ser. B: Geol., Khim. Biol.Nauki., 1 (1988) 50.

Raman Spectroscopic Analyses on the Growth Process of CO_2 Hydrates*1

(Key Word : CO_2 hydrate Raman spectroscopy, Deep sea, CO_2 sequestration)

Tsutomu UCHIDA*2, Akifumi TAKAGI*3, Junichi KAWABATA*4, Sinnji MAE*3 and Takeo HONDOH*5

1. Introduction

Carbon dioxide disposed in the ocean at depths below about 500 m will form a CO_2 hydrate layer at the interface with sea water. This hydrate layer is expected to control the CO_2 dissolution into the sea water, and the acidity of sea water[1]. The injection of CO_2 hydrates themselves in the ocean has been proposed as an option of CO_2 disposal because of their physical stability[2].

CO_2 hydrate ($CO_2 \cdot nH_2O$) is crystalline molecular complex which includes a large quantity of CO_2 molecules, and is stable at high pressure and low temperature conditions. n is the molecular fraction of water reacted with a mole of CO_2, which is called a hydration number. The structure of the CO_2 hydrate is a unit cell consisting of 46 water molecules enclosing two small and six large cages, each of which can include a CO_2 molecule. If all cages are occupied by CO_2 molecules, n becomes 5.75 and the density of CO_2 hydrate is about 1.13 g cm^{-3}, which is larger than that of sea water.

For detailed assessment of the behavior of the CO_2 injected in deep oceans, it is necessary to clarify not only the growth process of CO_2 hydrate, but also its physical properties. If n depends on its growth conditions, the density of the formed CO_2 hydrate would change. However, such physical properties of CO_2 hydrate have not been well studied. It is therefore important to study both the growth process and physical properties of CO_2 hydrate simultaneously. In the present study, we observed the growth process of CO_2 hydrate and performed the Raman spectroscopic analysis on the formed CO_2 hydrate. The typical raman spectra of both CO_2 and H_2O molecules in CO_2 hydrate were determined. Then we will present an attempt to evaluate the density of CO_2 hydrate with these raman spectra.

2. Experimental Procedures

A pressure vessel with about 4 cm^3 in volume had silica glass windows. These windows allowed us to observe the growth processes of CO_2 hydrate and to measure its raman spectra simultaneously. A cooling rod was inserted in the vessel to form the CO_2 hydrate at the center of the vessel. At a suitable temperature and pressure conditions, the CO_2 hydrate was formed only around the rod and transparent CO_2 hydrates grew slowly. This optical setting gave clear images of the growth process and prevents the dispersion of laser beam at any unexpected site in the vessel.

---

* 1 This paper was reproduced from Energy Convers. Mgmt., Vol.36,No.6-9, (1995)pp.547-550 by the permission of Elsevir Science Ltd., Great Britain.,
* 2 Resources and Energy Division
* 3 the Department of Applied Physics, Faculty of Engineering, Hokkaido Univ.
* 4 Material Division
* 5 the Institute of Low Temperature Science, Hokkaido Univ.

Ar^+ laser (λ = 488 nm) and JEOL-JRS-400T type spectrometer with triple monocrometer were used for raman spectroscopic analysis. The scattered light was multiplied by photomultipler (Hamamatsu TV R585) and recorded by a computer. Experimental conditions were as follows: temperature and pressure of the vessel were Tv = 278.3 - 282.7 (±0.1) K and P = 3.93 - 4.60 (± 0.06) MPa, respectively. Temperature of the cooling rod (Tcr) was set between 263.4 and 276.2 K.

3. Results and Discussions

Fig. 1 shows transparent CO_2 hydrates growing around the cooling rod under conditions of Tv = 282.2 K, Tcr = 268.9 K and P = 4.56 MPa. The growth rate of CO_2 hydrate decreased logarithmically of order from 10^{-3} to 10^{-5} mm $hour^{-1}$. Here the growth rate was regarded as the increasing rate of CO_2 hydrate thickness. At the boundary between CO_2 hydrates and CO_2 solution, we observed polyhedral facets of CO_2 hydrate crystals (Fig. 1b and c). The formation of facets indicates that formed CO_2 hydrates were crystalline solids.

Then, raman spectra of formed CO_2 hydrates were measured. Fig. 2 shows the typical example of raman spectra of the CO_2 hydrate (solid line) and CO_2 solution (dashed line). Two large peaks of CO_2 molecules are observed between 1250 and 1450 cm^{-1}. Other peaks are the raman

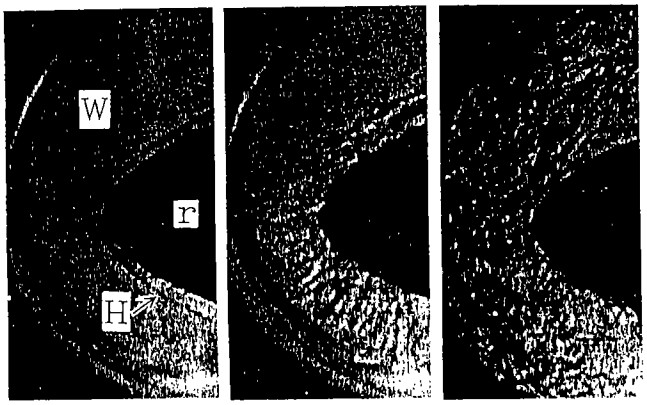

Fig. 1 : In situ observation of crystal growth process of CO_2 hydrate. a) initial state, b) after 1 hour, c) after 14 hours. r: cooling rod, H: CO_2 hydrate, W: CO_2 solution. 1mm

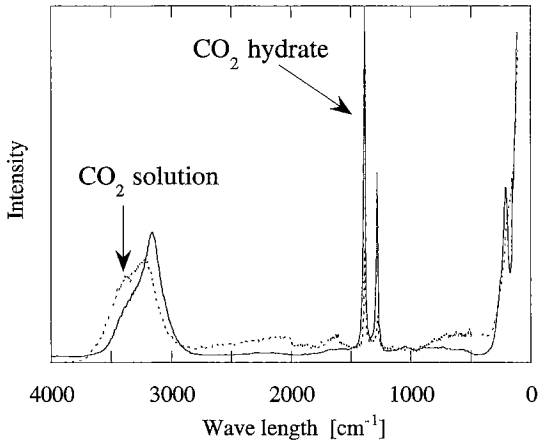

Fig. 2: Raman spectra of CO_2 hydrate (solid line) and CO_2 solution (dotted line)

spectra of H_2O molecules. We found some characteristics of raman spectra of CO_2 hydrate as follows: (i) raman intensities of CO_2 molecules in CO_2 hydrates were considerably larger than those in CO_2 solution. (ii) Raman peaks of CO_2 molecules in the CO_2 hydrate were 1380.7 and 1277.8 (±0.5) cm-1 and those in CO_2 solution, 1382.5 and 1276.5 (±0.5) cm^{-1}. (iii) Raman peaks of H_2O molecules in the CO_2 hydrate were similar to those of ice. (iv) Raman intensity ratio of both CO_2 and H_2O molecules between CO_2 hydrates and CO_2 solution varied with growth conditions of CO_2 hydrates.

Result (i) indicates that CO_2 hydrates formed in the present study included a large amount of CO_2 molecules. Result (ii) would be caused by the fact that molecular vibrations of CO_2 in a cage were slightly disturbed. Result (iii) shows that the CO_2 hydrate was the crystal whose hydrogen bonds were similar to those of ice crystals. This is supported by the structural analysis of CO_2 hydrate by X-ray diffraction[3]. According to these characteristics, we can distinguish raman spectra of CO_2 hydrate with those of CO_2 solution.

Result (iv) indicates that molecular concentrations of a CO_2 hydrate grown form CO_2 solution depended on its growing conditions. Here we present an attempt to estimate the hydration number, n, by the comparison of raman intensities. As we measured raman spectra after the growth rate of CO_2 hydrate reaching to zero, we considered the concentration of CO_2 mole-

cules in CO_2 solution to be saturated. Then the molar fraction of CO_2 in the solution, $[CO_2]_w$ / $[H_2O]_w$, was represented by CO_2 solubility data[3], and the molar fractions of H_2O and CO_2 in CO_2 hydrate, $[H_2O]_h$ / $[CO_2]_h$ = n, can be obtained as follows:

$$n = \frac{[H_2O]_h}{[CO_2]_h} = \frac{[I_{H_2O}]_h}{[I_{H_2O}]_w} / \frac{[I_{CO_2}]_h}{[I_{CO_2}]_w} \cdot \frac{[H_2O]_w}{[CO_2]_w} \qquad (1)$$

where $[I_{H2O}]_h$ / $[I_{H2O}]_h$ is the intensity ratio of H_2O molecules between in CO_2 hydrate and in CO_2 solution, and $[I_{CO2}]_h$ / $[I_{CO2}]_w$ is those of CO_2 molecules. Here we assumed that, in the present study conditions, the raman intensities of both H_2O and CO_2 depend linearly on their molar fractions. By substituting each value into equation (1), we obtain n to be about 7.68 at Tv = 282.2 K, Tcr = 268.8 K and P = 4.56 MPa. At another condition, that is Tv = 282.7 K, Tcr = 276.2 K and P = 3.93 MPa, n is about 7.24. These are considerably larger than 5.75, which corresponds to the hydration number of the CO_2 hydrate whose cages are fully occupied by CO_2 molecules.

The CO_2 hydrate whose cages are fully occupied has larger density than liquid CO_2 and sea water under deep sea conditions[4]. However, CO_2 hydrates formed in the present study had small densities. The density of CO_2 hydrate (ρ) can be calculated with n as follows:

$$\rho = 46\left(18 + \frac{44}{n}\right) R^{-1} a^{-3}$$

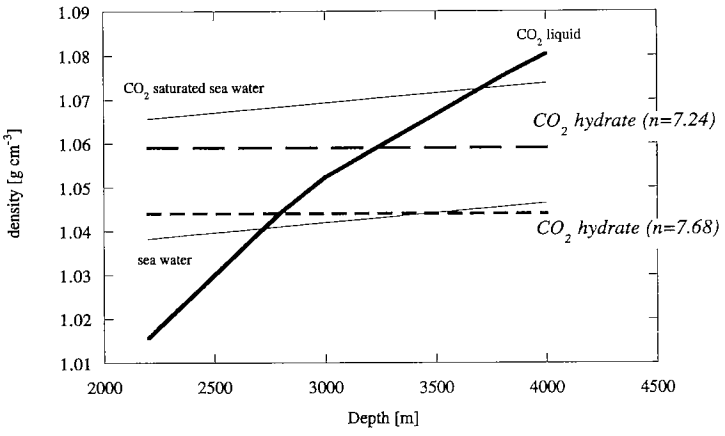

Fig. 3: Approximate estimation of relation between density and depth of the ocean.

where R is Avogadro constant and a is the lattice constant. With considering the temperature dependence of a[5], ρ is about 1.04 g cm^{-3} for n = 7.68, and 1.06 g cm^{-3} for n=7.24. Fig.3 shows a rough estimation of the relation between densities and depth of sea water below 2500 m. This figure indicates that at the depths larger than 3700 m the density of liquid CO_2 is larger than that of CO_2 saturated sea water[4]. However, densities of CO_2 hydrates formed in the present study are smaller than not only liquid CO_2 but also CO_2 solution at a depth deeper than about 3000 m. The density change of CO_2 hydrate would seriously affect its stability and the CO_2 dissolution rate into sea water. We are now investigating how the density of CO_2 hydrate depends on the formation and growth conditions of CO_2 hydrates.

Acknowledgments

This study was supported by fundamental works performed by Mr. Y. Kato and Mr. M. Hirano in Hokkaido University. The authors express gratitude to Dr. S. M. Masutani, Dr. H. Unuma, Dr. A. Kouuchi, Dr. T. Ohsumi and Dr. H. Narita for their helpful discussions. They also thank Dr. K. Yoshikawa of Mitsubishi Heavy Industries, Ltd. for his support of experimental apparatus.

References

1. I. Aya, K. Yamane and N. Yamada, Proc. of the Int. Symp. on CO_2 Fixation and Efficient Utilization of Energy (eds. Y. Tamaura et al), RCCRU of Tokyo Inst. of Tech., Tokyo, 351 (1993).
2. A. Saji, H. Yoshida, M. Sakai, T. Tanii, T. Kamata and H. Kitamura, Energy Convers. Mgmt., 33, 643 (1992).
3. T. Uchida, T. Hondoh, S. Mae and J. Kawabata, Global and Planet. Change (special issue), in press.
4. Y. Shindo, Y. Fujioka, M. Ozaki, K. Takeuchi and H. Komiyama, Proc. of the

Int. Symp. on CO_2 Fixation and Efficient Utilization of Energy (eds. Y. Tamaura et al), RCCRU of Tokyo Inst. of Tech., Tokyo, 307 (1993).
5. J.S. Tse, J.Phys. (Paris), 48, C1-543 (1987).

木材の熱分解によるレボグルコサンの収率に及ぼす昇温速度の影響*1

（キーワード：加熱速度、急速熱分解、木材、無水糖、レボグルコサン、赤外線加熱炉）

三浦　正勝*2・田中　重信*2・安藤　公二*3

セルロースは、(+)-D-グルコースが 1,4-β-グルコシド結合で連結した直鎖状の高分子であり、この結合を熱分解で切断するとグルコースの無水物であるレボグルコサン（1.6 Anhydro-β-D-glucopyranose）が得られる。 Pictetら[13]は、セルロースやでん粉を減圧下で乾留すると比較的多量のレボグルコサンが生成することを見い出した。その後もセルロースをはじめコットン、綿ネル、および 6炭糖類などの減圧熱分解でレボグルコサンが確認されている[1,2,4]。 Fisherら[1]、Wacekら[18]、Shafizadehら[14]、三浦ら[10]、中川ら[12]および小島ら[7]は、セルロースを約50 %含む木材からのレボグルコサンの生成を確認している。Shafizadehら[14,15,16]は、セルロース、綿および紙類の熱分解についての基礎実験を行い、純セルロースからのレボグルコサンの収率は大気圧下と比較し0.25 kPaの減圧下では約2倍になり、最大約40 %得られたことおよび木材を含むセルロース系物質に含まれる無機物質などの不純物をリン酸や硫酸処理によって除くとその収率が著しく向上したと報告している。中川ら[12]は、成長の早い南洋材のイピルイピルを前処理として加水分解し、Shafizadehら[14]と同様の装置にて減圧下で熱分解してレボグルコサンの生成速度に関して解析を行い、生成速度定数の実験式を提示している。小島ら[7]は、4種の木材を流動層で熱分解し、常圧で 1.0～3.9 %のレボグルコサンを得ている。さらに、前処理で木材中の無機物質を減少させることによってレボグルコサンの収率が6～9 %増加したことから、K,Mgなどの無機物質がレボグルコサンを含むタール生成物の二次的熱分解を促進させたとしている。一方、Kollら[8]および村木ら[11]は、超臨界抽出法を適用し、超臨界のアセトン流体中でセルロースの熱分解を行い、 Kollらは 2.5x10^4 kPa、613 Kの超臨界条件下で38.8 %のレボグルコサンを得ている。つまりセルロースの熱分解温度(513～623 K)[6]以上の高温を避けるとともに生成したレボグルコサンをアセトン気流で反応炉から速やかに抜き出すことによって高圧にも関わらず Shafizadehの減圧条件と同様なレボグルコサン収率を得たと推察される。このようにレボグルコサン収率が向上したのは、いったん生成したレボグルコサンが減圧あるいは超臨界流体による抽出法や金属成分などの不純物を除く前処理によって、二次的熱分解が抑制されたためと考えられる。

木炭製造においては、最初から高い温度で炭化速度を速めるとその収炭量が少なくなることから、温度が比較的低い緩徐の操作で行うのが適当とされている[17]。われわれはこの収炭量の増加の原因について、緩徐の温度つまり昇温速度が小さい条件では、低次分解生成物が粒子外に留出せず重合によって粒子内に固定されるので炭化物収率が大きく、昇温速度の増大と共に低次分解生成物の留出量が増大するのでこれに含まれるレボグルコサンの収率向上が期待され、一方、炭化物の収率は減少すると考えた。

本報では、赤外線加熱炉を用いて常圧近傍でカラマツ材の熱分解を行い、レボグルコサンと炭化物の収率に与える昇温速度の影響を検討した。また、減圧の効果との比較を行った。

1．実験装置および方法

試料には、北海道産のカラマツ（フルイ目 1.2～2.4 mmの破砕物）1.6～3 gを風乾状態で供した。Fig.1に実験装置の概略を示す。急速熱分解実験装置には、赤外線加熱炉（ヤマト科学製： FR-21）を使用した。この炉は無負荷の状態では室温から1273 Kまで約5秒間で昇温できる。熱分解反応管は、図示のような内径18 mm、長さ 350 mmのステンレス製管で、垂直に設置した。ステンレス製カプセル容器（ 内径15 mm、長さ80 mmの円筒状、 1 mmφの多孔壁）に試料を充填して反応管の上部より挿入し、カプセルが加熱域のほぼ中心にくるように設置した。昇温速度および熱分解温度の制御は反応管の外壁で行い、実験条件の設定および結果の解析にはこの制御点の温度を用いた。

*1 化学工学論文集, Vol.No.4(1995)pp843-846(化学工学会より転載許可)
*2 低温生物化学部
*3 室蘭工業大学

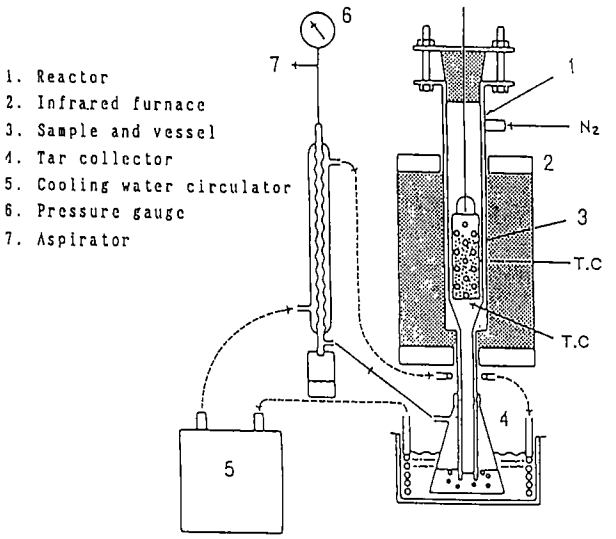

Fig.1 Schematic diagram of experimental set-up

実験条件は、熱分解温度Tを593～923 K、昇温速度Hrを0.25～ 3.33 K/sおよび設定温度での保持時間tHを60～1200 sとした。反応管の上部より窒素ガスを流し、その管内空塔速度UN2は、常温常圧基準で2.2および3.4 cm/sとした。系内の圧力 Pは、揮発物やタールの速やかな抜き出しを兼ね、反応管の下部に設置したタール溜めのガス抜き出し口から水流ポンプで吸引して調整した。タール溜めには予め 278～283 Kに冷却したメタノールを仕込み、発生した熱分解ガスはこの溶剤と接触させた後、凝縮管を経て水流ポンプで系外に排出した。

熱分解後、生成炭化物量を秤り、反応管と配管経路に付着しているタール分はメタノールで洗浄し、洗浄液を含む熱分解液全量を313 K以下で減圧濃縮した。濃縮液中のレボグルコサンの濃度を前報[10]と同じくキシリトールを内部標準物質に使い、トリメチルシリルエーテル誘導体としてガスクロ法で定量した。なお、条件によってはレボグルコサンに対し0～10数%程度の肩ピークが認められた。そのピークの分離が困難であったことから、レボグルコサンの収率は肩付きピークを含めた見掛け濃度から求めた。

2．結果および考察

2.1 圧力P の影響

熱分解による炭化物とレボグルコサンの収率（それぞれYcとY_{LG}）に及ぼす圧力の影響をFig.2 に示す。同一条件下では、減圧度が大きくなるほどY_{LG} は大きく、Ycは小さくなる傾向が現れている。 Y_{LG} は、大気圧下で約3 %、35 kPaでは、その2.6 倍の 7.8 %となり予想通り減圧が Y_{LG}を向上させるための一方法

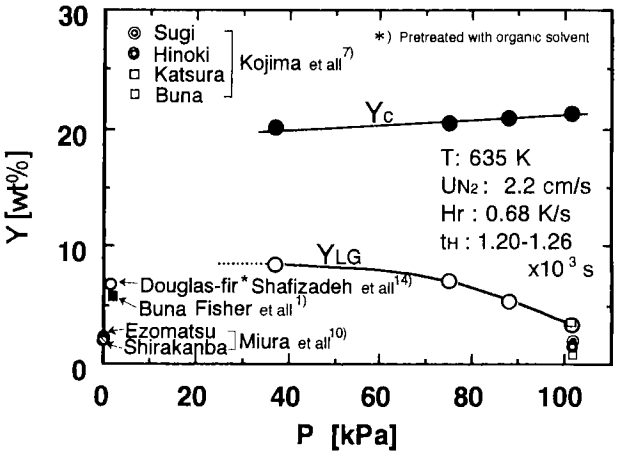

Fig.2 Effect of reduced pressure on the yield of pyrolytic products

であることが確認された。しかし、Y_{LG}は常圧から75 kPaまではほぼ直線的に増加しているが、さらに減圧度を倍以上に大きくした 35 kPaのY_{LG}は極微量の増加にとどまっている。既往の報告によれば、樹種および熱分解装置やその操作条件は異なるが、同図中に示したように圧力が 0.25 kPaにおける木材の Y_{LG}は 0.5 ～ 5.6 %である。したがって、減圧の程度を既往の報告のように著しく大きくしてもそれに対応してY_{LG}が大きくなる可能性は少ない。

小島ら[7]は、流動層を用いて673 K、常圧でスギ、ヒノキ、カツラおよびブナの熱分解を行った。Fig.2中に示した小島らのY_{LG}は、木材の種類によって異なっており厳密な比較は困難であるが、常圧におけるY_{LG}としてはカラマツについての本実験結果(Y_{LG} 3.3 %)と同程度の値からその約1/3の間に分散している。流動層の場合、急速加熱の面で優れている。一方、レボグルコサンの抜き出し口は上部であることとフリーボード部でのレボグルコサンの滞留が避けられないことのため、重質で熱的に不安定なレボグルコサンの高次熱分解が促進されY_{LG}が小さくなっている可能性もある。

2.2 昇温速度Hrの影響

Fig.3 に、Tが693 K、Pが常圧に近い88 kPaの条件下でのHrとYとの関係を示す。YcはHrが大きくなるにしたがい減少している。すなわち、Yc、Y_{LG}に対するHrの増大の影響は、Fig.2におけるPの減少と同様の影響が現れている。Y_{LG}はHrが0.25 K/sで 4.5 wt%、1.3 K/sでは最大値となり1.7 倍の7.8 wt%である。Y_{LG}はHrが1.3 K/s付近まではほぼ直線的に増加するが、Hrが1.7 K/sでは逆に減少している。この原因は、Hrが著しく大きくなると表面温度が高くなり、いったん生成したレボグルコサンが表層部で高次分解したためと考えられる。

純セルロースであるロ紙を約5 mm角に裁断してそ

れをHr=1 K/sの条件で熱分解した場合のY_{LG}(f.p)をFig.3中に◎印で示した。その見掛けのY_{LG}は、カラマツの約4 倍の22 %であった。Shafizadeh[14]らは、セルロース粉末を原料に大気圧・窒素雰囲気下で熱分解を行い16～19%の Y_{LG}と2～数 %の1.6 Anhydro-β-D-glucofuranoseを得ている。Shafizadehらの場合は、本実験より圧力が若干高く粒子が小さい。また、Hrが不明であり、本実験の結果はレボグルコサンの見掛け濃度であることを考慮すれば両者のセルロースを原料としたY_{LG}は同程度の値と見ることができよう。一方、カラマツの同一熱分解条件におけるY_{LG}は約5 %強である。カラマツのセルロース含量は約 50 %であることから、セルロース基準のレボグルコサン変換率は、ロ紙に比べて1/2以下の低い値となった。この原因は、Grayら[3]および小島ら[7]が報告したように木材中のK、Na、Ca、Mgなど無機物質による二次分解促進効果によるものと考えられる。

以上のことより、木材の熱分解糖化においては適切な昇温速度とタールの抜き出し方法を含めた高次熱分解の抑制が重要となる。さらに木材のリン酸処理[14]や微量の無機物質の除去操作[7]などとの併用によってレボグルコサンの収率の向上が期待される。

結　言

無処理カラマツの粒子を熱分解し、レボグルコサンと炭化物の収率（それぞれY_{LG}とYc）に及ぼす昇温速度 Hrおよび圧力Pの影響を検討し以下の結果を得た。

1) Y_{LG}の増大に対するPの減少の効果は、減圧度の小さい領域で顕著であり、高度の減圧は不要である。

2) Hrの増大は、Pの減少と同様Y_{LG}を増大しYcを減少させる。しかし、Hrが著しく大きくなるとY_{LG}は減少する。常圧に近い圧力 (88 kPa) で室温から693 Kまで 熱分解した結果、Hrが1.3 K/s近傍でレボグルコサン収率が最大となった。

Nomenclature

Hr	= heating rate	[K/s]
P	= pressure	[kPa]
T	= temperature	[K]
t	= reaction time	[s]
t_H	= holding time at maximum temperature	[s]
U_{N2}	= superficial nitrogen gas velocity	[cm/s]
Y_{LG}	= Yield of levoglucosan	[wt%]
Yc	= Yield of char	[wt%]

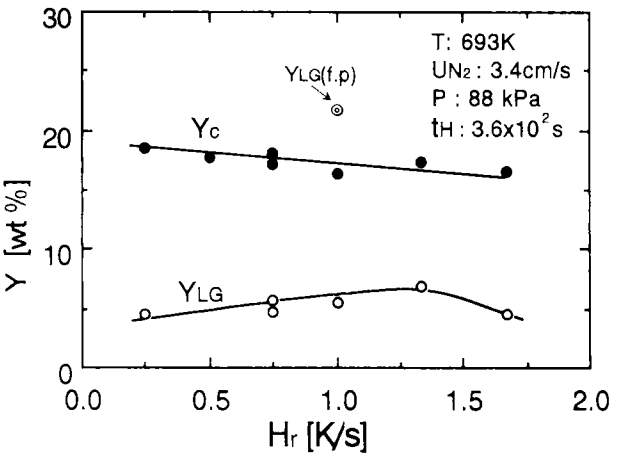

Fig.3 Relationship between yields of products and heating rates

Literature cited

1) Fisher,F.and H.Tropsch:Ber.,56,2418(1923); Sibamoto,T.and A.Kuriyama;Mokuzai Tanka, p.46～47(1952)

2) Gardiner,D.,; "The Pyrolysis of Some Hexoses and Derived Di-,Tri-,and Poly-saccharides", J.Chem.Soc.(c),.1473～1476(1966)

3) Gray,M.R.,W.H.Corcran and G.R.Gavalas ; "Pyrolysis of a Wood-Derived Material. Effects of Moisture and Ash Content",Ind. Eng. Chem. Process Des.Dev.,24,.646～651(1985)

4) Holmes,F.H .and C.J.G.Shaw ; "The Pyrolysis of Cellulose and the Action of Flame-Retardants. I.Significance and Analysis of the Tar",J. Appl.Chem.,11,.210～216(1961)

5) Imamura,H.,H.Okamoto , et al; "Mokuzai no Riyo no Kagaku", p32 Kyoritsu syuppan Co., Tokyo,(1983)

6) Ishihara,S.:Mokuzai no kagaku to Riyogijutsu 2.Bo·Taika seino, p.138, Nihon Mokuzai Gakkai Kenkyu-Bunkakai(1989)

7) Kojima,E.,Yelian,M. and S.Yoshizaki; "Catalytic Effect of Inorganic Components on the Yield of Levoglucosan from Wood Pyrolysis ", Kagaku Kougaku Ronbunsyu,16,.1138 ～ 1145 (1990)

8) Köll,P. and J. Metzger, ; "Thermischer Abbau von Cellulose und Chitin in Uberkritischem Aceton", Angew.Chem.,90,802～803(1978)

9) Kumagai,Y.,T.Ohuchi and M.Ono ; "Thermogravime-tric Analysis of Woods", Mokuzai Gakkaishi, 19,.265～270(1973)

10) Miura, M.,H.Kaga and H.Nishizaki ; "The Pyrolysis of Cellulosic Materials and Analysis of Levoglucosan in the Tar", Mokuzai Gakkaishi, 29,.759～762(1983)

11) Muraki,E.,and F.Yaku ; "Simplified Synthetic Method of Levoglucosan by Thermal Decomposition of Cellulose in Supercritical Acetone", Osaka Kogyogijutsu Shikensyo Kihou, 41,.22～26(1990)

12) Nakagawa,M., Y.Kamiyama and Y.Sakai; "Produc-tion Rate of Levoglucosan from Pyrolysis of Giant Ipil-Ipil Wood Cellulose", Japan J. Trop. Agr.,30,.160～165(1986)

13) Pictet,A. and J.Sarasin, Compt.Rend.,166,38 (1918);Helv.Chim. Acta.1,87(1918) : Sibamoto. T. and A Kuriyama;Mokuzaitanka, p.46, Asakurasyoten, Co., Tokyo(1952)

14) Shafizadeh, F., T.G.Cochran, Y.Sakai ; "Application of Pyrolytic Methods for the Sachari-fication of Cellulose",AIChE Symposium Series, 75,.24～35(1979)

15) Shafizadeh,F., R.H.Furneaux, T.G.Cochran, J.P. Scholl and Y.Sakai ; "Production of Levogluco-san and Glucose from Pyrolysis of Cellulosic Materials", J.Appl.Polym.Sci.,23,.3525～3539(1979)

16) Shafizadeh,F.and T.T.Stevenson ; "Saccharification of Douglas-Fir Wood by a Combination of Prehydrolysis and Pyrolysis", ibid, 27, .4577～4585(1982)

17) Uchida, K.: "Mokutan to kako tan",,p.23, Asaku-rasyoten Co.,Tokyo(1952)

18) Wacek,A.and H.Wagner;Oesterr.Chem.Ztg., 40,384,401(1937);B.C.A(B),1155(1937);Chem. Zentr., I,490 (1938);Hellstrom,N.; Acta Polytech.,9, 13(1947);C.A.,42,8446(1948); Sibamoto,T.and A;Kuriyama;Mokuzai Tanka, p.37,Asakurasyoten, Co.,Tokyo(1952)

Refractive Index Measurements of Natural Air-Hydrate Crystals in an Antarctic Ice Sheet*1

(Key Words: Air Hydrate, Refractive Index, Mach-Zehnder interferometer, Onsager cavity model, Cage occupancy)

Tsutomu UCHIDA*2, Wataru SHIMADA*3, Takeo HONDOH*3, Shinji MAE*4 and N.I.Barkov*5

1. Introduction

Ice-trapped bubbles are unique tools for the reconstruction of the composition of air. In the natural ice of glaciers, the ancient atmosphere has been trapped for hundreds of thousands of years. This occurs some 50-100 m below the surface of the polar ice sheets. At such depths, the snow gets so sintered that it transforms into ice, and the open pores between the snow crystals are definitively closed, thus trapping samples of the contemporaneous atmosphere.[1)]

At the depths of more than several hundred meters, these air bubbles change to air-hydrate crystals which are stable at high pressure and low temperature. Shoji and Langway[2)] first observed air-hydrate crystals in deep ice cores from Dye-3 Station, Greenland. They reported that the air-hydrate crystals were transparent and their diameters were less than 1 mm. Air-hydrate crystals also have been observed in some other polar ice cores.[3,4)]

The air-hydrate crystal is a molecular complex known as a clathrate, which is formed from mixtures of water and air molecules. Because air-hydrate crystals formed in the deep ice sheet are large single crystals, they give us more information than artificial polycrystal samples. X-ray diffraction studies on air-hydrate crystals in deep ice cores recovered at Dye-3 Greenland[5)] and Vostok Station, Antarctica,[6)] revealed that the space group is cubic Fd3m, and that a unit cell consisted of 136 water molecules enclosing 16 small and 8 large cage-like cavities in which air molecules (mainly N_2 and O_2) can be enclathrated.

The refractive index of air-hydrate crystals was revealed to be slightly higher than that of the surrounding ice matrix by the qualitative Becke test on air-hydrate crystals in deep ice cores.[2~4)] Davidson et al.[7)] suggested that the measurement of the refractive index together with use of the Onsager cavity model can yield good composition data for air-hydrate crystals, and they estimated the refractive index of air-hydrate crystals with some assumptions. However, because they are stable only in an ice matrix, no quantitative measurements of the refractive index of air-hydrate crystals have been performed.

The Onsager cavity model shows the relation between the refractive index of the air-hydrate crystal and the site occupancy ratio of air molecules for each cage, θ. Since the air volume stored in an air-hydrate crystal depends linearly on θ, it is important to measure θ for a paleoclimatic study on polar ice cores. Some attempts have been made to estimate θ of air-hydrate

---

*1 This paper was reproduced from Applied Optics, Vol.34,No.25, (1995)pp.5746-5749 by the permission of Optical Society of America,U.S.A.

*2 Resources and Energy Division
*3 the Institute of Low Temperature Science,Hokkaido Univ..
*4 the Department of Aplied Physics, Faculty of Engineering, Hokkaido Univ.
*5 the Arctic and Antarctic Research Institute, Russia.

crystals in polar ice. For example, an X-ray diffraction study on air-hydrate crystals in Dye-3 ice cores(1500 m depth) showed that θ was about 0.8.[5] Furthermore, the comparison between the air-hydrate volume and total air volume in Vostok ice cores indicated that θ varied from 0.58 to 1.0 in the depth range from 1250 to 2542m, indicative of ancient climatic changes.[4] However, previous methods of θ estimation were difficult, and included significant errors. However, the refractive index of air-hydrate crystals should provide precise values of θ by using the Onsager cavity model.

In the present study, we measured the difference of the refractive index between air-hydrate crystals and the surrounding ice matrix using a Mach-Zehnder interferometer. Using this unique technique, we can measure quantitatively the refractive index of each air-hydrate crystal easily. The ice samples we measured were deep ice cores from Vostok Station, Antarctica. These ice cores are important for the study of ancient climates, and for the study of air-hydrate crystals.

The results showed that the refractive index of air-hydrate crystals was slightly higher than that of the ice matrix, even considering the anisotropy of ice refractive index. We then applied the Onsager cavity model to relate the refractive index of air-hydrate crystals to their cage occupancy ratio.

2. Experimental Methods and Results

Air-hydrate crystals measured in the present study were found in an ice core of 2542 m depth, which was recovered at Vostok Station, Antarctica. This ice core is considered to include atmospheric air from about 220,000 years before the present.[8] Microscopic observations of these air-hydrate crystals[4] showed that most of them were ellipsoid shape, and that their mean diameter was about 125 μm.

Ice samples, with a dimension of about $3\times3\times30$ mm^3, were prepared from this ice core. Each ice sample included more than ten air-hydrate crystals. The ice samples were placed in the a cooling liquid in a cell made of optically flat glass plates,which was designed by Furukawa and Shimada.[9] The cell was cooled to about 270.2 K by blowing coldair over it. In order to prevent chemical etching of the ice surface and to diminish the light scattering at the surface, a mixture of Fluorinert FC70 and FC75 (Sumitomo 3M) was used as the cooling liquid. This cooling liquid gave clear images for the observation of air-hydrate crystals in the ice sample.

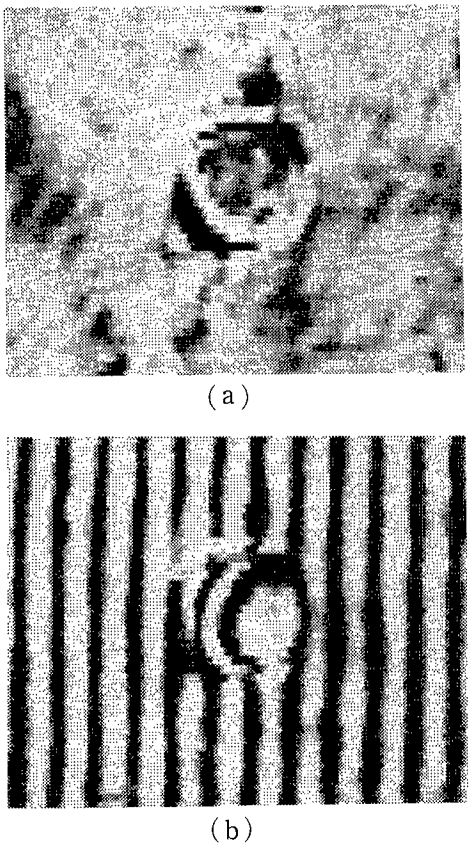

Fig. 1 Natural air-hydrate crystal observed by both (a) Schlieren system and (b) Mach-Zehnder interferometer. (a) An ellipsoid air-hydrate crystal is observed in the ice matrix. The diameter of this crystal is about 400 μm (b) The interference fringes on ice are parallel, but they shift about 1.4 times a line interval on the air-hydrate crystal.

Air-hydrate crystals in the ice sample were observed using a Mach-Zehnder interferometer.[9] Through the Mach-Zehnder interferometer, interference fringes are observed on the ice sample. When the re-

ference light of the interferometer is blocked by a chopper, this optical system changes to a Schlieren system, and the outline of the air-hydrate crystal can be observed clearly. Fig. 1 shows pictures of an air-hydrate crystal observed by (a) the Schlieren system and (b) the Mach-Zehnder interferometer.

The interference fringe shift at the air-hydrate crystal is dependent on both the crystal thickness and the refractive index difference between air-hydrate crystals and the ice matrix. In this case, the refractive index difference, Δn, is given as

$$\Delta n = \lambda s / d, \quad (1)$$

where d is the thickness of an air-hydrate crystal, λ = 0.6328 μm (at room temperature) is the wave length of a He-Ne laser, and s is the shift of interference fringes. In order to minimize systematic errors, we measured only air-hydrate crystals with a thickness greater than 125 μm, which is the average diameter of air-hydrate crystals of the 2542 m depth ice core.[4]

Table 1 lists the results obtained, which include the thickness of air-hydrate crystals and values of Δn given by equation (1). All of the values of Δn are positive, indicating that the refractive index of the air-hydrate crystals is larger than that of the surrounding ice matrix. The average value of Δn with its standard deviation is

$$\Delta n = 5.3\times10^{-3} \ (\pm 0.9\times10^{-3}). \quad (2)$$

This value was in qualitative agreement with results obtained from Becke line tests.[2-4]

Thickness d (μm)	Refractive-Index Difference Δn
138	7.1×10^{-3}
145	5.7×10^{-3}
152	6.3×10^{-3}
155	5.7×10^{-3}
161	4.7×10^{-3}
168	4.9×10^{-3}
168	6.0×10^{-3}
172	4.0×10^{-3}
174	6.5×10^{-3}
185	4.8×10^{-3}
185	4.8×10^{-3}
194	4.7×10^{-3}
194	5.7×10^{-3}
197	5.8×10^{-3}
203	4.4×10^{-3}
299	4.4×10^{-3}

Elongated ellipsoid

3. Discussion

The absolute refractive index of air-hydrate crystals was estimated using the following procedure. The refractive index of the ice matrix depends on its c-axis orientation varying from 1.3077 to 1.3090 at λ = 0.6238 μm and 270.3 K.[10] In the present study, the c-axis orientations of the ice matrix were random in each sample, so the refractive index of the ice matrix was estimated to be 1.3084 ($\pm$0.0007). This variation is smaller than the standard deviation of our measurements. It is therefore concluded that the mean refractive index of an air-hydrate crystal, n_{ah}, is

$$n_{ah} = 1.3137 \ (\pm 0.0016). \quad (3)$$

This value is slightly smaller than that predicted by Davidson et al.[7], which was between 1.3176 and 1.3186 at the sodium-D wavelength.

We then estimated the cage occupancy ratio of air-hydrate crystals from the obtained refractive index in equation (3). The refractive index of air-hydrate crystals, n_{ah}, is related to their cage occupancy ratio, θ, using the Onsager cavity model[17] by the following equations,

$$\frac{(n_{ah}^2-1)(2n_{ah}^2+1)}{9n_{ah}^2} = \frac{4}{51}\pi N_w \left(17\frac{\alpha_w}{1-f_w\alpha_w} + 3\theta\frac{\alpha_g}{1-f_g\alpha_g}\right) \quad (4)$$

$$f = \frac{2n_{ah}^2-2}{(2n_{ah}^2+1)\gamma^3} \quad (5)$$

where N_w and α_w are the number density and the polarizability of water molecules, respectively, α_g is the polarizability of air molecules, f is the reaction field factor, and r is the radius of the spherical cavity

in which an air molecule is considered to lie. We evaluated each parameter as described in the following paragraphs.

The value of N_W was determined by $N_W = 136 / x^3$, where x is the lattice parameter of a cubic unit cell of the air-hydrate crystal. x was obtained from X-ray diffraction analysis[5)6)] and found to be 17.213 Å at 243.2 K. In order to estimate the value at 270.2 K, the thermal expansion of air-hydrate crystals should be considered. Because the thermal expansion of air-hydrate crystals in an ice matrix will be the same as that of the ice lattice, we used the expansion coefficient of ice[11)], and estimated x as about 17.24 Å at 270.2 K.

A factor to be taken into account in applying equations (4) and (5) to the present data is the finite dependence of molecular polarizability, that is, the electronic states of the molecule, on the environment. To minimize this effect, we adopted the value of $\alpha_w / (1-f_w \alpha_w)$ to be that of ordinary ice at 270.2 K and $\lambda = 0.6328$ μm because the hydrate lattice has a hydrogen-bonded water structure similar to that of ice lattice.

On the other hand, as air molecules are a mixture of N_2 and O_2 molecules, we considered two cases to evaluate α_g: enclathrated air (i) has the same composition as atmospheric air (79% N_2, 21% O_2) and (ii) is enriched in oxygen and consists of 63% N_2 and 37% O_2, a value which was obtained from Raman spectroscopic analysis.[12)] Then ag is obtained from the polarizability of gaseous N_2 and O_2[7)], and (i) $\alpha_g = 1.73$ Å^3 or (ii) $\alpha_g = 1.70$ Å^3.

Normally the radius of a spherical cavity, r, is estimated by setting the volume of the sphere equal to the average molecular volume. Here r for use in evaluating f_g in equation (5) may be conveniently taken as the average free radius of small and larges cages containing air molecules. Thus r = 2.40 Å for small cages and r = 3.45 Å for large cages. Such a replacement of a poorly defined conceptual cavity in Onsager's treatment of liquids by a physically well-defined cage has already been used[7)] to account for some of the dielectric properties of clathrate hydrates.

Substituting these values into equations (4) and (5) gave values of the dependence of cage occupancy ratio θ on n_{ah} as shown in Fig. 2. This Figure indicates that θ increases almost linearly with both increasing n_{ah} and increasing O_2 concentration in the enclathrated air. The calculated value for $n_{ah} = 1.3137$ (a thick solid line) with errors (thin broken lines) are also shown in Fig. 2. The cross points between the measured n_{ah} line and the calculated N_2:O_2 mixture lines indicate that (i) $\theta = 0.921$ (± 0.032) and (ii) $\theta = 0.935$ (± 0.033) in the air-hydrate crystals measured in the present study.

These values are similar to the value of 0.91, estimated by comparison between the air-hydrate volume and total air volume in a 2542m depth Vostok ice core.[4)] The dependence of N_2:O_2 ratio on θ suggests that the composition of air molecules included in observed air-hydrate crystals is similar to that of the present atmospheric air. These values, however, disagree with the result obtained by Raman spec-

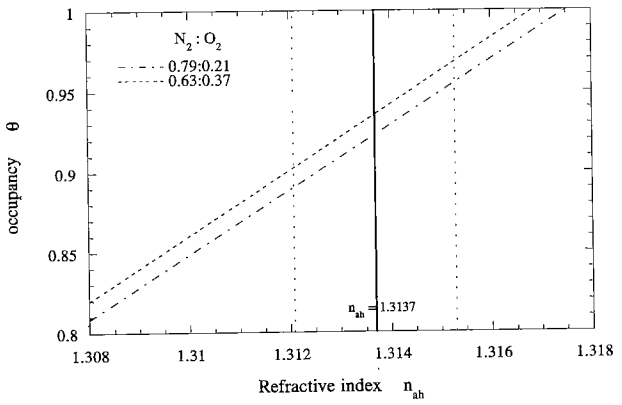

Fig. 2: The dependence of the cage occupancy, θ on the refractive index of air-hydrate crystals n_{ah}, calculated by the Onsager cavity model (eqs. (4) and (5)). Two air compositions are considered; (i) normal air (N_2:O_2 = 0.79:0.21; thin broken line) and (ii) oxygen-enriched air (N_2:O_2 = 0.63:0.37; thin broken line). The measured refractive index (thick solid line), n_{ah}=1.3137, is shown together with the experimental errors as thin dotted lines, ± 0.0016.

troscopic analysis on air-hydrate crystals in Dye-3 ice cores.[12] The Dye-3 ice cores are much younger than our samples and the difference in results may indicate different climatic conditions at the time of air enclathration.

In view of the experimental difficulties and low accuracy of both X-ray diffraction analysis and measurements of the air-hydrate volume and total air volume, the present method of refractive index measurements is preferred for more accurate determination of the cage occupancy ratio of air-hydrate crystals. Therefore we suggest that the refractive index measurement provides a new tool for paleoclimatic study on polar ice cores.

Acknowledgments

We are very grateful to all Russian and French participants in drilling, field work and ice sampling, especially to Dr. V. Ya. Lipenkov for providing ice core samples and Dr. J. R. Petit for their transportation. We also would like to thank Dr. P. Duval, Dr. Y. Furukawa and Dr. A. Kohuchi for helpful discussion. One of the authors (T.U.) wish to thank Dr. R. W. Jackson for the proofreading of the manuscript. This work was supported financially by the Asahi Glass Foundation, the Japan Society for the Promotion of Science and the Science and Technology Agency.

References

1. J. Chappellaz, "Polar ice bubbles as recorders of past greenhouse gas concentrations," Analusis Magazine, 22, M25-27 (1994).
2. H. Shoji and C. C. Langway, Jr., "Air hydrate inclusions in fresh ice core," Nature 298, 548-550 (1982).
3. H. Shoji and C. C. Langway, Jr., "Microscopic observations of the air hydrate-bubble. Transformation process in glacier ice," J. de Physique, 48, C1 551-556 (1987).
4. T. Uchida, T. Hondoh, S. Mae, V. Ya. Lipenkov and P. Duval, "Air-hydrate crystals in deep ice core Samples from Vostok Station, Antarctica," J. Glaciol. 40, 79-86(1994).
5. T. Hondoh, H. Anzai, A. Goto, S. Mae, A. Higashi and C. C. Langway, Jr., "The Crystallographic Structure of the Natural Air-Hydrate in Greenland Dye-3 Deep Ice Core," Journal of Inclusion Phenomena and Molecular in Chemistry 8, 17-24 (1990).
6. T. Ikeda, T. Hondoh, K. Satoh, T. Uchida and S. Mae, "Development of X-ray analysis of polar ice cores," Photon Factory Activity Rept. 1993, # 11(National Laboratory for High Energy Physics, I baragi, 1994) P.360.
7. D. W. Davidson, R. N. O'Brien, P. Saville and S. Visaisouk, "Optical refraction by clathrate hydrate," J. Opt. Soc. America, B 3, 864-866 (1986).
8. J. Jouzel and other 16 members, "Extending the Vostok ice-core record of palaeoclimate glacial period," Nature, 364, 407-412 (1993).
9. Y. Furukawa and W. Shimada,"Three dimensional pattern formation during growth of ice dendrites - its relation to universal law of dendritic growth," J. Crystal Growth 128, 234-239(1993).
10. International Critical Tables of Numerical Data, Physics, chemistry and technology, (U.S. National Res Council, New York, 1930) 7, 17.
11. International Critical Tables of Numerical Data, Physics, chemistry and technology, (U.S. National Res Council, New York, 1928) 3, 43.
12. J.Nakahara, Y.Shigesato, A.Higashi, T. Hondoh and C.C. Langway, Jr., "Raman spectra of natural clathrates in deep ice cores," Philos. Mag. B57, 421-430 (1988).

Determination of Silicon in Electrolyte Solutions by Electrothermal Atomic Absorption Spectrometry Using Platinum as a Chemical Modifier*1

(Key Words : Silicon; mateix modifier; platinum; electrolyte solutions; electrothermal atomic absorption)

Masami FUKUSHIMA*2, Tashio OGATA*3*4, Kensaku HARAGUCHI*3,
Kohichi NAKAGAWA*3 and Saburo ITO*3
Masao SUMI*2 and Naoto ASAMI*2

1. Introduction

The determination of silicon is important for evaluation of the quality of advanced technology products, e.g., semiconductors and ceramics.[1,2] Electrothermal atomic absorption spectrometry (ETAAS) is known to be a direct method for the determination of silicon, in addition to being simple and having excellent sensitivity and precision.[3-9]

Frech and Cedergen investigatde the determination of silicon by ETAAS.[3] Silicon is diffcult to determine by ETAAS because of the problems of atomization. The use of a platform furnace[4,5] and the addition of chemical modifiers[6-8] have been studied for the determination of silicon to improve the sensitivity and to reduce interferences from diverse elements. A chemical modifier is advantageous as it can simplify the analytical procedure, such as the separation and concentration of the analyte stages. It has been reported that silicon concentrations of the order of μgml^{-1} can be determined by the addition of an alkali metal fluoride,[6] a lanthanum-calcium mixture[7] or palladium[8] as the chemical modifier.

In the present work, the addition of platinum as a chemical modifier was found to be useful for enhancement of the peak height absorbance of silicon during ETAAS. The effect of platinum as a modifier was investigated, as was the effect of diverse elements on the peak height absorbance signal. The addition of platinum as a chemical modifier for ETAAS was investigated for the determination of silicon in electrolyte solutions (1 $moll^{-1}$ LiOD in deuterium oxide) of a fuel cell being studied for the generation of excess heat.

EXPERIMENTAL

Reagents

A silicon standard solution ($1000mgl^{-1}$), prepared by dissolving Na_2SiO_3 in 0.4 $moll^{-1}$ solution of Na_2CO_3, was purchased from Wako Pure Chemicals (Tokyo, Japan). A platinum standard solution for AAS ($1000mgl^{-1}$, Wako Pure Chemicals) was used as the chemical modifier. Deuterium oxide (D_2O, ISOTEC, Tokyo, Japan) was used as supplied.

Apparatus

A Varian atomic absorption spectrometer, Model Zeeman SpectrAA-40, equipped with a programmable autosampler, was used. A silicon hollow cathode lamp was utilized at a working current of 10 mA, using the 250.6 nm spectral line and a 0.2 nm bandwidth. Argon was used as the purge gas.

---

*1 This paper was reproduced from Journal of Analytical Atomic Spectroscopy, Vol.10, November (1995) pp999～1002 by the permission of The Royal Society of Chemistry

*2 The Institute of Applied Energy, New Hydrogen Energy Laboratory

*3 Bioscience and Chemistory Division

*4 To whom corresponce should be addressed.

The temperature programming of the furnace is given in Table 1. A 20 μl portion of the standard or sample solution was diluted and mixed with 5 $\mu\ell$ of the modifier solution using the auto-mixing mode of the autosampler. A Varian pyrolytic graphite coated graphite tube (Part No.63-100012-00) was used. An inductively coupled plasma mass spectrometry (ICP-MS) instrument, Model PMS-2000 (Yokogawa Analytical Systems. Tokyo, Japan), was used for the determination of diverse elements in the electrolyte samples. Water used throughout the experiments was obtained from Barnstead RO-Pure and NANO-Pure systems (Barnstead/ Thermolyne, Dubuque, IA, USA).

Table 1 Furnace operating conditions

Stage	Step No.	Temperature/℃	Time/s	Gas flow/l min^{-1}
Dry	1	85	5	3
	2	95	40	3
	3	120	10	3
Ash	4	700	5	3
	5	700	1	3
	6	700	2	0
Atomize	7	2700	1	0
	8*	2700	2.3	0
Clean	9	2700	2	3

*The absorbance was read during this step

Electrolyte Solutions

The electrolyte solutions (1 $moll^{-1}$ LiOD in D_2O) were obtained from the New Hydrogen Energy Laboratory, Energy Applied Institute (Sapporo, Japan), where the electrolysis of an LiOD-D_2O system with a palladium cathode has been studied in order to generate excess heat.

The electrolysis cell for the generation of the excess heat was a fuel cell type and the set-up has been repored in the literature.10.11 The electrolyte solutions were stored in PTFE bottles. These solutions were diluted 50-3000-fold with water just prior to the determination of silicon.

Polyethylene containers (Nargen, NY, USA) were used but no glassware, to avoid any contamination by silicon.

RESULTS AND DISCUSSION

Modifiers

It could be expected that other platinum group metals, i.e., platinum and nickel, would be effective as chemical modifiers since palladium is effective for the determination of silicon by ETAAS.[8] The peak absorbance profiles for 0.76 ng of silicon without and with any chemical modifier are shown in Fig.1. As is shown in Fig.1 (a), only a small absorbance signal for silicon was observed wihtout the modifier. When 25 ng of palladium, nickel or platinum were added as the modifier, the signal was enhanced [Fig.1 (b), (c) and (d)].

Howevre, the enhancement of the signal with the palladium or nickel modifier was smaller than that with platinum. The addition of 2.5 μg of palladium or nickel

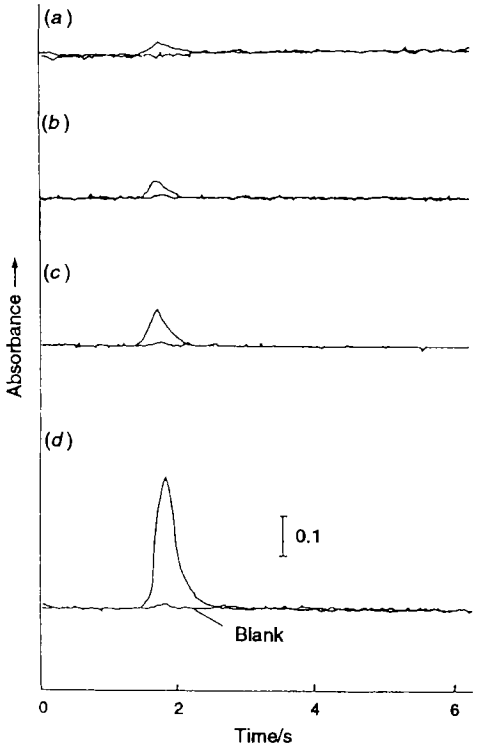

Fig.1 Absorption profiles of silicon with various chemical modifiers (25 ng) added: (a) without modifier, 0.023 absorbance; (b) with Pd, 0.048 absorbance; (c) with Ni, 0.080 absorbance; and (d) with Pt, 0.313 absor-bance. Pt, Pd and Ni were added as H_2PtCl_6 $Pd(NO_3)_2$ and $NiCl_2$ respectively, and background correction was not used. Ashing temperature, 900℃ and atomization temperature, 2700℃

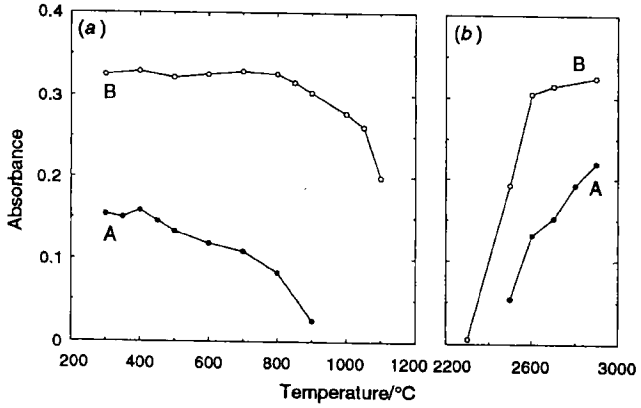

Fig.2 Effect of(a)ashing temperature(atomization temperature, 2700℃) and (b) atomization temperature [ashing temperature, 400℃ (without Pt), 700℃ (with Pt)] on peak height absorbance: A, in the absence of modifir (100 ng ml^{-1} Si);and B, in the presence of Pt(38ng ml^{-1} Si and 25 ng Pt)

was necessary in order to obtain the same signal enhancement as that of 25 ng of platinum, as is shown in Fig.1(d). The peak height absorbance for the addition of 250 ng of the platinum modifier was also the same as that for 25 ng of platinum. Therefore, platinum is the most effective of the three chemical modifiers investigated for the determination of silicon.

Effect of Ashing and Atomization Temperature

The relationship between ashing temperature and the peak height absorbance is shown in Fig.2(a). When platinum was not added as a modifier [Fig.2(a)line A] ,the peak height was almost constant up to 400℃ and then decreased with an increase in the ashing temperature above 400℃. This is probably due to the formation of silicon oxide, which is difficult to atomize. According to the phase diagram, silicon oxide exists in a non-crystalline form at lower ashing temperatures (<400 ℃), which seems to atomize comparatively easy, buy is present as a crystalline form at higher temperatures (>400 ℃), which is more difficult to atomize than the non-crystalline form. However, with the addition of 25 ng of platinum [Fig.2(a) line B), The peak height was constant up to 800℃ and decreased on increasing the ashing temperature above 800℃ . This shows that silicon is stabilized at higher temperatures by the addition of platinum. The effect of platinum on the atomization temperature was also investigated [Fig.2 (b)]. When platinum was not added as the modifier [Fig.2(b)line A] , the peak height absorbance increaed with temperature. This result supports the fomation of silicon oxide, which is difficult to atomize during the ashing stage. On the other hand, when platinum was added [Fig.2(b) line B] ,a plateau region was obtained between 2600 and 2900℃, which shows that shows that addition of platinum helps to improve the atomization efficiency of silicon.

When palladium is used as a modifier, intermetallic compounds are formed and the analyte is stabilized to a higher temperature.[12,13] Therefore, since silicon tends to form alloys wiht a range of metals, the modifier effect of platinum could also be attributable to the fomation

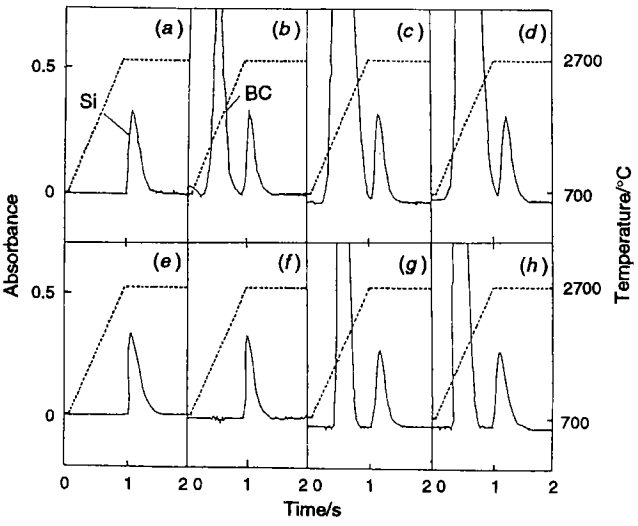

Fig.3 Effect of lithium, sodium and potassium on the background signal (38 ng ml^{-1} Si): (a) and (e) without alkali metals;(b) and (f) 0.1$moll^{-1}$ LiCl;(c) and (g) 0.1 $moll^{-1}$ NaCl;(d) and (h) 0.1 $moll^{-1}$ KCl. (a)—(d) Without Zeeman-effect background correction and(e)—(h)with Zeeman-effect background correction. Peak absorbance of silicon:(a) 0.332;(b) 0.321;(c) 0.343;(d) 0.377;(e) 0.328;(f) 0.317;(g) 0.320;and (h) 0.326. Blank, 0.1 $moll^{-1}$ alkali metals+ 25ng Pt. Signal of silicon(Si)and background(BC)shown and dotted line, temperature

Table 3 Determination of silicon in electrolyte solutions

	Calibration curve		Standard additions	
Sample*	Si/ng ml^{-1}	RSD†,%	Si/ng ml^{-1}	RSD†,%
D_2O	6.0	1.2	5.8	4.4
Cell A	5.9	2.0		
Cell B	47	1.7		
Cell C	52	0.5	53	2.4
Cell D	38	2.5		
Cell E	31	2.6		
Cell F	140	4.6		
Cell G	58	4.7	57	4.5
Cell H	95	2.6	98	3.7

*Cell A, 1 mol l^{-1} LiOD solution before electrolysis;Cell B, 1 mol l^{-1} LiOD solution after Ni calibration[10,11] Cells C-H, 1 mol l^{-1} LiOD after 45d of electrolysis.

†RSD, Relative standard deviation(n=3).

of intermetallic compound between silicon and platinum. An ashing temperature of 700℃ and an atomization temperature at 2700℃ were subsequently adopted for the determination of silicon in electrolyte solutions.

Effect of Alkali Metals

The absorbance profiles of silicon in the presence of 0.1 $moll^{-1}$ alkali metal chlorides are shown in Fig.3 A significant background signal was observed in the presence of alkali metals, probably owing to the molecular absorption of alkali metal salts.[14] The signals for the molecular absorption of alkali metal salts appear before that for silicon, as shown in Fig.3. It is generally known that Zeeman-effect background correction cannot be used effectively at an absorbance of higher than 2. Since the bacground absorbance in the case of lithuum [Fig.3(b)] was lower than 2, the background signal disappeared when using the Zeeman-effect background correction [Fig.3(f)] . However, the background signals due to sodium and potassium [Fig.3(c) and (d)] were greater than 3, and these background signals overlapped slightly with the silicon signal. Although the background signals from sodium and potassium could not be adequately eliminated with the use of Zeeman-effect background correction [Fig.3(f)] . However, the background signals due to sodium and potassium [Fig.3(c) and (d)] were greater than 3, and these background signals overlapped slightly with the silicon signal. Although the background signals from sodium and potassium could not beadequately eliminated with the use of Zeeman-effect background correction [Fig.3 (g) and (h)] , these signals were completey separated from those due to silicon when the correction system was used. The absorbance of silicon in the absence of alkali metals was not changed by Zeeman-effect background correction as shown in Fig.3(a) and (e). Moreover, the absorbance of silicon in the presence of alkali metals [Fig.3(f)－(h)] was the same as that in the absence of alkali metals [Fig.3 (e)] . Therefore, Zeeman-effect background correction was applied for the detrmination of silicon in the electrolyte solutions.

Since the electrolyte solutions contain large amounts of lithium ions, the effect of lithium concentration on the peak height absorbance of silicon was investigated.

Table 2 Effect of diverse elements in electrolyte solutions on the determination of silicon

Diverse element	Concentration range in electrolyte solutions/$\mu g\ ml^{-1}$	Added as	Concentration of diverse element added/$\mu g\ ml^{-1}$	Relative error, %
None*	—	—	—	100
B	0.03-4.3	H_2BO_3	1	101
			10	65
Al	0.3-1.2	$AlCl_3$	1	101
			5	85
Na	0.13-3.5	NaCl	1	102
			10	101
Cr	0.004-0.010	$K_2Cr_2O_7$	0.025	98
Zr	0.001-0.010	$ZrOCl_2 \cdot 8H_2O$	0.025	99
Mo	0.001-0.010	$(NH_6)Mo_7O_{24}$	0.025	102

*Without any diverse elements present;Si concentration 25 ng ml^{-1}

The results showed that the peak height was constant for lithium concentrations of between 0.025 and 0.2 $moll^{-1}$ and was the same as the peak height in the absence of lithium. Howevre, lithium was added to the standard and sampls solutions to maintain the lithium concentration at 0.1 $moll^{-1}$ as a matrix matching reagent.

Effect of Diverse Elements

Several electrolyte solutions were analysed by ICP-MS in order to identify the elements that could affect the determination of silicon. Only the elements listed in Table 2 were found in the sample solutions as diverse elements. The concentrations of boron, aluminium and sodium were in the range 30 ng ml^{-1} — 4.3 μ g ml^{-1}, and chromium, molybdenum and zirconium were in the range 1-10 ng ml^{-1}. The effect of each of these elements on the determination of silicon was studied.

As shown in Table 2, the absorption signal of silicon decreased to 60-65% of the original by the addition of 10 μg ml^{-1} of boron, whereas 1 μg ml^{-1} of boron had no effect on the absorption signal of silicon. Similarly, the signal decreased to 85-90% in the presence of 5 μ g ml^{-1} of aluminium. However, boron and aluminium were present in the electroyte solutions at concentrations of only up to 4 and 1.3 μg ml^{-1}, respectively. As the electrolyte solutions were diluted 50-3000-fold for the determination of silicon, the concentration levels of these elements would cause no problems in the detemination of 10-100 ng ml^{-1} level of silicon.

Analysis of Electrolyte Solutions

For a 20 μ l aliquot of sample, the calibration curve of silicon was linear within the range 0-40 ng ml^{-1} in the presence of platinum as a modifier. The relative standard deviation (n=5) was typically 1.5% at the 25 ng ml^{-1} of silicon level, and the relative correlation coefficient was 0.999_8. The detection limit for silicon, calculated as the 3 σ value of the blank absorbance, was about 0.4 ng ml^{-1}, i.e., 8pg.

The silicon concentration was then determined in eight electrolyte solutions and in the solvent, D_2O, by the calibration curve method. The standard additions method was also applied to some of these solutions. The results are summarized in Table 3, and as can bo seen, the concentrations of silicon in the samples obtained by the standard additions method are in good agreement with those obtained by the calibration curve method.

Therefore, the method proposed in the present study is suitabie for the determination of silicon in electrolyte solutions. The concentrations of silicon in the electrolyte solutions after electrolysis (Cells B-H) were at the 30-180 μg ml^{-1} level. However, silicon in the D_2O and in the electrolyte solution before electrolysis (Cell A) was at 6 μg ml^{-1}. These results indicate that large amounts of silicon are dissolved in the solution from the cell wall during electrolysis.

The addition of platinum was effective for enhancing the absorption signal of silicon, and it was possible to determine μg ml^{-1} levels of silicon. As lithium, sodium and potassium did not affect the absorption signal of silicon, the proposed method could possibly also be applied to the determination of trace amounts of silicon, the proposed method could possibly also be applied to the determination of trace amounts of silicon in natural waters and biological fluid by ETAAS.

We thank Mr K.Nakajima of Varian Instruments, Japan Branch Office for many useful comments.

REFERENCES

1 Streckfuss, N., Frey., L., Zielonka, G. F., Ryzlewicz, C., and Ryssel, H., Fresenius' J.Anal.Chem.,1992,343, 765.
2 Fuchs-Pohl, G.R., Solinska, K., and Feig, H., Fresenius' J. Anal. Chem., 1992,343,711.
3 Frech, W., and Cedergren, A., Anal. Chim. Acta, 1980,113,227.
4 Shuttler, I. L., and Delves, H. T., J. Anal. At. Spectrom., 1988,3,145.
5 Gitelman, H.J ., and Alderman, F. R., J.Anal.At. Spectrom.,1990,5,687.

6 Nater, E. A., and Butrau, R.G.,Anal. Chim. Acta.,1989,220,83.
7 Zhuoer,H.,J.Anal. At.Spectrom.,1994, 9,11.
8 Analytical Methods for Zeeman Graphite Tube Atomizer, ed. Rothery, E., Varian Techtron, Mulgrave, Victoria, Australia, 1986, pp.13-15
9 Atomic Absorption Spectrometry, ed. Welz, B., VCH, 1985, pp.323-324.
10 Hasegawa, N., Hayakawa, N., Tsuchida, Y.,Yamamoto, Y.,and Kunimatsu, K., J. Am. Nucl. Soc., Proceedings: Fourth International. Conferenec on Cold Fusion, Dec. 1994, Hawaii, Plenary Session Papers, 1994,1,3.
11 Akita, H.,Tsuchida, Y.,Nakata, T.,Kubota, A., Kobayashi, M., Yamanoto, Y., Hasegawa, N., Hayakawa, N., and Kunimatsu, K., J. Am. Nucl. Soc.,Proceedings: Fourth International Conference on Cold Fusion, Dec. 1994, Hawaii,Plenary Session Papers, 1994,1,21.
12 Teague-Nishimura, J. E., Tominaga, T.,and Katsumoto, K., Anal. Chem., 1987,59,1647.
13 Styris, D. L., Prell, L. T., and Redfield, D. A., Anal. Chem., 1991.63, 503.
14 Culver, B. R., and Surles, T.,Anal. Chem., 1975,47,920.

北海道工業技術研究所報告

第69号

平成９年３月

発行　　工業技術院北海道工業技術研究所

〒062　札幌市豊平区月寒東２条17丁目２番１号

☎ 011(857)8400（ダイヤルイン）

ＦＡＸ 011(857)8900